Collective dynamics of passive and conformationally active membrane proteins

Quentin Goutaland

Université Paris Cité

Thèse de doctorat
d'Université Paris Cité

M S C

École Doctorale "Physique en Île-de-France" - ED 564

Laboratoire Matière et Systèmes Complexes

Collective dynamics of passive and conformationally active membrane proteins

---

Par **Quentin Goutaland**

Thèse de doctorat de Physique théorique

dirigée par Jean-Baptiste Fournier

Présentée et soutenue publiquement à Paris le 8 Décembre 2022
Devant un jury composé de

Nicolas Destainville, Professeur, Univ. Toulouse III	Rapporteur
Martin Müller, Maître de conférences, Univ. de Lorraine Metz	Rapporteur
Patricia Bassereau, Directrice de recherche, Institut Curie	Examinatrice
Jean-Baptiste Fournier, Professeur, Univ. Paris Cité	Directeur
Frédéric Van Wijland, Professeur, Univ. Paris Cité	Invité

Remerciements

En premier lieu, je tiens à remercier mon directeur de thèse Jean-Baptiste Fournier ainsi que mon officieux co-directeur Frédéric Van Wijland pour leur bienveillance, leur pédagogie et leur patience pour me transmettre leurs connaissances ainsi que pour m'avoir offert l'opportunité de rejoindre une équipe avec une ambiance de travail très agréable.

Je remercie également les membres du jury pour avoir consacré de leur temps à relire attentivement ce manuscrit.

Merci à Valentin Leroy et Philippe Marcq d'avoir endossé les rôles de parrain et tuteur dans mon comité de suivi de thèse. De façon générale je remercie les membres du laboratoire MSC pour toutes les discussions de physique ou non et les bons moments que j'ai passé durant ma thése, en particulier Marc Durand, Matthieu Roché et Bérangère Abou. Merci aux doctorants de la 777A, dont Johann Maddi et Alice Briole qui ont commencé leur thèse en même temps que moi. Merci également aux doctorants de la 768A pour les bons moments : Ruben, Thibaut, David, Jérémy, ainsi que les italiens Giulia, Gianmarco Fédérico et Alberto (cheesecake day !)

Enfin je tiens à remercier mes amis et ma famille qui m'ont soutenu tout au long de ma thèse. Merci à mes parents et mes grands-parents maternels qui sont toujours présents pour moi. Merci á mon frère pour nos rigolades. Et enfin je remercie Éléonore qui partage ma vie et m'a encourager quotidiennement au cours de ma thèse.

Résumé en français

Le rôle des membranes biologiques est de séparer la cellule et ses constituants de l'environnement extérieur et de réguler les échanges de celle-ci avec l'extérieur. Une membrane biologique est constituée de deux couches de fluide de lipides, composants amphiphatiques, qui, en s'auto-assemblant, rendent la membrane sélectivement perméable. Pour séparer la cellule de l'extérieur, la membrane se referme sur elle-même, adoptant la topologie d'une sphére que l'on appelle une vésicule. En plus de sa fluidité, la membrane oppose une résistance à la flexion et à l'extension, elle est donc élastique.

Une membrane biologique contient, de plus, des protéines qui remplissent différents rôles tels que le transport intra-cellulaire et extra-cellulaire et la signalisation cellulaire. Les protéines membranaires sont classées en deux catégories : les protéines dites intégrales qui restent en permanence en interaction avec la membrane via l'un de ses sites et les protéines périphériques qui ne restent attachées à la membrane que temporairement.

Dans la première catégorie, soit la protéine traverse la membrane et est ainsi en contact avec les deux couches (protéine transmembranaire), soit elle n'est en contact qu'avec une seule des couches (protéine monotopique). Dans le cas des protéines périphériques, les protéines ne sont en interaction qu' avec une seule monocouche.

Les protéines existent dans une grandes variété de formes et sont rigides, ainsi, s'appuyant sur la propriété élastique de la membrane, elles peuvent induire une courbure à la membrane. C'est typiquement le cas des protéines faisant partie de la superfamille des BARs ; ces protéines périphériques ont une forme de banane qui leur permet de courber la membrane localement le long de leur domaine lorsqu'elles s'accrochent à cette dernière.

A ce mécanisme de courbure à l'accrochage, s'ajoute la possibilité, pour certaines protéines, en particulier les transmembranaires, de changer de conformation. En effet, des réactions chimiques ont lieu entre les protéines et les divers composés chimiques présents dans la membrane et autour. Ainsi, les protéines BmrA faisant parties des transporteurs ABC, réagissent à l'hydrolyse de la molécule d'ATP pour changer leur forme et, par là même, permettre le transport de composants de l'extérieur vers l'intérieur de la cellule. On a donc l'existence d'un mécanisme de changement conformationnel actif de la protéine qui induit lui aussi des déformations à la membranes.

Les déformations membranaires induites par les protéines au travers des mécanismes présentées au-dessus sont à leur tour source d'interactions. D'abord, la membrane étant décrite par un champ élastique, ces déformations génèrent des interactions élastiques entre les protéines. Ensuite, les protéines imposent localement des contraintes au champ

membranaire et celui-ci est soumis à des fluctuations thermiques. De ce fait, des interactions de type Casimir apparaissent entre les protéines. On parle donc ici d'interactions médiées car les protéines n'intéragissent pas directement entre elles, mais seulement au travers des déformations du champ qui affectent leur déplacement. Par conséquent, à la fois les fluides de lipides qui composent la membrane et les protéines sont déplacées, ce qui pose la question de la mobilité des objets dans la membrane.

A ces interactions médiées, s'ajoutent des couplages hydrodynamiques ; la membrane étant constituée d'une bicouche de lipides de quelques nanomètres pouvant être assimilée à un fluide bidimensionnel, il se crée des couplages hydrodynamiques 2D entre les protéines, eux-mêmes couplés aux écoulements 3D des fluides entourant la membrane, à la fois de l'extérieur et de l'intérieur.

Cette thèse s'attache à étudier la dynamique collective des protéines dans une membrane biologique, en considérant les mécanismes décrits ci-dessus. On utilise des approches analytiques, mais aussi numériques.

On commence par modéliser la statique du système. On considère un morceau de membrane en contact avec un réservoir de lipides. Se basant sur ses propriétés élastiques, Helfrich a établi un Hamiltonien qui permet de modéliser les déformations de la membrane comportant une énergie de flexion qui fait intervenir les invariants du tenseur de courbure : la courbure moyenne et la courbure de Gauss. De plus, l'ensemble thermodynamique approprié pour décrire ce système est l'ensemble grand canonique qui fait apparaître une tension de surface effective qui pénalise les déformations.

En sus, on considère que les protéines sont ponctuelles. Cette supposition permet de simplifier la modélisation du couplage entre les protéines et la membrane car la présence d'une taille pour les protéines induirait des conditions aux bords convoluées à l'énergie de couplage. Toujours dans un esprit de simplification, on considère un couplage quadratique, un couplage linéaire n'étant pas suffisant pour rendre compte des intéractions multicorps essentielles pour étudier les interactions médiées entre protéines.

On s'attelle ensuite à décrire la dynamique du système. Pour cela, on assimile la membrane à un fluide infini incompressible bidimensionnel entouré, de part et d'autre, par des solvents aqueux qui transmettent des contraintes visqueuses à la membrane. Et on considère la présence de protéines ponctuelles induisant une courbure locale isotrope à la membrane.

Les dynamiques de la membrane et des protéines sont ainsi décrites par des équations de Langevin suramorties avec des bruits qui satisfont le bilan détaillé à l'équilibre thermique et, auxquels il est possible d'ajouter des taux permettant de mettre le système hors d'équilibre.

Cette modélisation nous a permis, dans un premier temps, d'étudier le comportement collectif de protéines périphériques pouvant s'accrocher et se détacher de la membrane selon un mécanisme thermalisé ou activé.

Nous avons déterminé et analysé le diagramme de phase d'une membrane en contact avec un réservoir de telles protéines qui induisent une courbure locale et isotrope à la membrane lorsqu'elles s'accrochent, à l'aide d'approches à la fois analytiques et numériques.

A l'équilibre thermique, avec des taux d'accrochage et de décrochage respectant le

bilan détaillé, une analyse de stabilité linéaire appliquée à l'énergie libre d'une membrane plane contenant une densité uniforme de protéines en fonction du potentiel chimique du réservoir et de la courbure spontanée des protéines montre que la membrane présente trois phases différentes :

- une phase dite phase non liée uniforme et plane (U). Dans cette phase, peu de protéines se sont accrochées à la membrane, cette dernière contient donc une densité faible de protéines et reste plane en moyenne.

- Une phase liée uniforme et plane (B), où une densité très élevée de protéines s'est attachée à la membrane, générant donc une courbure uniforme à la membrane, mais qui, en raison des conditions aux limites périodiques, reste plane.

- Une phase «vallonnée»(SC) dans laquelle la membrane se compose de régions de courbure et de densité de protéines différentes.

La structure adoptée dans la dernière phase étant non linéaire, une analyse de stabilité linéaire n'est pas suffisante pour la déterminer. On utilise donc un *ansatz* sur la forme adoptée par la membrane qui nous permet de déterminer que dans la phase vallonnée, la membrane s'ondule, on observe une succession périodique de zones courbées où se concentrent les protéines et de zones vidées de protéines, où la membrane s'infléchit dans le sens contraire. De plus, en étudiant le coût énergétique optimal de ces ondulations de la forme de la membrane par rapport à une membrane plane en fonction du potentiel chimique et de la courbure spontanée, on a pu obtenir un point tricritique, à droite duquel survient une transition de phase du second ordre entre la phase non liée U et la phase vallonée SC. A sa gauche, on observe une transition de phase du premier ordre entre les phases SC et B.

De plus, on trouve une transition du premier ordre entre les phases U et B en restaurant les fluctuations d'équilibre en présence de protéines ayant une courbure spontanée nulle, c'est-à-dire, en considérant des protéines soumises uniquement à des interactions de type Casimir.

On considère ensuite le cas hors d'équilibre en rajoutant un mécanisme d'accrochage-décrochage actif décrit par un processus de Poisson, et brisant le bilan détaillé. En appliquant une analyse de stabilité linéaire sur la dynamique du système, on montre que la présence d'activité altère la stabilité de la phase vallonnée : en présence de décrochage actif, on observe un décalage de la région où la membrane adopte la phase vallonnée vers des valeurs du potentiel chimique du réservoir plus élevées car l'ajout d'un taux de décrochage entraîne la stabilisation de la membrane plane.

En parallèle, nous avons mené une approche numérique dont les simulations ont été effectuées par Hiroshi Noguchi. Dans ces simulations, on considère que la membrane est constituée de particules qui s'auto-assemblent à l'aide d'un potentiel attractif. Un réservoir de protéines qui s'accrochent et se décrochent stochastiquement de la membrane avec des taux satisfaisant la condition de bilan détaillé entoure la membrane lorsque l'on étudie l'équilibre thermique, on peut étendre ce modèle en introduisant des taux actifs plongeant le système hors d'équilibre.

Qualitativement, le diagramme de phase à l'équilibre thermique obtenu numériquement est en accord avec celui trouvé analytiquement : on observe les trois phases décrites plus haut et on obtient les mêmes transitions de phases. Concernant la phase SC, la simulation montre une structure où les zones courbées et denses en protéines ont une forme hexagonale. De même, l'analyse numérique hors d'équilibre donne un comportement similaire à celui déterminé analytiquement en présence de décrochage actif.

Dans un second temps, nous nous intéressons à la diffusion de protéines ponctuelles qui induisent une courbure locale à la membrane.

On commence par étudier la diffusion d'une protéine isolée assimilée à un objet ponctuel. Cette approche nous permet non seulement de retrouver la loi de Saffman-Delbrück, mais aussi de la généraliser. Cette loi établie en 1976 par Saffman et Delbrück permet de déterminer la mobilité d'une protéine dans une membrane. La membrane étant un fluide 2D infini, à nombre de Reynolds faible, la mobilité diverge (paradoxe de Stokes). Toutefois, considérer les solvents entourant la membrane permet d'introduire une longueur caractéristique, appelée longueur de Saffman-Delbrück, qui permet de régulariser la mobilité. Cependant, la dérivation usuelle de cette loi nécessite des calculs lourds. Grâce à notre approche «ponctuelle» faisant intervenir une coupure ultraviolette de l'ordre de l'inverse de la taille caractéristique de la protéine, nous arrivons à dériver cette loi simplement, à un facteur près. Fort de ce résultat, nous avons étendu cette approche en prenant en compte d'autres effets.

Tout d'abord, on prend en compte le caractère bicouche de la membrane. En effet, la membrane se compose de deux couches de lipides ayant chacune leur propre viscosité. De plus, à l'interface entre les deux couches, la (faible) interdigitation entre les queues des lipides génère une friction intermonocouche.

Dans un premier cas, on considère une protéine ne se déplaçant qu'au sein d'une seule couche. En imposant une condition de non-glissement entre la protéine et la monocouche, on trouve que pour de larges valeurs du coefficient de friction intermonocouche la loi de Saffman-Delbrück décrit toujours la mobilité du système, à condition de remplacer la viscosité de la membrane assimilée à un fluide unique par la somme des viscosités des deux couches. Ainsi, dans ce régime, la friction entre les couches peut être négligée car cela revient à imposer une condition de non-glissement entre les couches. Pour des valeurs plus faibles qu'un seuil dépendant de la viscosité de la membrane et de la taille de la protéine la loi de Saffman-Delbrück trouvée ne tient plus, et on trouve une mobilité plus large car le fluide de la couche ne contenant pas la protéine n'est pas entièrement entraînée par le déplacement de cette dernière.

Dans le cas d'une protéine occupant l'intégralité de la bicouche, nous montrons que la contrainte de non-glissement entre la protéine est chaque monocouche entraîne une condition de non-glissement entre les deux couches. Ainsi, pour toutes valeurs physique du coefficient de friction intermonocouche, on retrouve une loi de Saffman-Delbrück dont la viscosité est la somme des viscosités des deux monocouches.

Dans un second cas, on considère une protéine induisant une courbure à la membrane. En utilisant un couplage linéaire entre la protéine et la membrane, notre approche nous permet de démontrer que dans le régime des faibles déformations, la friction totale ressentie par la protéine est la somme de la friction usuelle d'une protéine isolée se déplaçant

dans un fluide 2D plan (Saffman-Delbrück) et d'une friction supplémentaire due à la force de rappel qu'exerce la déformation sur la protéine.

Finalement, on étudie la diffusion collective d'un ensemble de protéines induisant une courbure à la membrane a l'aide de simulations numériques.

Il a été montré que les couplages hydrodynamiques entre protéines formant un ensemble dense dans un fluide incompressible 2D (membrane maintenue plane) génèrent un déplacement collectif. En effet, en présence de ces interactions hydrodynamiques, le coefficient de diffusion du centre de masse de l'ensemble devient comparable à celui du grandissement du rayon de gyration.

Pour effectuer nos simulations, on considère un ensemble d'un nombre fini de protéines ponctuelles distribuées initialement uniformément dans un cercle dans une membrane maintenue plane. La dynamique des protéines suivant une dynamique brownienne, on remplace le tenseur hydrodynamique usuel d'Oseen par un tenseur défini positif dérivé selon la méthode variationnelle de Rotne et Prager. Ceci est nécessaire car le calcul numérique fait intervenir la décomposition de Cholesky qui n'est possible que pour des tenseur de mobilité définis positifs. Nos simulations nous permettent de valider numériquement les prédictions analytiques trouvées dans la littérature sur le comportement collectif des protéines à temps long : la diffusion collective est subdiffusive et la distribution interprotéine, initialement uniforme, tend vers une distribution gaussienne au fil du temps.

Enfin, on prend en compte les couplages entre la membrane et des protéines qui induisent localement une courbure spontanée à la membrane, ainsi que les fluctuations de cette dernière. Pour cela, on considère un patch de taille finie de membrane et on impose des conditions aux limites périodiques. Dans l'espace de Fourier, on discrétise son champ de hauteur : on remplace le champ défini dans le continu par un réseau dont les sites contiennent chacun un mode du champ membranaire. La dynamique du système est décrite par une équation de Langevin suramortie faisant intervenir un noyau hydrodynamique pour la membrane, couplée à la dynamique brownienne des protéines à travers un couplage quadratique.

Comme dans le cas précédent, on considère un ensemble dense de protéines distribuées initialement selon une loi uniforme dans un cercle.

Les couplages hydrodynamiques étant toujours présents, l'étude numérique des coefficients de diffusion du centre de masse de l'ensemble et du grandissement du rayon de gyration établit l'existence de la diffusion collective des protéines.

Toutefois, on observe un coefficient de diffusion collective réduit en présence des fluctuations de la membrane. L'étude de cette distinction avec le cas d'une membrane plane nécessite une étude plus poussée, non effectuée dans cette thèse, mais nous suspectons que cet effet est dû à des forces de rappel exercées par la membrane sur les protéines.

Résumé

Les membranes biologiques sont des constituants importants de nos cellules qui ont pour rôle de séparer le cytoplasme du fluide extracellulaire. Les bicouches lipidiques, qui forment la base de ces membranes, sont des structures auto-assemblées qui confèrent ses propriétés de fluidité et d'élasticité aux membranes. De plus, les membranes biologiques contiennent des protéines, objets rigides existant dans une grande variété de formes et impliqués dans plusieurs mécanismes biologiques tels que les transports intra et extracellulaires. En raison de leur forme et de leur rigidité, certaines protéines peuvent déformer les membranes. D'autres sont même conformationellement active, i.e., elles peuvent changer leur forme, passant sur des états qui peuvent déformer ou non la membrane Ces déformations élastiques entraînent des interactions médiées élastiques entre les protéines, auxquelles s'ajoutent des interactions de type Casimir issues des fluctuations de la forme de la membrane. En outre, la membrane biologique est entourée par un solvent, ajoutant ainsi des couplages hydrodynamiques.

Cette thèse aborde la dynamique collective de protéines membranaires passives et conformationellement actives qui induisent une courbure locale à la membrane, au travers d'approches à la fois analytiques et numériques.

Dans le Chapitre 3, nous déterminons analytiquement et numériquement le diagramme de phase à l'équilibre thermique d'une membrane en présence de protéines induisant une courbure qui peuvent s'accrocher ou se décrocher de la membrane en fonction de leur courbure spontanée et du potentiel chimique du réservoir de protéines. Au moyen d'une analyse non-linéaire, nous étudions la structure adoptée par la phase instable. Nous étendons ensuite l'étude du système au cas hors-équilibre en ajoutant des taux actifs au processus d'accrochage et de décrochage des protéines.

Dans le Chapitre 4, nous appliquons une approche ponctuelle à l'étude de la diffusion d'une protéine membranaire isolée. Cette méthode nous permet de retrouver simplement la loi de Saffman-Delbrück (SD) qui régit la mobilité d'un objet se déplaçant dans un fluide bidimensionnel. Nous présentons ensuite des généralisations de cette loi en prenant en compte le caractère bicouche de la membrane. Enfin, nous obtenons analytiquement la correction de la loi de SD pour une protéine qui génère une courbure spontanée locale.

Dans le Chapitre 5, nous présentons une approche numérique qui nous permet de confirmer des prédictions sur le comportement à long terme de la diffusion collective de protéines dans une membrane non fluctuante et en présence de couplages hydrodynamiques. Nous étudions ensuite le comportement collectif de protéines induisant une

courbure locale dans une membrane fluctuante.

Mots-clés : Matière molle, Matière active, Interactions hydrodynamiques, Interactions médiées, Membranes biologiques

Abstract

Biological membranes are important constituents of our cells that separate the cytoplasm from the extracellular fluid. Lipid bilayers, which form the basis of these membranes, are self-assembled structures that give fluidity and elastic properties to the membranes. Furthermore, biological membranes contain proteins, rigid objects coming in various shapes and implied in many biological mechanisms such as intra and extracellular transport. Due to their shape and rigidity, some proteins can deform the membranes and others are conformationally active, *i.e.*, they can switch between states which can either deform the membrane, or not. These elastic deformations cause elastic mediated interactions between proteins, which are supplemented by Casimir-like interactions coming from the membrane shape fluctuations. In addition, a biological membrane is surrounded by a solvent fluid adding hydrodynamic couplings.

This thesis deals with the collective dynamics of passive and conformationally active proteins that induce a local curvature of the membrane, using both analytical and numerical approaches.

In Chapter 3 we determine analytically and numerically the phase diagram of a membrane in the presence of thermalized curvature-inducing proteins that can bind to or unbind from the membrane as a function of the spontaneous curvature and the chemical potential of the reservoir. By means of a nonlinear analysis, we study the pattern selected by the unstable phase. We then extend the study by considering, in addition, active rates for the binding/unbinding process of proteins.

In Chapter 4 we resort to a pointlike modeling of the protein diffusing within the membrane. This method allows us to make a simple derivation of the well-known Saffman-Delbrück (SD) law that governs the mobility of an object moving within a bi-dimensional fluid. We then present analytical generalizations of this law by taking into account the bilayer nature of the membrane. And we are able to derive the correction of the SD law for a protein that creates a local spontaneous curvature.

In Chapter 5, we present a numerical approach that allows us to confirm the predictions made in the literature on the long-time behavior of the collective diffusion of proteins in a non-fluctuating membrane and with hydrodynamic couplings. We then study the collective behavior of curvature-inducing proteins in a fluctuating membrane.

Keywords: Soft matter, Active Matter, Hydrodynamics interactions, Mediated interactions, Biological membranes

Contents

Chapter 1

Introduction: the soft matter physics of membranes and proteins

1.1 Biological membrane structure

In this first section, we introduce one of the main components of biological membranes, lipids, and how they self-assemble into bilayer membranes. And finally, we briefly describe biological membranes.

1.1.1 Lipids

Lipids are commonly defined as organic compounds that are insoluble (or sparingly soluble) in water but dissolve in organic solvents. Given this loose definition, a wide range of molecules is included under the term lipid, including sterols, waxes, or fatty acids [1]. In addition, most lipids fall into the latter group of fatty acids because they contain a hydrocarbon chain characteristic of fatty acids. This hydrocarbon chain is aliphatic, i.e., it is not aromatic, and is responsible for the hydrophobic aspect of lipids. Along this hydrophobic chain at one end, the lipids terminate with a carboxylic acid at their other end. Unlike the chain, this "head" is hydrophilic and therefore soluble in water. The two major components of cells, triglycerides and phospholipids, are examples of such molecules. Triglycerides, which are the main component of both animal and plant fats, serve as energy stores. Phospholipids are the main component of membranes.

Phosphoglycerides are shown in Fig. 1.1 along with the other group of phospholipids: sphingolipids. Sphingolipids, like phosphoglycerides, have two "tails" one of which is derived from sphingosine, an aliphatic chain that ends with an amino group. Sphingolipids are involved in signal transduction [2]. The typical size of phospholipids is determined by the length of their aliphatic tails, which is about 2 nm [3]. Having both a hydrophobic part through its aliphatic chains and a hydrophilic headgroup, phospholipids are amphiphilic, a property that plays a key role in the assembly of lipids into bilayer membranes as we will see in the following.

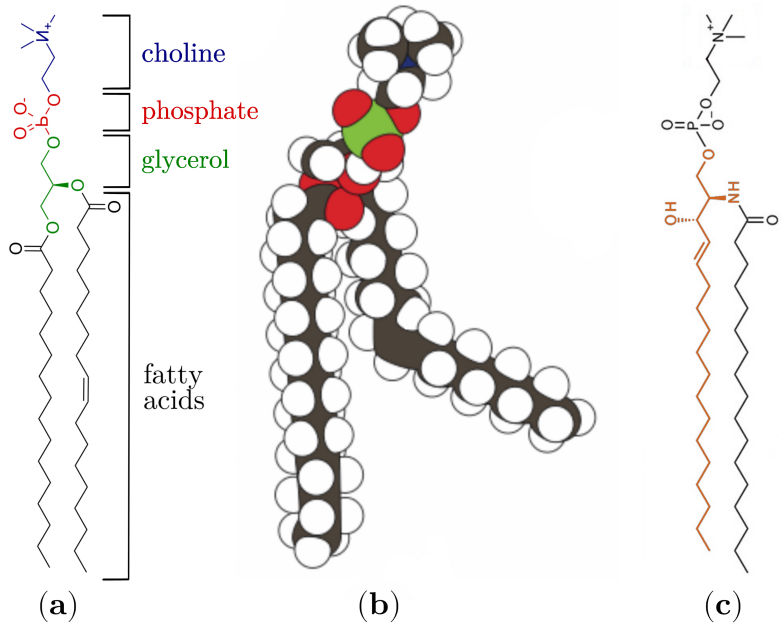

Figure 1.1 – Structural formulae of phospholipids. (a) Structural formula of a phosphoglyceride. Choline, phosphate, and glycerol form the "head" of the phospholipid and fatty acids its two "tails". This phosphoglyceride is called phosphatidylcholine. Its space-filling representation is given in (b). (c) Structural formula of a sphingomyelin. The orange part corresponds to the sphingosine tail of this sphingolipid. *Formulae (a, c) adapted from Wikimedia Commons and illustration (b) extracted from [4].*

1.1.2 Self-assembly of lipids

When phospholipids and water are mingled, two opposing effects compete: the hydrophilic head groups want to maximize their contact with water, while the hydrophobic tails tend to aggregate in order to minimize their contact area with water. Therefore, phospholipids seek to optimize their surface area with water to minimize their free energy and do so by assembling into supramolecular structures such as micelles, bilayers, or vesicles, as shown in Fig. 1.2. The way lipids self-assemble into such structures can be explained by a rather heuristic argument.

Using geometric considerations on the lipids [5], *i.e.*, considering the volume v of their hydrocarbon chains, the length ℓ of their tails, and the surface a of their hydrophilic head group, one can construct the so-called dimensionless packing parameter p given by $p = v/(\ell a)$. The value that this packing parameter takes indicates the possible structures in which the lipids self-assemble. However, the structure formed by the assembly of lipids not only depends on the geometry of the lipids, but also on entropy. For instance, single-chained lipids,*i.e.*, lipids with one tail, could form bilayer energetically, but cannot in reality due to entropy [5].

In the case of phospholipids, most self-assemble into bilayers where the interior of the leaflets are the tails ended on each side by the headgroups. This structure takes advantage of the amphiphilic property of its constituents to select objects that can pass through it. The thickness of the bilayer is around twice the phospholipids size, *i.e.*, 4-10 nm [6, 7]. Finally, to avoid contact between the hydrophobic chains and water, the bilayers

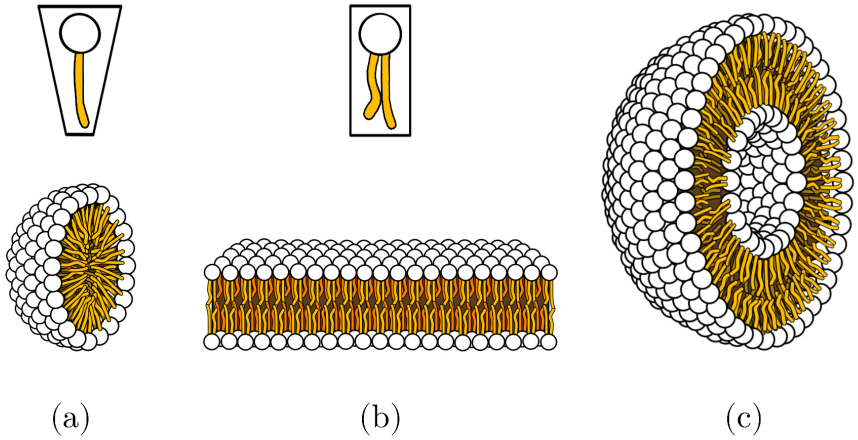

Figure 1.2 – Common supramolecular structures formed by lipids. (a) One-tailed lipids that have conical shapes tend to form micelles, whereas (b) rectangular-shaped lipids, such that phosphoglycerides, form bilayers. (c) A bilayer can be closed into a sphere called a vesicle. *Illustrations adapted from Wikimedia Commons.*

spontaneously close themselves by forming spherical vesicles called liposomes. It is this selectively-permeable structure that separates the cell from the external environment.

1.1.3 Biological membrane

The bilayer described so far is the basic structure of biological membranes. Biological membranes are essentially composed of three different components: lipids, sugars, and proteins [8].

In addition to phospholipids introduced previously, biological membranes contain other types of lipids such that glycolipids and sterols. Glycolipids share a structure similar to phospholipids, except that the phosphate group present in the latter is replaced by carbohydrates (sugar). These lipids have different functions, among which are cellular recognition and cell stabilization [9, 10]. As for sterols, they are composed of three cyclohexanes molecules ended on one side by a hydroxyl group replacing a hydrogen of the cyclohexane, and on the other side by a cyclopentane in a way presented Fig. 1.3a. The most common sterol in animal cells is the infamous cholesterol (Fig. 1.3b) which plays a key role in the regulation of membrane fluidity. Besides this lipids diversity, the two leaflets are often asymmetric, *i.e.*, their composition differs.

Proteins are diverse and have important functions within membranes such that transport across the bilayer. Since the membrane isolates the cell from the external environment, proteins act as watchmen which select what molecules can cross the membrane either inward to fuel the cell or outward to eliminate the toxins [8]. Section 1.3 gives more details about membrane proteins.

The model presented here is called the fluid mosaic model [11]. In this paradigm, the phospholipids composing the bilayer form a bidimensional fluid in which membrane proteins are embedded. Therefore, lipids are not static, they diffuse laterally as well as

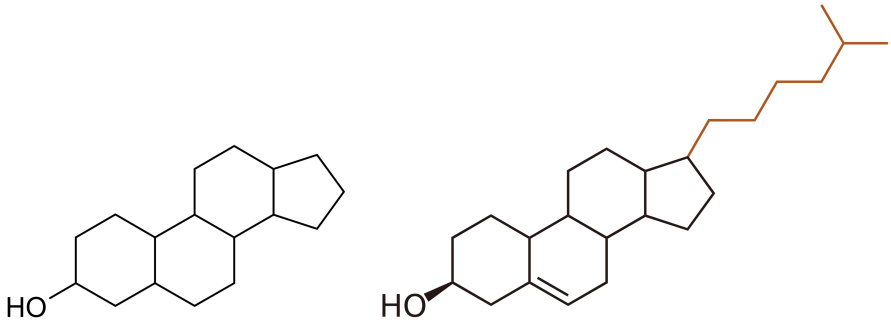

(a) (b)

Figure 1.3 – (a) Generic chemical formula of sterols. Sterols are composed of four carbon rings fused together and a hydroxyl group. (b) Structural formula of cholesterol. The sterol part is ended by a carbon chain. Like phospholipids, cholesterol is an amphiphilic lipid where the hydroxyl group corresponds to the hydrophilic head and the carbon chain plus rings are the hydrophobic tails. *Formulae adapted from Wikimedia Commons*

.

proteins. A well-known fluid mosaic representation of the biological membrane is given in Fig. 1.4

1.2 Membrane properties

Given the particularity of its formation–no covalent or electrostatic interactions bind the phospholipids to each other, they only keep the structure through the love-hate interactions with water–the bilayer presents some interesting physical properties described in this section.

1.2.1 Fluidity

As explained above, the phospholipids are not truly attached and form a fluid. The fluidity property of membranes is mainly affected by three factors, temperature, cholesterol concentration, and types of lipids [12].

First, the degrees of freedom of phospholipids influence membrane fluidity. When the temperature is increased, the lipids are more and more excited. Gaining thermal energy, they become more mobile and get away from each other, increasing fluidity. At low temperatures, lipids get closer and the structure is more organized. Therefore, lipids can undergo a phase transition between a solid-like phase, usually referred to as the gel phase, at low temperatures and a liquid phase at high temperatures. It is worth mentioning that the temperature of transition is indeed below the physiological one and that it depends on the cholesterol concentration as well as on the types of lipids. The cholesterol molecules help the membrane to stay fluid and keep its isolating property either by acting as a glue between phospholipids when they get too far from each other (high temperatures), and so avoiding unwanted molecules to cross the membrane, or by preventing phospholipids to be too close (low temperatures) and thus maintaining the membrane fluidity. Finally,

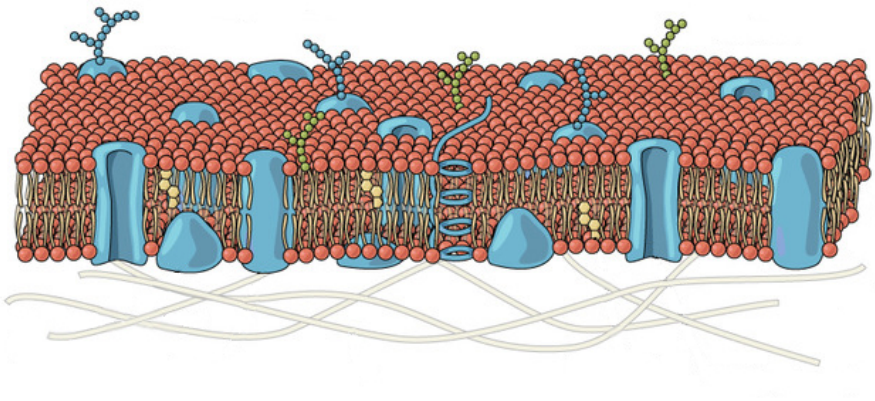

Figure 1.4 – Fluid mosaic model of the biological membrane. The bilayer is composed of phospholipids whose head is colored red here. Embedded in the bilayer we see the cholesterol lipids in yellow, the glycolipids in green, and finally the proteins in blue. The membrane is attached to the cell through the cytoskeleton filaments, the old lace tubes on the figure. *Illustration adapted from Wikimedia Commons.*

the fluidity is also affected by the fatty acids which are part of the phospholipids. The unsaturated ones, *i.e.*, the fatty acids where all carbon atoms have only single bonds between them, are straight and so easy to order closely and thus have a lower transition temperature than the saturated fatty acids which present "kinks" due to double bonds between some carbon atoms (see the right tail of the phosphatidylcholine in Fig 1.1b). These kinks create disorder and therefore favor the liquid phase.

Like every fluid, the bilayer is therefore characterized by a viscosity coefficient quantifying the internal friction between adjacent fluid molecules moving in different directions. The typical observed value is $\eta_2 = 4 \times 10^{-9}\,\mathrm{Js/m^2}$ [13].

1.2.2 Elasticity

In the fluid mosaic model [11], the phospholipid bilayer confers elasticity to the membrane, as it relaxes to its original shape after a constraint was applied to it. Therefore membranes respond to deformations either by bending or stretching, the two modes of elastic deformations.

The stretching happens when the area A of the membrane is changed from its mechanical equilibrium one A_0. In this case, analogous to the elongation of a spring, the variation of the free energy density Δf, *i.e.*, the free energy per unit area is given by

$$\Delta f = \frac{1}{2} k_s \left(\frac{A - A_0}{A_0} \right)^2 , \tag{1.1}$$

where k_s is the stretching modulus of the bilayer. The stretching modulus was measured experimentally in different bilayer membranes [14]. The order of magnitude obtained is $k_s \simeq 0.1\,\mathrm{N/m}$.

When the membrane shape is altered – different from its mechanical equilibrium shape – we speak about bending deformation. In the case of two identical monolayers, lipids

tend to align with each other and so the bilayer equilibrium shape is flat. However, when the compositions of the two monolayers differ, for instance, if the lipids in one monolayer are all cylindrical and the ones of the other leaflet are all conical, the bilayer spontaneously curves with a spontaneous curvature C_0. This asymmetry is not always as trivial as in the previous illustration; it arises from the variety of lipids found in membranes that make it difficult to get two identical monolayers. Furthermore, many proteins, as we will see later in Sec. 1.3, bend the membrane so as to satisfy their boundary conditions, resulting in a local curvature. In the case the curvature is imposed on the membrane, the free energy density is given by

$$\Delta f = \frac{1}{2}\kappa \left(C - C_0\right)^2 , \tag{1.2}$$

where κ is the bending modulus of the bilayer. Like the stretching modulus, the bending modulus was measured in membranes [14]. Its order of magnitude is $\kappa \simeq 10^{-19}\,\mathrm{J}$. More precisely, the values taken by κ goes from $10\,k_\mathrm{B}T$ to $30\,k_\mathrm{B}T$ (for T at room temperature).

1.2.3 Surface tension

As bilayers are fluid and surrounded by water, one could expect the emergence of a surface tension γ at the interface. Such phenomenon is usual for common fluid interfaces, *e.g.*, liquid-vapor interface, where the surface tension is defined by

$$\gamma = \left.\frac{\partial \mathcal{F}}{\partial A}\right|_{V,N,T} , \tag{1.3}$$

with $\mathcal{F}$ the free energy of the liquid, V its volume, A the area of the liquid-vapor interface, N the number of molecules in the liquid and T the temperature. Molecules at the interface have fewer bounds, *i.e.*, they have fewer neighbors and so less attractive interactions. Therefore, the bigger the interface area is, the greater the energy cost is. Thus the two fluids tend to minimize their interface area by changing their geometry and the force that keeps the system in this minimum energy configuration is the surface tension γ.

However, in the case of bilayers, the lipids have self-assembled in such a way that the area interface with water is minimized. Hence, if we consider a bilayer formed with a constant number of lipids, then it implies that the total area of the membrane is equal to its equilibrium one in the absence of any external constraints and thus the surface tension γ vanished [15].

Finally, membranes are subjected to thermal fluctuations. These fluctuations tend to deform the bilayer so that its shape is no more than its mechanical equilibrium one. Therefore the bilayer acts against these deformations which cost energy by inducing opposite forces, from which arises a surface tension that tends to restore the bilayer to its equilibrium shape. Here we work at a fixed area, therefore the "surface tension" σ is a Lagrange multiplier conjugate to the area A. This will be discussed further in Sec 2.1.1. The typical range of tension for membranes is $10^{-8} - 10^{-3}\,\mathrm{N/m}$. At higher tensions, membrane ruptures occur [16].

1.3 Proteins in membrane

In this section, we review the different types of proteins and then we present some curvature-inducing proteins.

1.3.1 Integral and peripheral proteins

Fig. 1.5 shows the main types of membrane proteins. There exist two types of membrane proteins: integral and peripheral.

Integral membrane proteins are proteins permanently embedded within the membrane thanks to one of its domains which ensures that they stay stuck in the bilayer. Transmembrane proteins are the most common integral proteins. Integral proteins are subdivided into three groups [17]. First, if the protein spans the bilayer by a single pass it is therefore bitopic. Such proteins have a hydrophilic region on both sides of the bilayer. In the case that the protein span the bilayer several times, *i.e.*, it passes back and forth across the membrane, the protein belongs to the polytopic group. Polytopic proteins have many hydrophilic regions on each side of the bilayer. Finally, the third group is called monotopic and corresponds to proteins that bind to the membrane on a single leaflet. These proteins bind to the membrane through their hydrophobic region, leaving the single hydrophilic domain outside the membrane.

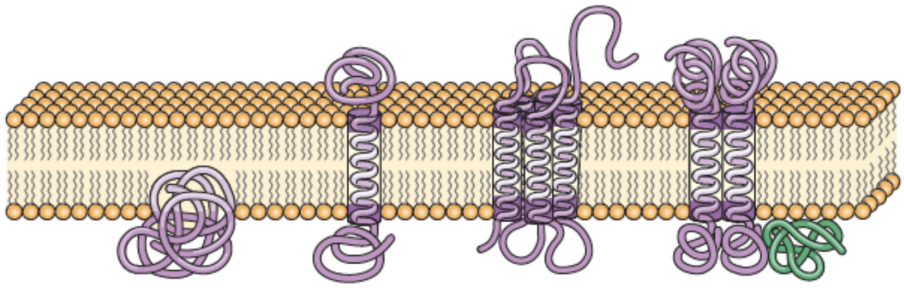

Figure 1.5 – Different types of membrane proteins. Purple proteins correspond to integral membrane proteins. The left one which is attached to the bottom leaflet is a monotypic protein. At its right comes the bitopic protein or singlepass protein that spans the bilayer once. Note that the protein represented is called an α helix due to its structure. Then there are the polytopic protein or multipass protein. Finally, some proteins can form a complex called multisubunit protein. A peripheral protein is shown in green. *Illustration adapted from Alchetron.com (https://alchetron.com/Membrane-protein).*

Unlike integral proteins, peripheral proteins are only temporarily attached to the membrane. Since they have no hydrophobic region, peripheral membrane proteins bind only to the surface of the bilayer, *i.e.*, to the heads of the phospholipids or to integral proteins, avoiding contact with the inner hydrophobic part of the membrane. Therefore, they are not in contact with the hydrophobic part of the bilayer. The bond these proteins

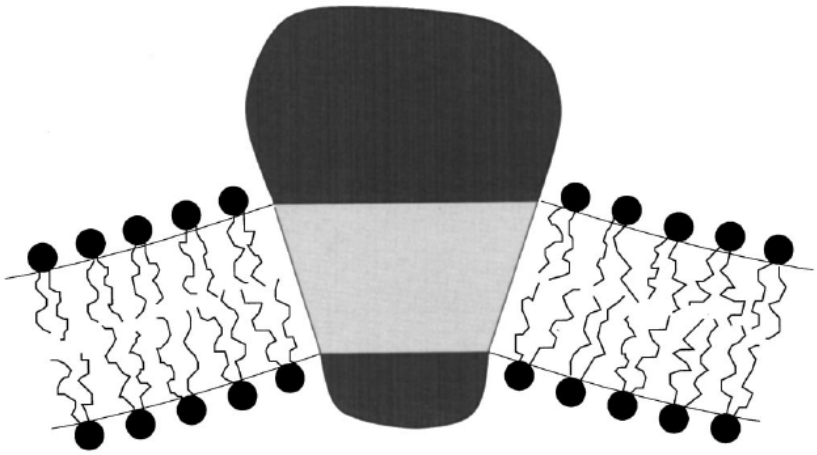

Figure 1.6 – Transmembrane conical shape protein embedded in a membrane. The conical shape of the protein (at the center) provokes the bending of the bilayer (on both sides). *Extracted from [19].*

form with the phospholipids can easily be broken and therefore peripheral proteins can move away from the membrane. While transmembrane proteins are mainly gateways that allow transport across the membrane, peripheral proteins are involved in signal transduction [18].

1.3.2 Curvature-inducing proteins

Since proteins are rigid and come in a wide variety of shapes on the one hand, and the membrane is elastic on the other, it is well understood that they can deform the bilayer to satisfy their boundary conditions by, for instance, inducing a curvature. A noteworthy case of such proteins is the conical transmembrane protein (see Fig. 1.6) of which KvAP and BmrA presented below are examples. This kind of protein being skewed at the interface with the bilayer, the lipids that would rather stay aligned can't anymore as it is not favored energetically, and so the bilayer locally bend near the protein. Below we give different examples of proteins inducing a curvature.

a. BAR proteins

Bin-Amphiphysin-Rvs (BAR) name comes from the three proteins that contain this type of domain. BAR domains are dimers having the shape of a banana represented in Fig. 1.7a. They play a dual role; they can both sense membrane curvature and induce an anisotropic curvature to the membrane along the concave surface of their domain [20]. The BAR domain-membrane interaction is an electrostatic one and BAR proteins only bind to negatively charged membranes. Since they bind only to the surface of the membrane, these proteins are part of the peripheral membrane proteins group. BAR proteins exhibit different sorts of BAR domains (see Fig. 1.7) which give different mechanisms and roles to them [21].

When a BAR domain is modified at its N-terminal, *i.e.*, a group with a free amine (-NH2) which can be found at both ends of the domain, it is called an N-BAR domain

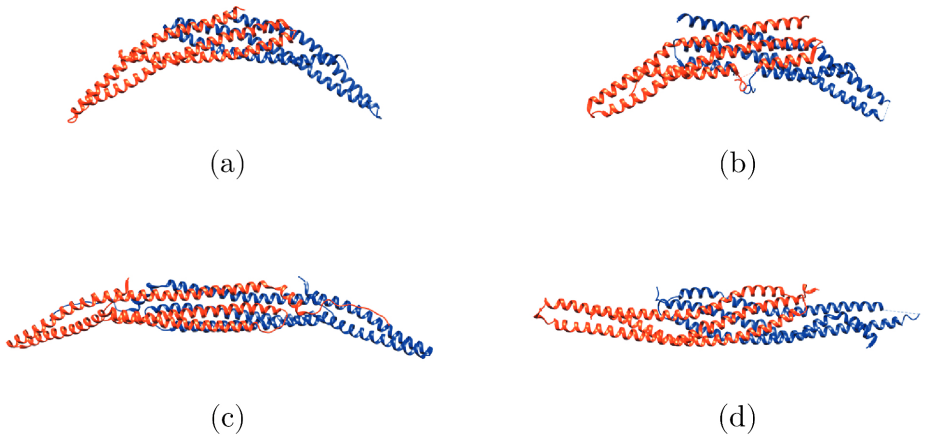

Figure 1.7 – BAR domains dimer of the BAR superfamily proteins. Here only the BAR domains of these proteins are shown. (a) The classical BAR domain. (b) N-BAR domain where an N-terminal region sequence is added at one end of the BAR domain (see text, N-terminal not visible here). (c) The F-BAR domain is longer and shallower than the previous domains. (d) I-BAR domains impose an opposed curvature with respect to the other domains. *Illustrations adapted from [21].*

(see Fig. 1.7b). These proteins are mainly found in the mammalian nerve cells where they are involved in synapse formation and signal transduction [22]. The N-terminal evoked here is an amphiphilic α helix [23] that acts as an anchor: it can use its amphipathic property to be embedded in the membrane where it reshapes the latter locally by moving the phospholipids around in order to induce a favorable curvature for the protein to bind to the membrane [20, 24]. Therefore, N-BAR proteins generate curvature through two mechanisms: scaffolding and wedging [25, 26], also called hydrophobic insertion. While the latter mechanism is induced when the N-terminal sequence is (deeply) inserted into one monolayer as described above, scaffolding occurs through the binding of the BAR domain to one of the two leaflets. The protein being rigid and curved, it imposes therefore locally its curvature on the membrane along its long axis. Note that we use scaffolding both to deal with the binding of a single BAR domain and the collective effect of BAR proteins on the membrane indifferently. Depending on the strength of these mechanisms (*i.e.*, the imposed curvature), N-BAR proteins can induce either membrane tubulation associated with an anisotropic curvature or vesiculation associated with a (collective) isotropic curvature [25, 27, 28]. The length of proteins containing a classical BAR domain is approximately 20 nm [29] and the radius of curvature they impose to the membrane was measured in the range $11 - 30$ nm experimentally [24, 30, 31] giving a curvature C_0 around $0.05\,\mathrm{nm}^{-1}$.

F-BAR domains shown in Fig. 1.7c are quite similar to classical BAR domains. Like the latter, they have an N-terminal called Fes/CIP4 homology (FCH) domain [32] and have a crescent shape. However, their N-terminal group doesn't play a role in curvature induction [33]. Moreover, these proteins are longer than classical BAR domains, as their length is around 30 nm [34], and are also thrice shallower having a radius of curvature in the range $30-50$ nm [31, 33, 35] which gives a curvature C_0 of approximatively $0.02\,\mathrm{nm}^{-1}$.

Figure 1.8 – Binding mechanisms of BAR proteins. (a) scaffolding which occurs when the protein bind to the membrane through its BAR domain. (b) wedging or hydrophobic insertion where the protein bind to the membrane using its N-terminals. *Illustrations adapted from [24].*

These proteins are present in all eukaryotes excluding plants and play a role in several biological processes such as clathrin-mediated endocytosis [25, 34]. This transport process allows some compounds to cross the membrane towards the cell thanks to the invagination of the membrane that forms a clathrin-coated vesicle.

The last important BAR domain is the Inverse (I-) BAR domain represented in Fig. 1.7d. As its name suggests, these proteins induce a curvature along their convex region, *i.e.*, they induce an opposed curvature with respect to other BAR domains [25, 36]. They are involved in several processes where they induce or stabilize the negative curvature, *e.g.*, they are found along with N-BAR proteins during synapse formation [22]. Like F-BAR domains, their arc is shallower, almost flat and they are elongated [25].

b. KvAP channels

Transmembrane proteins can also induce curvature. It is the case, for instance, of the KvaP proteins. KvAP proteins are part of the voltage-gated ion channels, more specifically the potassium channels. Ion channels are proteins that allow the transfer of ions from one side of the membrane to the other along their concentration gradient (see Fig. 1.9). There exist two types of ion channels: non-gated channels which are never closed and gated channels which stay closed until they receive a chemical or electrical signal. The voltage-gated channels change their state by sensing the transmembrane voltage; they remain close when the inner part, *i.e.*, the interior of the cell, is more negative than the outer part and open in the opposite case.

KvAP, like sodium and calcium gated ion channels [37], is a tetramer, *i.e.*, it is composed of four identical subunits as shown in Fig. 1.9a. Each subunit contains six α helices of which four are dedicated to transmembrane voltage sensing and the last two are part of the pore domain that is the central part of the protein [38]. The voltage-gated potassium channels play a key role in the regulation of cellular excitability; while they depolarize the membrane and thus induce an excitation when they are closed, they are responsible for quiescence when their channel is opened [39].

The interplay between membrane curvature and KvAP distribution was highlighted by observing their behavior as a function of membrane curvature [42]. To do so, a giant unilamellar vesicle (GUV) – a spherical vesicle composed of a single bilayer – is held by

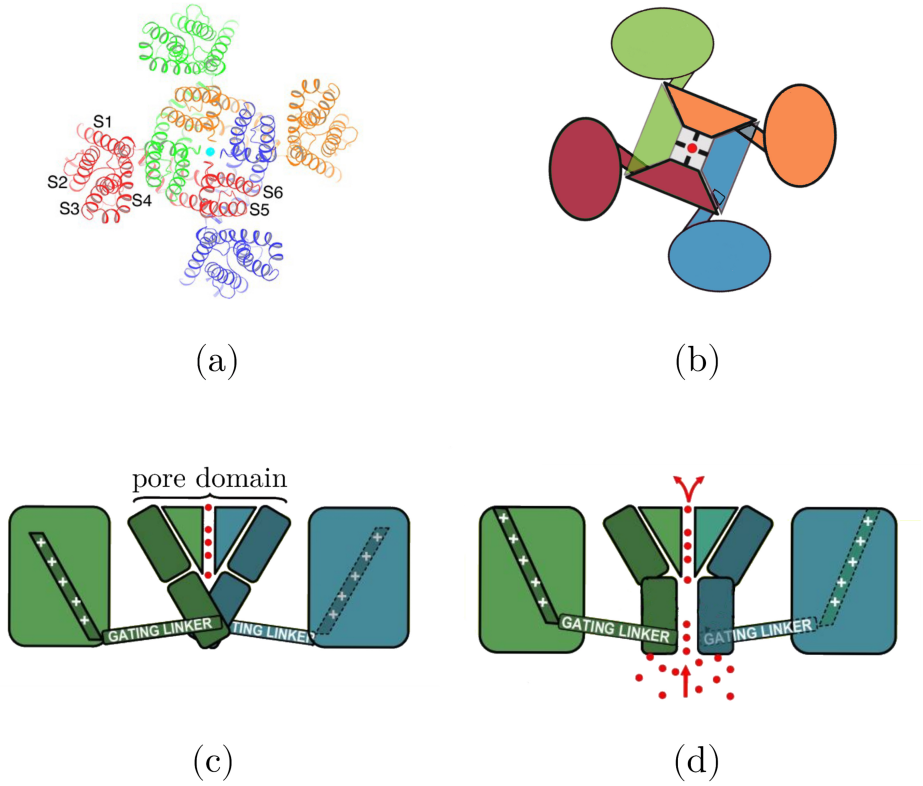

Figure 1.9 – KvAP structure. Top view of the KvAP structure (a) and its simplified representation (b). A color has been assigned to each subunit. The helices S1 to S4 compose the voltage sensor group. S5 and S6 are part of the pore domain which forms the channel for ions. The bond between S4 and S5 links these two groups. Schematic side view of the protein when the channel is closed (c) and when it is opened (d). When the protein receives a signal to open, its pore domain change conformation to let the ions pass. *(a) is extracted from [40] and the illustrations are adapted from [41].*

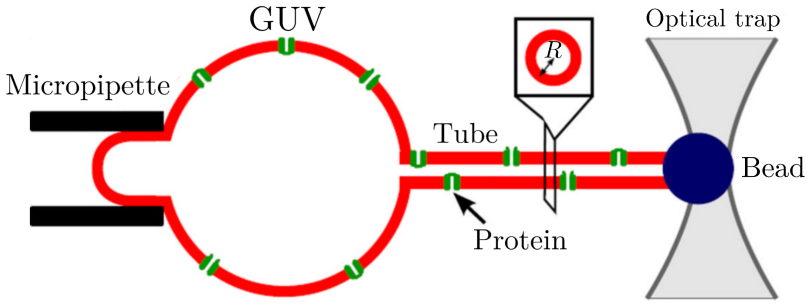

Figure 1.10 – Schematic representation of the experimental setup used to highlight the KvAP curvature dependence. A GUV (kind of planar membrane) is held by a micropipette while a bead in an optical trap pulls out a membrane tube (curved membrane). *Adapted from [42].*

a micropipette, and a membrane tube of radius R is pulled out from the GUV to form a curved membrane. One can observe that KvAP proteins prefer to occupy the curved membrane. A schematic representation of the experiment performed in [42] is shown Fig. 1.10. The size of KvAP is around 4 nm and its spontaneous curvature measured is approximatively $C_0 = 0.04\,\mathrm{nm}^{-1}$ experimentally [42, 43] as well as numerically [44].

c. ABC transporters - BmrA

Our last example is the BmrA protein that belongs to the superfamily of ATP-binding cassette (ABC) transporters. ABC transporters are transmembrane proteins that are composed of two subunits, each containing a transmembrane domain (TMD) that spans the bilayer, a nucleotide-binding domain (NBD) and an intracellular domain (ICD) that links the two previous domains (see Fig. 1.11). TMDs selectively bind substrates to the proteins to transport them either towards or away from the cell if the ABC transporter is an importer or an exporter respectively [45], the latter being more common. NBDs, as its name suggests, can bind nucleotides and more precisely adenosine triphosphate (ATP) which is the energy source of several essential biological processes.

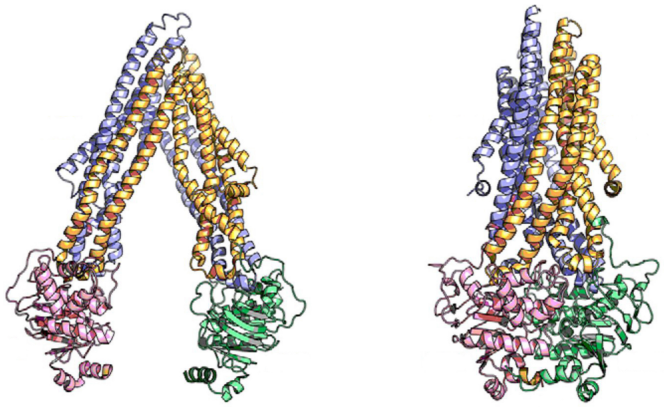

(a) (b)

Figure 1.11 – ABC transporter architecture. All ABC transporters share a common structural organization, especially the P-glycoprotein (P-gp) represented here is homologous to the BmrA protein [46]. (a) Inward-facing (IF) conformation. In this conformation, the ABC transporter has a V-shape. (b) Outward-facing (OF) conformation where the proteins take a rectangular shape. The purple and yellow helices are the TMD. The end of these domains as well as the filaments constitutes the ICDs linking the former domains with the two NBDs colored in pink and green. *Illustrations adapted from [47].*

BmrA stands for Bacillus multidrug resistance ATP as this ABC transporter endows (multi-) drug resistance with cells binding several drugs and exporting them outside the cell. Although this is essential to maintain healthy cells, multidrug resistance prevents the drugs used in chemotherapy from healing cancerous cells [48].

The ATPase cycle of the BmrA protein [49] represented Fig 1.12 begins with the protein in the IF conformation where it binds substrates inside its TM domains. When ATP nucleotides are added, the NBD capture them which induces dimerization of the two NBDs, *i.e.*, they merge, changing the conformation of the protein from inward-facing (IF)

to outward-facing (OF) conformation where the substrates can be expelled outside the cell. Finally, by ATP hydrolysis, the two NBD sites are dissociated releasing adenosine diphosphate and restoring the IF initial state of the protein.

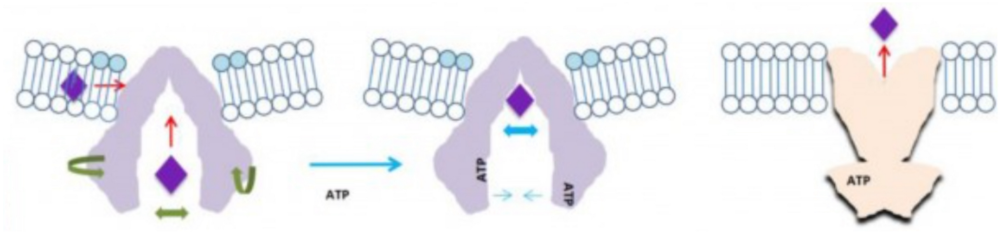

Figure 1.12 – ATP cycle of the BmrA protein. First compounds (purple lozenges) bind to the protein (light purple inverted V). In presence of ATP, the latter nucleotides are caught by NBDs. This binding induces the dimerization of the two NBDs and so the protein changes its conformation towards the outside of the cell where the substrate is expulsed. *Illustration extracted from Team Lévy, Institut Curie.*

As can be seen in Figs 1.12, 1.13a, when the BmrA is in its IF conformation it induces a curvature of the membrane in order to satisfy its boundary conditions. From the BmrA rings given in [50] one can deduce the size and spontaneous curvature of BmrA proteins. The size is around 5 nm and the ring radius is 27 nm giving a spontaneous curvature of $0.04\,\mathrm{nm}^{-1}$ approximatively.

1.3.3 Casimir-like interactions in biological membranes

Since proteins curve the membranes, membrane-proteins interactions are elastic. However, there are also Casimir-like interactions between proteins and biological membranes.

The Casimir force was identified by Casimir in 1948 when he studied the interaction between two perfectly conducting plates in vacuum [51]. Casimir determined that this interaction is attractive and exists even in the absence of a charge or any external electromagnetic field, and at zero temperature. In fact, the boundary conditions imposed by the plates on the zero-point fluctuations of the electromagnetic field constrain a component

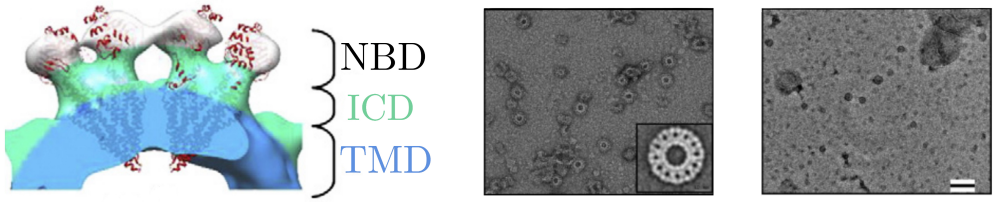

(a) (b) (c)

Figure 1.13 – Change of conformation of BmrA. In its IF conformation and at a high enough concentration BmrA forms rings (b). When it is in presence of ATP, the rings disappear as the BmrA proteins switch their state to OF with a conformation that does not curve the membrane (c). (a) shows a 3D model of such BmrA rings that curve the membrane (TMD). *The 3D model and the electron microscopy experiment images are extracted from [50] and [49] respectively.*

of the field to vanish on the former, so they prevent the existence of some field modes inside the cavity. Since these modes are allowed to exist outside the cavity (see Fig. 1.14), an (attractive) interaction arises between the plates.

Since then, several manifestations of Casimir-like interactions have been reported in Soft Matter [52, 53]. In biological membranes, these interactions come from the boundary conditions imposed by proteins on the fluctuations of the membrane shape [54]. Let us consider two disk proteins of radius a at distance R. In this case, the Casimir interaction is given by [55]

$$F_C = -6k_{\mathrm{B}}T\frac{a^4}{R^4} + O\left(\frac{a^6}{R^6}\right), \tag{1.4}$$

which is an attractive long-range interaction.

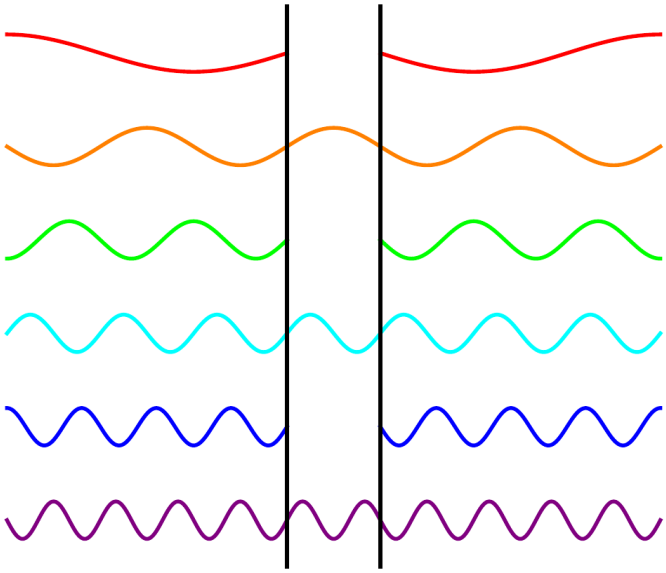

Figure 1.14 – Representation of the Casimir effect. All field modes shown in color exist outside the cavity but, to ensure the field vanishing condition on the two plates, some field modes can't exist inside the cavity, leading to the generation of an attractive interaction between the plates. *Illustation extracted from [56]*

Chapter 2

How to model a membrane?

In this chapter, we aim to model a membrane containing proteins from a physical point of view. We shall first model the membrane without proteins and then consider the coupling with proteins. After the description of the statics, we present the dynamics of the system.

2.1 Statics

2.1.1 Canham-Helfrich Hamiltonian

In 1973, Helfrich elaborated a physical modelization of the lipid bilayer based on the elastic properties of the latter [57]. In this model, Helfrich kept only the membrane bending energy arguing the latter dominates the stretching one in (almost) every case. Notably, he calculated the bending and stretching energy of a spherical vesicle using his model and showed that the stretching can be neglected with respect to the bending [57]. Therefore, in the case of a closed bilayer membrane with a fixed number of phospholipids (*e.g.*, vesicles), disregarding stretching corresponds to keeping a fixed area and the system undergoes only bending deformations, *i.e.*, curvature.

The local curvature of a bilayer membrane can be described by a tensor of rank 2 called the curvature tensor. Its eigenvalues, c_1 and c_2, are called the principal curvatures (see Fig. 2.1). The trace c_1+c_2 and the determinant c_1c_2 are called the total curvature and the Gaussian curvature, respectively. Since the membrane bending energy is a scalar, *i.e.*, it does not depend on the chosen frame , it can only depend on the total curvature and Gaussian curvature as they are the two invariants of the curvature tensor [58]. Helfrich introduced the membrane Hamiltonian

$$\mathcal{H}_0 = \int_A \mathrm{d}A \left[\frac{\kappa}{2}\left(c_1 + c_2 - c_0\right)^2 + \bar{\kappa}\, c_1 c_2\right], \tag{2.1}$$

where A is the membrane area, κ and $\bar{\kappa}$ are the bending modulus and saddle-splay modulus, respectively, and c_0 is the spontaneous curvature emerging from the asymmetry between the two monolayers as explained in the previous chapter. The first term ac-

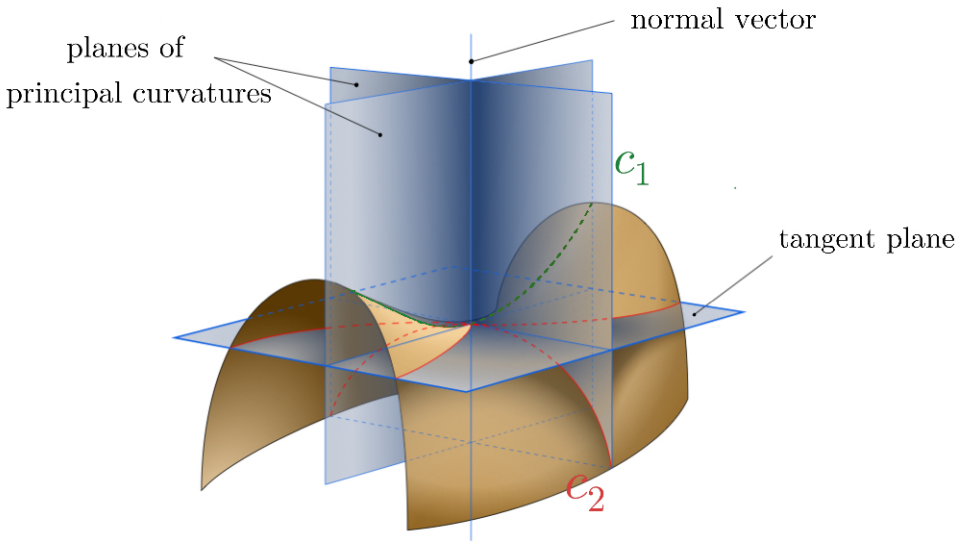

Figure 2.1 – Representation of the planes of the two principal curvatures c_1 and c_2 at a saddle point on a surface (in gold). The principal curvatures depend on the choice of the basis we use, unlike the mean and Gaussian curvatures that are invariant under a change of basis. *Illustration extracted and adapted from Wikipedia.*

counts for the energetic cost due to the difference between the total curvature and the spontaneous curvature of the membrane, the second term comes from the Gaussian curvature. While the bending modulus is always positive, the sign of the saddle-splay modulus can be either positive or negative. Moreover, to guarantee membrane stability it can be shown that the saddle-splay modulus should be between -2κ and 0 [58].

It is worth noting that the Helfrich Hamiltonian we presented above is sometimes called the Canham-Helfrich Hamiltonian, as Canham used a similar Hamiltonian in 1970 to study the membrane of blood cells [59]:

$$\mathcal{H}_0 = \int_A \mathrm{d}A\, \kappa \left[\frac{1}{2}(c_1 + c_2)^2 - c_1 c_2\right], \tag{2.2}$$

where the main difference with the Helfrich Hamiltonian is the lack of a saddle-splay modulus, or more precisely, it is assumed that $\bar{\kappa} = -\kappa$. The other difference–a zero spontaneous curvature c_0–comes from the assumption of a symmetric bilayer. For the sake of simplicity, we will assume the same in the following.

Fortunately, these two Hamiltonians will give the same energy for membranes thanks to the Gauss-Bonnet theorem. This theorem states that the Gaussian curvature contribution is a constant for a closed surface:

$$\int_A \mathrm{d}A\, c_1 c_2 = 2\pi\chi, \tag{2.3}$$

where χ is the Euler characteristic of the system, *i.e.*, it is a number that depends only on the topological shape of the system. Since we assume that the membrane does not change its topology, it is a constant that can be disregarded. It is worth noting that even if proteins generate local "holes" in the membrane, if they keep a fixed shape, *i.e.*, the

contact angle between the membrane and a protein is fixed, the geodesic curvature is a constant and, thereby, the Gauss-Bonnet theorem holds (see Erratum of [60]). Keeping only the contribution of the total curvature, we see that the two Hamiltonians are the same for membranes in the case of zero spontaneous curvature.

Now, let us consider a patch of the membrane which is in contact with a reservoir of lipids (*e.g.*, in the case of a membrane patch of a vesicle, the rest of the vesicle plays the role of the lipids reservoir). We impose a fixed projected area A_p for the patch that corresponds to the projection of the curved membrane on a parallel plane (see Fig. 2.2). Therefore, stretching does not play any role and the appropriate thermodynamic ensemble to describe the membrane is the grand canonical ensemble where the number N of molecules can fluctuate and a chemical potential μ is imposed on the system. Thus the appropriate Hamiltonian is

$$\mathcal{H}_0' = \mathcal{H}_0 - \mu N = \mathcal{H}_0 + \sigma A, \tag{2.4}$$

where we introduced the effective surface tension $\sigma = -\mu/a_0$ of the lipid reservoir with a_0 the area per lipid, assumed fixed (k_s large in Eq.(1.1)).

Finally, gathering all elements, the Hamiltonian we use in the following to describe the bilayer membrane is

$$\mathcal{H}_0 = \int_A \frac{\kappa}{2} (c_1 + c_2)^2 \, \mathrm{d}A + \sigma A. \tag{2.5}$$

We recall that the order of magnitude of κ is $30\, k_\mathrm{B}T$ and σ is in the range $10^{-8} - 10^{-3}\,\mathrm{N/m}$.

2.1.2 Monge parametrization

To describe the bilayer membrane effectively, we need to define its parametrization, *i.e.*, a mapping of its surface to a field that specifies its variations. We use the so-called Monge parametrization where the bilayer membrane is described by its height field $h(x, y)$ where the Cartesian coordinates x and y are the coordinates in a reference plane (see Fig. 2.2):

$$h : \begin{cases} \mathbb{R}^2 \to \mathbb{R} \\ (x, y) \to h(x, y) \end{cases} \tag{2.6}$$

Introducing the vector $\boldsymbol{n}$ normal to the surface, the curvature tensor $\boldsymbol{K}$ is the rate of change of the normal vector when one makes a displacement $\mathrm{d}\boldsymbol{r}$ along the membrane surface, *i.e.*,

$$\mathrm{d}\boldsymbol{n} = \boldsymbol{K} \cdot \mathrm{d}\boldsymbol{r}. \tag{2.7}$$

As straightforward as this parametrization is, it has a major drawback: it cannot hold "overhangs", *i.e.*, the height field cannot be multivalued. Nevertheless, we are only interested in small deformations. Thereby, we consider deformations such that $\partial_i h = O(\epsilon)$ and $e\,\partial_i \partial_j h = O(\epsilon)$ with $i, j \in \{x, y\}$ and e the bilayer thickness. To determine the curvature tensor, we introduce the function $\Phi(x, y, z) = h(x, y) - z$ such that it vanishes

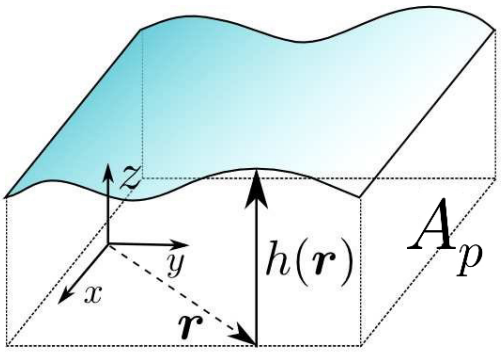

Figure 2.2 – Sketch showing the parametrization of a surface (in shaded blue) in the Monge gauge. The area of the square formed by the projection of the surface is A_p. The height of the surface is given by the field $h(x, y)$. *Extracted from [61].*

on the membrane surface. Therefore the unit vector $\boldsymbol{n}$ normal to the surface is along $\boldsymbol{\nabla}\Phi$, and for small deformations, to first order in ϵ

$$\boldsymbol{n} \propto \boldsymbol{\nabla}\left[h(x,y) - z\right] \simeq \begin{pmatrix} \partial_x h \\ \partial_y h \\ -1 \end{pmatrix} \tag{2.8}$$

We can then determine $\mathrm{d}\boldsymbol{n}$ and so the curvature tensor $\boldsymbol{K}$:

$$\mathrm{d}\boldsymbol{n} = \begin{pmatrix} \mathrm{d}(\partial_x h) \\ \mathrm{d}(\partial_y h) \end{pmatrix} = \begin{pmatrix} \partial_x h \partial_x h & \partial_y h \partial_x h \\ \partial_x h \partial_y h & \partial_y h \partial_y h \end{pmatrix} \begin{pmatrix} \mathrm{d}x \\ \mathrm{d}y \end{pmatrix}, \tag{2.9}$$

$$\boldsymbol{K} = \begin{pmatrix} \partial_x h \partial_x h & \partial_y h \partial_x h \\ \partial_x h \partial_y h & \partial_y h \partial_y h \end{pmatrix}, \tag{2.10}$$

where the matrix on the rhs is the expression of the curvature tensor in the Monge parametrization. Note that the trace and the determinant of this tensor are the total curvature and the Gaussian curvature, respectively and

$$c_1 + c_2 \simeq \nabla^2 h. \tag{2.11}$$

We now focus on the expression of the infinitesimal area element $\mathrm{d}A$ in the Monge gauge. The element of surface can be written in Cartesian coordinates by starting with a point S on the surface at position $(x, y, h(x, y))$, we construct the vectors $S\vec{S}_x$ and $S\vec{S}_y$ such that their coordinates are approximatively $(1, 0, \partial_x h)\,\mathrm{d}x$ and $(1, 0, \partial_y h)\,\mathrm{d}y$, respectively. The parallelogram formed by these two vectors corresponds to the element of the surface and its area $\mathrm{d}A$ is given by their cross product [62]:

$$\mathrm{d}A = |S\vec{S}_x \times S\vec{S}_y| = \sqrt{1 + (\boldsymbol{\nabla}h)^2}\,\mathrm{d}x\mathrm{d}y \simeq \left(1 + \frac{1}{2}(\boldsymbol{\nabla}h)^2\right)\mathrm{d}x\mathrm{d}y, \tag{2.12}$$

where the approximation is done to second order in the derivatives of h ($\epsilon \sim \partial_i h$). We

thus can rewrite the area A using the projected area A_p:

$$A = \int_{A_p} \mathrm{d}A \simeq \int_{A_p} \frac{1}{2}(\boldsymbol{\nabla} h)^2 \,\mathrm{d}x\mathrm{d}y, \tag{2.13}$$

up to a constant.

Finally, the Hamiltonian for the membrane bilayer in the small gradient approximation (second order in ϵ) is given by

$$\mathcal{H}_0 = \frac{1}{2}\int_{A_p} \mathrm{d}^2 r \, \left[\kappa(\nabla^2 h)^2 + \sigma(\boldsymbol{\nabla} h)^2\right], \tag{2.14}$$

where $\mathrm{d}^2 r = \mathrm{d}x\,\mathrm{d}y$.

2.1.3 Membrane-protein coupling

We now focus on the coupling between the membrane and the proteins embedded in the bilayer. As explained in the last chapter, the proteins can deform membranes when they bind to them as well as sense their curvature. Therefore, the deformations a membrane undergoes due to some protein generate elastic forces that affect other proteins, *i.e.*, proteins interact with each other via the membrane field deformations (see Fig 2.3). These kinds of indirect interactions between objects conveyed by the change of a field of matter are called mediated interactions [55].

In the literature, to model the coupling between a membrane and proteins that curve it upon binding, authors commonly use a quadratic coupling [64–69]. Having in mind the bending energy that describes the curvature of a membrane, it is straightforward to determine that a quadratic coupling between an isotropic protein at position $\boldsymbol{r}_p$ and a membrane takes a form similar to

$$\mathcal{H}_{\text{int}} = \frac{1}{2}\int_{A_p} \mathrm{d}^2 r \, \kappa_p \, G(\boldsymbol{r} - \boldsymbol{r}_p) \left(\nabla^2 h - 2c_0\right)^2, \tag{2.15}$$

where c_0 is the favored curvature by the protein along its principal curvatures, *i.e.*, proteins impose an isotropic curvature to the membrane, κ_p is the strength of the coupling; the greater it is, the closer the membrane curvature is to c_0. $G(\boldsymbol{r})$ corresponds to the coupling region between a protein and the membrane. Here, we have deliberately omitted the contribution of the Gaussian curvature for the sake of presentation. This quadratic potential is a good approximation of higher-order potentials in the small gradient approximation where the membrane deformations and fluctuations are kept small [64].

It is noteworthy that a linear potential can be used to describe the membrane-proteins coupling [43, 64, 69]. Such a coupling is written

$$\mathcal{H}_{\text{int}} = -\frac{1}{2}\int_{A_p} \mathrm{d}^2 r \, \kappa_p G(\boldsymbol{r} - \boldsymbol{r}_p) \, c_0 \nabla^2 h. \tag{2.16}$$

This expression appears clearly as an approximation of the quadratic potential to the first order in $\nabla^2 h$, up to an additive contribution. While a linear coupling implies simpler

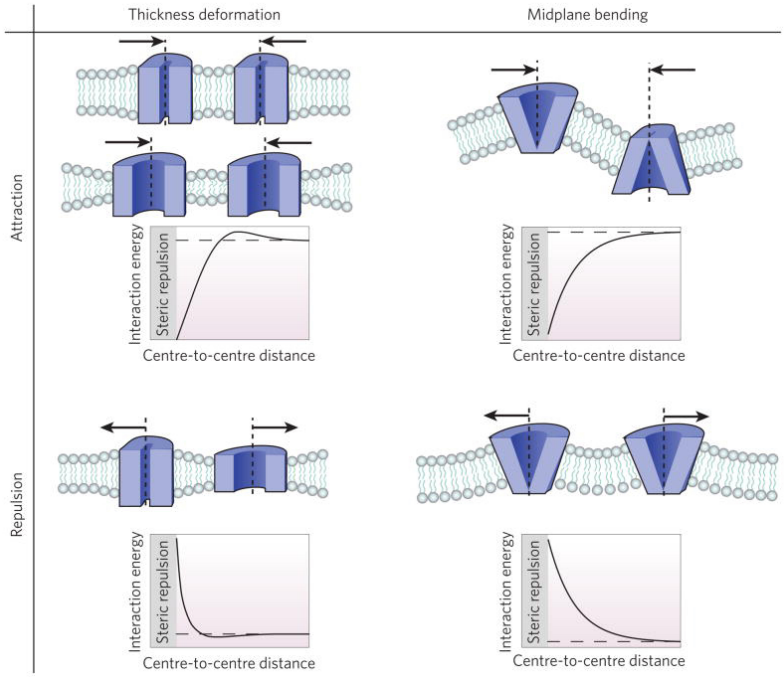

Figure 2.3 – Sketch of different sorts of mediated interactions between two proteins (purple) embedded in a membrane (light grey). The black arrows show the direction of the force acting on each protein. Here we see that proteins can interact either via a change of membrane thickness (on the right) or via membrane bending (on the left). Since we assume a bidimensional membrane, we will only consider the latter case. *Extracted from [63].*

computations, it cannot account for multi-body interactions [64] which can be essential for mediated interactions. Therefore it can be considered only to study the behavior of a single protein [43].

We now aim at giving a more specific expression of the membrane-proteins coupling, especially by specifying the coupling region encoded by $G(\boldsymbol{r})$. Commonly, proteins are assumed to be either cylinders or cones that become disks when the membrane thickness is neglected [19, 70]. In this case, the first and straightforward way to model the area of coupling is to assume that $G(\boldsymbol{r})$ is a Gaussian kernel [65–67]: (see Fig. 2.4a)

$$G(\boldsymbol{r}) = \mathrm{e}^{-\frac{\boldsymbol{r}^2}{a_p^2}}, \tag{2.17}$$

with a_p the protein radius which is also the radius of the coupling area. However, as noted in [68], a Gaussian function to describe the envelope function $G(\boldsymbol{r})$ is irrelevant as it doesn't define a clear envelope where the protein influence the membrane but rather leads to a normalization varying with the strength κ_p. A more suitable choice is therefore to consider a series of envelope functions for $G(\boldsymbol{r})$ [68] (see Fig. 2.4b). Furthermore, since proteins curve the membrane on their envelope function, the membrane can be seen as a mixture of bound sites where a protein imposes a deformation and unbound sites where the membrane tends to adopt its spontaneous curvature. Therefore one has to remove the binding energy on places where the proteins bind [66, 68]. As the envelope is

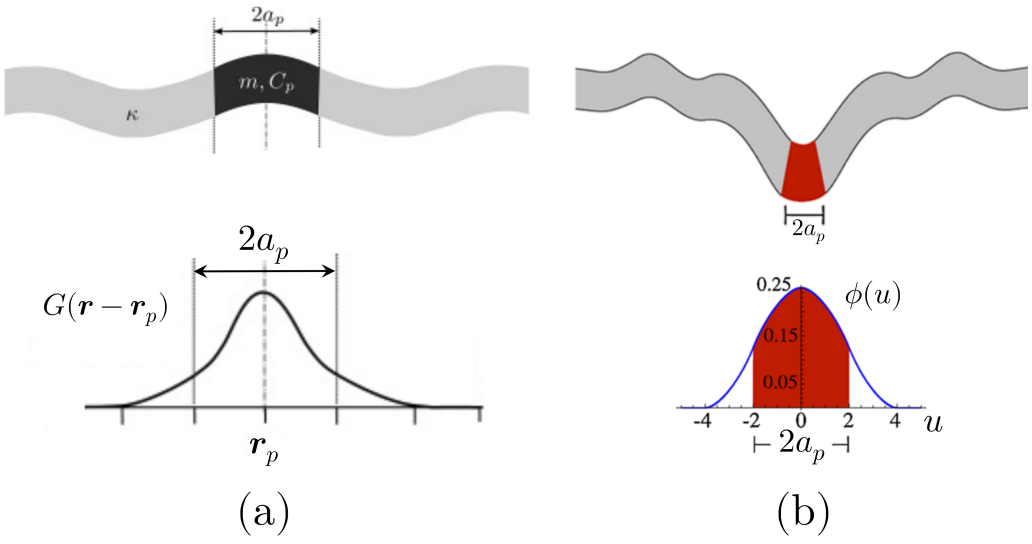

Figure 2.4 – Representation of different coupling region function $G(\boldsymbol{r})$ for a protein of radius a_p and located at position $\boldsymbol{r}_p$. (a) a Gaussian coupling function $G(\boldsymbol{r})$ is wider than the more sophisticated function (b) $G(\boldsymbol{r}) \propto \phi(x)\phi(y)$, with ϕ a piecewise function given in [68]. *Extracted and adapted from [67] and [68], respectively.*

space-dependent, the integral of the Gaussian curvature is no more a constant, *i.e.*, the Gauss-Bonnet theorem does not hold for integrands that vary locally in space. Thus the interaction energy takes the form

$$\mathcal{H}_{\text{int}} = \int_{A_p} \mathrm{d}^2 r\, G(\boldsymbol{r}-\boldsymbol{r}_p) \left[\frac{\kappa_p}{2} \left(\nabla^2 h - 2c_0 \right)^2 - \frac{\kappa}{2} (\nabla^2 h)^2 + (\bar{\kappa}_p - \bar{\kappa}) \det \boldsymbol{K} \right], \tag{2.18}$$

where $\bar{\kappa}$ and $\bar{\kappa}_p$ are the saddle-splay moduli of the membrane and the proteins, respectively, associated with the Gaussian curvature $\det \boldsymbol{K}$ which is the determinant of the matrix of Eq. (2.9).

Finally, for the sake of simplicity, proteins can be assumed to be pointlike. This is the assumption made in the following. In this case, the envelope function $G(\boldsymbol{r})$ reduces to a Dirac delta function $\delta(\boldsymbol{r})$. Since the envelope is pointlike, it is useless to remove the bending energy where proteins bind to the membrane. Furthermore, in the case of an isotropic curvature imposed by proteins and assuming that the splay-modulus $\bar{\kappa}_p = -\kappa_p$, we can write

$$(\partial_i \partial_j h - c_0 \delta_{ij})(\partial_i \partial_j h - c_0 \delta_{ij}) = (\nabla^2 h - 2c_0)^2 - 2\left(\partial_x^2 h)(\partial_y^2 h) - (\partial_x \partial_y h)^2 \right), \tag{2.19}$$

up to irrelevant boundary terms. The tensor $(\partial_i \partial_j h(\boldsymbol{r}) - c_0 \delta_{ij})$ corresponds to the deviation between the curvature tensor and the isotropic curvature c_0 at position $\boldsymbol{r}$. Note that it is possible to consider proteins with different curvatures c_n corresponding to the curvature favored by the nth protein. Considering N proteins located at positions $\boldsymbol{r}_n$,

the interaction can thus be written

$$\mathcal{H}_{\text{int}} = \frac{\kappa_p}{2}\sum_{n=1}^{N}\int_{A_p} \mathrm{d}^2 r\, \delta(\boldsymbol{r}-\boldsymbol{r}_n)(\partial_i\partial_j h - c_n\delta_{ij})(\partial_i\partial_j h - c_n\delta_{ij}) = \frac{\kappa_p}{2}\sum_{n=1}^{N} K_{ij}^{(n)}K_{ij}^{(n)}, \quad (2.20)$$

where $K_{ij}^n = \partial_i\partial_j h|_{\boldsymbol{r}_n} - c_n\delta_{ij}$ is the deviation between the curvature tensor at the location of the nth protein and its isotropic favored curvature c_n. In what follows, the complete Hamiltonian of the system will be given by

$$\mathcal{H} = \mathcal{H}_0 + \mathcal{H}_{\text{int}} = \frac{1}{2}\int_{A_p} \mathrm{d}^2 r\, \left[\kappa(\nabla^2 h)^2 + \sigma(\boldsymbol{\nabla} h)^2\right] + \frac{\kappa_p}{2}\sum_{n=1}^{N} K_{ij}^{(n)}K_{ij}^{(n)}. \quad (2.21)$$

The order of magnitude of the coupling strength κ_p can be obtained by comparing the coupling energy to the bending energy in terms of order $(\nabla^2 h)^2$. To do so, we form the dimensionless ratio R_p such that $R_p = \kappa_p/(\kappa\pi a_p^2)$, where the numerator comes from the interaction energy and the denominator is obtained by integrating the bending energy for a disk of radius a_p supposed to be the "true" shape of the assumed pointlike proteins. Therefore, for $a_p \simeq 10\,\text{nm}$, a value $\kappa_p \simeq 3\times10^{-17}\,\text{Jnm}^2$ corresponds to a coupling strength comparable to the bending strength.

2.2 Dynamics

2.2.1 Dynamics of a membrane in a solvent

We consider a membrane as an infinite two-dimensional incompressible fluid with viscosity η_2 surrounded on both sides by an incompressible bulk solvent (water) with viscosity η (see Fig. 2.5). Since the latter is viscous, we neglect the inertial forces and work at low Reynolds number. Therefore, the dynamics of the solvent can be described by the well-known Stokes equations supplemented with conditions expressing the incompressibility of the fluids:

$$\eta\nabla^2\boldsymbol{V}^{\pm} - \boldsymbol{\nabla}P^{\pm} = 0, \quad (2.22)$$

$$\boldsymbol{\nabla}\cdot\boldsymbol{V}^{\pm} = 0, \quad (2.23)$$

where the $\pm$ subscript refers to the upper $(+)$ or lower $(-)$ solvent bulk, $\boldsymbol{V}^{\pm}$ is the fluid velocity, and $P^{\pm}$ its pressure.

Since the membrane is a fluctuating surface, we should describe its dynamics both in-plane, *i.e.*, along its surface, and across its normal (z-direction). While the former corresponds to the lateral displacements of lipids in the membrane, the latter encodes the transversal deformations undergone by the membrane. Since the membrane is also a viscous incompressible fluid, its in-plane dynamics is given by [71, 72]

$$\eta_2\bar{\nabla}^2\boldsymbol{v} - \bar{\boldsymbol{\nabla}}p + \boldsymbol{\sigma}^+ + \boldsymbol{\sigma}^- = \boldsymbol{0},, \quad (2.24)$$

$$\bar{\boldsymbol{\nabla}}\cdot\boldsymbol{v} = 0, \quad (2.25)$$

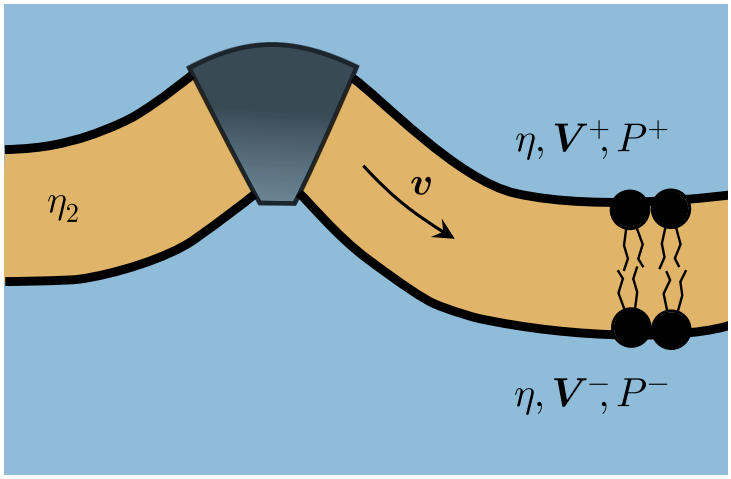

Figure 2.5 – Sketch of an infinite membrane (orange) surrounded by a bulk (sky blue) of viscosity η. While the membrane has a thickness on the sketch, it is assumed to be a 2D fluid of viscosity η_2 with field velocity $\boldsymbol{v}(\boldsymbol{r})$. Here a conical protein (dark grey) is embedded in the membrane.

where $\bar{\boldsymbol{\nabla}} = \partial_x \boldsymbol{e}_x + \partial_y \boldsymbol{e}_y$ is the in-plane gradient operator, $\boldsymbol{v}$ is the velocity of the bi-dimensional lipidic fluid and p is its pressure. One recognizes that the first two terms of Eq. (2.24) correspond to the Stokes equations. As the membrane is surrounded by another fluid, we add the tangential viscous stresses $\boldsymbol{\sigma}^\pm = \pm\eta(\partial_z \boldsymbol{V}^\pm + \bar{\boldsymbol{\nabla}} V_z^\pm)|_{z=0}$ transmitted by the solvent to the bi-dimensional membrane fluid, where $z = 0$ is the coordinate of the tangential plane. Again, the second equation conveys the incompressibility of the fluid.

In the transverse plane, the membrane is subjected to the elastic deformations $-\frac{\delta \mathcal{H}_0}{\delta h}$ coming from thermal fluctuations, and to the transverse viscous stresses $\Sigma^\pm = \pm(2\eta\partial_z V_z^\pm - P^\pm)|_{z=0}$. Therefore, the transversal dynamics of the membrane is given by

$$-\frac{\delta \mathcal{H}_0}{\delta h} + \Sigma^+ + \Sigma^- = 0, \tag{2.26}$$

where the Hamiltonian $\mathcal{H}_0$ is given by Eq. (2.14).

Finally, we assume no-slip boundary conditions between the membrane and the solvent. Thus, the continuity equations between the fluids are

$$\boldsymbol{v} = \boldsymbol{V}^\pm|_{z=0}, , \tag{2.27}$$
$$\dot{h} = V_z^\pm|_{z=0}, \tag{2.28}$$

where the first equation corresponds to the in-plane continuity and the second one, to the transverse continuity.

2.2.2 Dynamics of the proteins embedded in a membrane

We now add pointlike curvature-inducing proteins located at position $\boldsymbol{r}_n$ and favoring a local isotropic curvature c_n. When these proteins bind, they induce a curvature to the membrane which leads to local deformations in the transverse plane through the (modified) elastic forces $-\frac{\delta \mathcal{H}}{\delta h}$, with $\mathcal{H} = \mathcal{H}_0 + \mathcal{H}_{\text{int}}$ given by Eq. (2.21). In turn, these

local deformations impact the in-plane dynamics where the forces $-\frac{\partial \mathcal{H}}{\partial \boldsymbol{r}_n}$ are applied to each protein. Therefore, the in-plane (Eq. (2.24)) and transverse (Eq. (2.26)) dynamics of a membrane surrounded by a bulk fluid in the presence of proteins become

$$\eta_2 \bar{\nabla}^2 \boldsymbol{v} - \bar{\boldsymbol{\nabla}} p + \boldsymbol{\sigma}^+ + \boldsymbol{\sigma}^- - \sum_n \frac{\partial \mathcal{H}}{\partial \boldsymbol{r}_n} \delta(\boldsymbol{r} - \boldsymbol{r}_n) = \boldsymbol{0}, \tag{2.29}$$

$$-\frac{\delta \mathcal{H}}{\delta h} + \Sigma^+ + \Sigma^- = 0, \tag{2.30}$$

respectively. The Dirac $\delta(\boldsymbol{r})$ function expresses the locality of the forces applied by pointlike proteins on the fluid. The presence of proteins affects neither the dynamics of the solvent which is still given by the Stokes equations Eqs. (2.22) and (2.23), nor the no-slip fluid-fluid boundary conditions (Eqs.(2.27) and (2.28)). Finally, we assume again no-slip conditions between the lipid fluid and the embedded proteins:

$$\dot{\boldsymbol{r}}_n = \boldsymbol{v}(\boldsymbol{r}_n). \tag{2.31}$$

This equation yields the dynamics of proteins.

We now aim at expressing the dynamics of the systems with the relevant variables, *i.e.*, the membrane and proteins variables. We first introduce the continuous Fourier transform using the convention

$$\hat{f}(\boldsymbol{q}) = \int \mathrm{d}^2 r \, f(\boldsymbol{r}) \, \mathrm{e}^{-i\boldsymbol{q}\cdot\boldsymbol{r}}, \tag{2.32}$$

$$f(\boldsymbol{r}) = \int \frac{\mathrm{d}^2 q}{(2\pi)^2} f(\boldsymbol{q}) \mathrm{e}^{i\boldsymbol{q}\cdot\boldsymbol{r}}, \tag{2.33}$$

with $\boldsymbol{q}$ the 2D in-plane wavevector in Fourier space. Since the dynamics of the proteins is divided into the in-plane one and the transverse one, we use the Fourier Transform for the tangential (x, y) plane while keeping the transverse component along z in the direct space. Therefore, the bulk pressures $P^{\pm}(\boldsymbol{r}, z)$ and velocities $V^{\pm}(\boldsymbol{r}, z)$ become $P^{\pm}(\boldsymbol{q}, z)$ and $V^{\pm}(\boldsymbol{q}, z)$, respectively, the membrane height fields becomes $h(\boldsymbol{q})$ and so on. For vectorial quantities, we now use the local basis $(\hat{\boldsymbol{q}}, \hat{\boldsymbol{q}}_\perp, \boldsymbol{e}_z)$ with $\hat{\boldsymbol{q}} = \boldsymbol{q}/q$ and $\hat{\boldsymbol{q}}_\perp = \boldsymbol{e}_z \times \hat{\boldsymbol{q}}$. For instance, in this basis $V^{\pm} = V^{\pm}_{\parallel} \hat{\boldsymbol{q}} + V^{\pm}_{\perp} \hat{\boldsymbol{q}}_\perp + V^{\pm}_z \boldsymbol{e}_z$. In Fourier space, the bulk Stokes equations (2.22) and (2.23) become

$$\eta(\partial_z^2 - q^2) V^{\pm}_{\parallel} = iq P^{\pm}, \tag{2.34}$$

$$\eta(\partial_z^2 - q^2) V^{\pm}_{\perp} = 0, \tag{2.35}$$

$$\eta(\partial_z^2 - q^2) V^{\pm}_z = \partial_z P^{\pm}, \tag{2.36}$$

$$\partial_z V^{\pm}_z + iq V^{\pm}_{\parallel} = 0. \tag{2.37}$$

Using Eq. (2.34) to eliminate $P^{\pm}$ in Eq. (2.36), and then using Eq. (2.37) to further eliminate $V^{\pm}_{\parallel}$ yields $(\partial_z^2 - q^2) V^{\pm}_z = 0$. The solutions of the latter equations which vanish

at infinity are

$$V_z^{\pm} = (A^{\pm} + B^{\pm} z)\mathrm{e}^{\mp qz}, \tag{2.38}$$

with $A^{\pm}$, $B^{\pm}$ and $C^{\pm}$ depend on q and are given below. Substituting these solutions both into Eq. (2.36) and integrating with respect to z yields

$$P^{\pm} = 2\eta B^{\pm}\mathrm{e}^{\mp qz}, \tag{2.39}$$

and into Eq. (2.37) gives

$$V_{\parallel}^{\pm} = -i\left(\frac{B^{\pm}}{q} \mp A^{\pm} \mp B^{\pm} z\right)\mathrm{e}^{\mp qz}. \tag{2.40}$$

$V_{\perp}^{\pm}$ can be determined using Eq. (2.35):

$$V_{\perp}^{\pm} = C^{\pm}\mathrm{e}^{\mp qz}. \tag{2.41}$$

Finally, satisfying the boundary conditions between the bulk and the membrane fluids, we get

$$A^{\pm} = \dot{h}, \tag{2.42}$$
$$B^{\pm} = -iqv_{\parallel} \pm q\dot{h}, \tag{2.43}$$
$$C^{\pm} = v_{\perp}. \tag{2.44}$$

Thus, by injecting the expressions of the bulk variables into the tangential and transversal viscous stresses, the dynamical equations of the membrane and proteins become

$$(2\eta q + \eta_2 q^2)v_{\perp}(\boldsymbol{q}) + \sum_n \frac{\partial \mathcal{H}}{\partial \boldsymbol{r}_n} \cdot \hat{\boldsymbol{q}}_{\perp}\mathrm{e}^{-i\boldsymbol{q}\cdot\boldsymbol{r}_n} = 0, \tag{2.45}$$
$$v_{\parallel}(\boldsymbol{q}) = 0, \tag{2.46}$$
$$4\eta q\dot{h}(\boldsymbol{q}) = -\frac{\delta \mathcal{H}}{\delta h}(\boldsymbol{q}), \tag{2.47}$$
$$\dot{\boldsymbol{r}}_n = \boldsymbol{v}(\boldsymbol{r}_n), \tag{2.48}$$

with $\boldsymbol{v} = v_{\parallel}\hat{\boldsymbol{q}} + v_{\perp}\hat{\boldsymbol{q}}_{\perp}$. The two first equations come from the in-plane dynamics. The component $v_{\parallel}$ vanishes as the fluid is incompressible (Eq. (2.25)). Therefore, combining these two equations yields

$$\boldsymbol{v}(\boldsymbol{q}) = -\boldsymbol{O}(\boldsymbol{q}) \cdot \sum_n \frac{\partial \mathcal{H}}{\partial \boldsymbol{r}_n}\mathrm{e}^{-i\boldsymbol{q}\cdot\boldsymbol{r}_n}, \tag{2.49}$$

where one recognizes $\boldsymbol{O}$, the well-known mobility Oseen-like tensor [73, 74]

$$\boldsymbol{O}(\boldsymbol{q}) = \frac{\mathbb{1} - \hat{\boldsymbol{q}} \otimes \hat{\boldsymbol{q}}}{2\eta q + \eta_2 q^2}. \tag{2.50}$$

a. Mobility tensor

The mobility μ links the velocity $\boldsymbol{v}$ of an object to the force $\boldsymbol{f}$ applied to it, *i.e.*, the mobility is the velocity response of a considered protein to a force it feels [75], $\boldsymbol{v} = \mu \boldsymbol{f}$. For instance, according to Stokes law, the mobility of a spherical particle of radius a in a 3D fluid of viscosity η is given by $\mu_{3D} = 1/(6\pi\eta a)$ [76]. However, in 2D, the mobility diverges which is known as the Stokes paradox [76]. This has to do with the Oseen tensor.

The Oseen mobility tensor is the solution of the Stokeslet equation, *i.e.*, the Stokes equation where the object is reduced to a point on which a unit external force is applied. In other words, the Oseen mobility tensor is the Green function associated with the Stokes equation. In 2D, this tensor has an infrared divergence when integrated over wavevectors. This divergence can be regularized in two ways: either by restricting the 2D fluid to a finite area or by embedding the infinite 2D fluid in an immiscible 3D fluid [70, 77]. Fortunately, the last case occurs naturally for biological membranes, recalling that they are bidimensional fluids of lipids embedded in bulk water. Taking into account the solvent introduces a length cutoff, the so-called Saffman-Delbrück length $\ell = \eta_2/(2\eta)$ [70] that regularizes the infrared divergence. For the Oseen tensor given in Eq. (2.50), the regularization has led to the addition of the q term in the denominator.

In direct space, the Oseen tensor Eq. (2.50) becomes [78, 79]

$$O_{ij}(\boldsymbol{r}) = \frac{1}{4\eta_2}\left\{\left[H_0(r/\ell) - \frac{H_1(r/\ell)}{r/\ell} - \frac{1}{2}[Y_0(r/\ell) - Y_2(r/\ell)] + \frac{2}{\pi(r/\ell)^2}\right]\delta_{ij}\right. \tag{2.51}$$

$$\left. - \left[H_0(r/\ell) - \frac{2H_1(r/\ell)}{r/\ell} + Y_2(r/\ell) + \frac{4}{\pi(r/\ell)^2}\right]\frac{r_i r_j}{r^2}\right\}, \tag{2.52}$$

where Y_n and H_n are Bessel functions of the second kind and Struve functions, respectively. At short distances, *i.e.*, distances such that $r \ll \ell$, the Oseen tensor can be approximated to first order in r/ℓ by [79]

$$O_{ij}(\boldsymbol{r}) \simeq \frac{1}{4\pi\eta_2}\left\{-\left[\ln\left(\frac{r}{2\ell}\right) + \gamma + \frac{1}{2}\right]\delta_{ij} + \frac{r_i r_j}{r^2}\right\}, \tag{2.53}$$

with $\gamma \simeq 0.577$ Euler's constant. Therefore, at short distances, the Oseen tensor has a logarithmic decay which is typical of 2D flows. At large distances, $\boldsymbol{O}$ exhibits a $(\eta r)^{-1}$ decay, characteristic of 3D flows. Thus, to keep a bidimensional fluid, we should stay in the short distances regime. Especially, when considering hydrodynamic interactions between proteins, the interprotein distances should be negligible with respect to the Saffman-Delbrück length.

Nevertheless, the short distances Oseen tensor Eq. (2.53) does not allow for the recovery of the self-mobility corresponding to $\boldsymbol{r} = \boldsymbol{0}$. The self-mobility can be recovered by considering the flow provoked by a cylindrical protein of radius a_p dragged by an external force in a 2D planar fluid which gives back the well-known Saffman-Delbrück mobility [77]. Therefore, one gets

$$\boldsymbol{O}(\boldsymbol{r} = \boldsymbol{0}) = \mu_{\mathrm{SD}}\mathbb{1} = \frac{1}{4\pi\eta_2}\left[\ln\left(\frac{\ell}{a_p}\right)\right]\mathbb{1}. \tag{2.54}$$

Further details about self-mobility will be given in Sec. 4.2.

It is worth noting that, from a physics point of view, the true mobility tensor is positive definite, as this latter property is directly related to the second law of thermodynamics [80]. The Oseen tensor gives a valid approximation of the true mobility tensor for objects far from each other. However, when its use is extended to shorter distances it is not surprising that it is not positive-definite. For instance, depending on the strength of the hydrodynamic interaction, the mobility of a rigid rodlike polymer in a 3D fluid can be negative, which is unphysical [81]. In addition, since the positive-definiteness property is required for Brownian dynamics simulations [82, 83], one needs a corrected mobility tensor

In 3D, Rotne and Prager, in their seminal article [84], introduced a "patch" correcting the lack of positive-definiteness of the Oseen tensor at short distances, making it an acceptable mobility down to short distances. By applying a variational principle on the energy dissipation associated with an ansatz on the superposition of independent individual contribution of the particles to the stresses and restoring the particle size they get a correction to second order in a_p/r [84, 85]. Although the corrected tensor derived in this way can be inaccurate for small distances, it gives back the definite positiveness of the mobility tensor and tends to the usual Oseen tensor for large distances.

The same method was applied recently by Sokolov and Diamant on the 2D case [80]. Like in the 3D case, they get a correction to second order in a_p/r, so that the corrected Oseen tensor $\tilde{O}_{ij}$ is given by

$$\tilde{O}_{ij}(\boldsymbol{r}) = O_{ij}(\boldsymbol{r}) + \frac{1}{4\pi\eta_2}\left(\delta_{ij} - 2\frac{r_i r_j}{r^2}\right)\left(\frac{a_p}{r}\right)^2, \tag{2.55}$$

with $O_{ij}(\boldsymbol{r})$ given in Eq. (2.53). This corrected tensor is valid for $\boldsymbol{r} = \boldsymbol{0}$ and $\tilde{\boldsymbol{O}}(\boldsymbol{r} = \boldsymbol{0})$ coincides with $\boldsymbol{O}(\boldsymbol{r} = \boldsymbol{0})$. A step-by-step presentation of the computations performed by Sokolov and Diamant to get the corrected tensor is given in Appx. A. In addition, along with the corrected Oseen tensor introduced above, the authors of [80] derived another positive-definite mobility tensor for objects allowed to overlap, that fails at very short distances. Thereby, we derive a rectified mobility tensor in the overlapping case, using the method of [85] (see Appx. A).

In the following, we shall replace the Oseen tensor $\boldsymbol{O}(\boldsymbol{r})$ with its corrected counterpart.

b. Dynamics of the proteins

We now go back to the dynamical equations. Using the membrane-proteins continuity equation Eq. (2.48) and the 2D fluid velocity expression Eq. (2.49) we get the dynamics of proteins

$$\dot{\boldsymbol{r}}_n = -\sum_m \int \frac{\mathrm{d}^2 q}{(2\pi)^2}\, \tilde{\boldsymbol{O}}(\boldsymbol{q}) \cdot \frac{\partial H}{\partial \boldsymbol{r}_m}\, \mathrm{e}^{i\boldsymbol{q}\cdot(\boldsymbol{r}_n - \boldsymbol{r}_m)} = -\sum_m \tilde{\boldsymbol{O}}(\boldsymbol{r}_n - \boldsymbol{r}_m) \cdot \frac{\partial H}{\partial \boldsymbol{r}_m}, \tag{2.56}$$

where the second equality arises from the definition of the inverse Fourier transform of the corrected Oseen tensor.

Up to now, we did not take into account the thermal fluctuations that affect both the membrane and the proteins. To do so, we add thermal noises to the latter that satisfy the detailed balance condition, *i.e.*, the added noises ensure thermal equilibrium. Therefore, as the 2D fluid is viscous, we use overdamped Langevin equations to describe the dynamics:

$$\dot{h} = -\frac{1}{4\eta q}\frac{\delta \mathcal{H}}{\delta h} + \nu(\boldsymbol{q}, t), \tag{2.57}$$

$$\dot{\boldsymbol{r}}_n = -\sum_m \tilde{O}(\boldsymbol{r}_n - \boldsymbol{r}_m) \cdot \frac{\partial \mathcal{H}}{\partial \boldsymbol{r}_m} + \boldsymbol{\xi}_n(t), \tag{2.58}$$

where $\Lambda_q = (4\eta q)^{-1}$ is the Fourier transform of the Oseen hydrodynamic kernel. The quantities ν and $\boldsymbol{\xi}_n$ are Gaussian white noises with zero mean such that ($k_\mathrm{B} = 1$)

$$\langle \nu(\boldsymbol{q}, t)\nu(\boldsymbol{q}', t')\rangle = \frac{T}{2\eta q}(2\pi)^2 \delta(\boldsymbol{q} + \boldsymbol{q}')\delta(t - t'), \tag{2.59}$$

$$\langle \boldsymbol{\xi}_n(t)\boldsymbol{\xi}_m(t')\rangle = 2T\tilde{\boldsymbol{O}}(\boldsymbol{r}_n - \boldsymbol{r}_m)\delta(t - t'), \tag{2.60}$$

$$\langle \nu \boldsymbol{\xi}_n \rangle = \boldsymbol{0}. \tag{2.61}$$

The forces in real space are given by

$$\frac{\delta \mathcal{H}}{\delta h}(\boldsymbol{r}) = \kappa \nabla^4 h(\boldsymbol{r}) - \sigma \nabla^2 h(\boldsymbol{r}) + \kappa_p \sum_n \partial_i \partial_j \left[K_{ij}^{(n)}(\boldsymbol{r}) \delta(\boldsymbol{r} - \boldsymbol{r}_n) \right], \tag{2.62}$$

$$\frac{\partial \mathcal{H}}{\partial \boldsymbol{r}_m} = \kappa_p \int \mathrm{d}^2 r \, \delta(\boldsymbol{r} - \boldsymbol{r}_m) \, K_{ij}^{(m)}(\boldsymbol{r}) \, \boldsymbol{\nabla} \partial_i \partial_j h(\boldsymbol{r}). \tag{2.63}$$

Note that while the dynamical equations given above ensure convergence towards thermal equilibrium, we can drive them out of equilibrium by introducing sources of noise that break the detailed balance condition (see Sec. 3.2.3).

2.3 Conclusion

Considering the bending elasticity of the membrane we modeled the couplings between pointlike proteins and a membrane. Then, regarding the membrane as a bi-dimensional incompressible viscous fluid containing proteins gave coupled overdamped Langevin equations for the dynamics of the system.

We will use our modeling to study both the collective behavior of curvature-inducing proteins that bind and unbind to the membrane in Chapter 3 and the mediated interactions between proteins that can change their conformation in Chapter 5.

Finally, in Chapter 4, we will take advantage of the simplicity of our pointlike approach to study the mobility of a protein in a membrane considering various cases.

Chapter 3

Binding of thermalized and active membrane curvature-inducing proteins

In this chapter, we focus on proteins that induce a local curvature of the membrane when they bind to it. We consider a membrane in contact with a reservoir of such proteins that can bind or unbind. We analyze the phase behavior of this system by a combination of analytical and numerical approaches. In thermal equilibrium under the detailed balance between binding and unbinding, the membrane exhibits three phases: an unbound uniform flat phase (U), a bound uniform flat phase (B), and a separated/corrugated phase (SC). In the SC phase, the bound proteins form hexagonally-ordered bowl-shaped domains. The transitions between the U and SC phases and between the B and SC phases are second order and first order, respectively. At small spontaneous curvature of the protein or high surface tension, the transition between the B and SC phases becomes continuous. Moreover, a first-order transition between the U and B phases is found at zero spontaneous curvature driven by the Casimir-like interactions between rigid proteins. Furthermore, nonequilibrium dynamics is investigated by the addition of active binding and unbinding at a constant rate. The active binding and unbinding processes alter the stability of the SC phase. This work was performed and published [86] in collaboration with Prof. Hiroshi Noguchi who performed all the Monte Carlo simulations.

3.1 Introduction

Previously, we introduced examples of proteins that bind to biological membranes and locally reshape the curvature. For instance the F-BAR proteins of the BAR superfamily that bind to membranes via their BAR domain play a role in various biological mechanisms such that the clathrin-mediated endocytosis via the generation of membrane tubules [20, 30]. Clathrins are triskelion-shaped proteins that form a polyhedral lattice (*i.e.*, a coat") when they interact with each other. When they are recruited by the

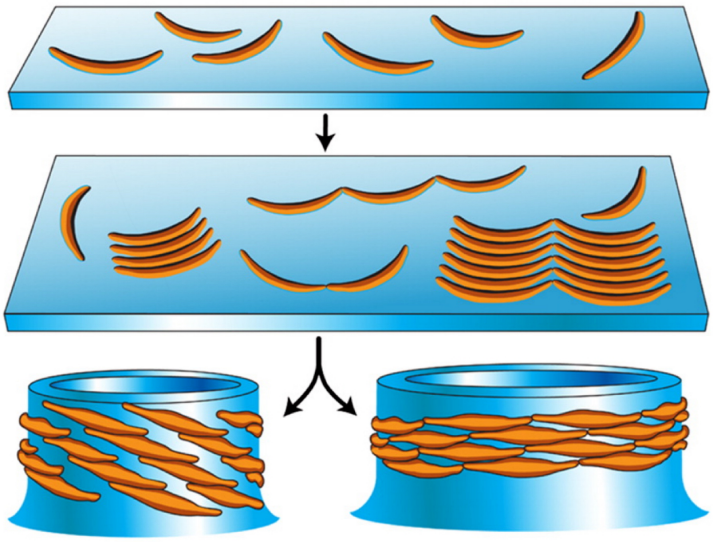

Figure 3.1 – Schematic representation of the steps of membrane tubulation induced by F-BAR proteins. Some F-BAR proteins (orange) bind to the membrane (blue plate) that remains flat as the concentration of proteins is low. Then, enticed by the local membrane curvature generated by the already attached F-BARs, more proteins bind to the membrane beginning the tubulation. Finally, at a high enough concentration, tubules are formed by the assembly of F-BAR proteins. Two distinct size tubules are shown according to the way these proteins scaffold. *Extracted from [87].*

biological membrane, these coat-proteins begin to form buds by locally imposing their spontaneous curvature of the membrane parts they cover. Attracted by the buds, some F-BAR proteins bind to the membrane along their BAR domain and begin to generate a curvature. F-BAR proteins are not only curvature generators but also curvature sensors that preferentially attach to areas where the membrane curvature matches its spontaneous curvature. Therefore, these proteins aggregate by scaffolding, forming a collective assembly and thus generating membrane tubulation [87] (see Fig. 3.1).

The tube thus formed is the only link between the membrane bud shaped by the clathrin and the rest of the bilayer membrane. In order to achieve the vesicle formation, the tube must be "dissolved". It happens when the dynamin proteins, recruited by the F-BAR proteins during the tubulation, change guanosine triphosphate (GTP) enzymes into guanosine diphosphate (GDP) by hydrolysis (GTPase), leading to the unbinding of the F-BAR proteins [88, 89]

Therefore, we see two underlying phenomena behind this mechanism: collective behavior and non-equilibrium processes. In living cells, biomembranes evolve in non-equilibrium conditions, and the individual protein binding/unbinding is often activated by chemical reactions. Thus the fluctuations of membranes containing such active proteins are often found to deviate from the equilibrium spectrum [90, 91]. In terms of collective behavior, spatiotemporal patterns in membranes are often observed in cell migration, spreading, growth, or division [92–96]

The binding of proteins and their assembly on membranes have been explored in equilibrium for fully flat membranes [97–99] and in the more complicated case of curved membranes where the effects of a fixed curvature sensing [100–102] are present. But the

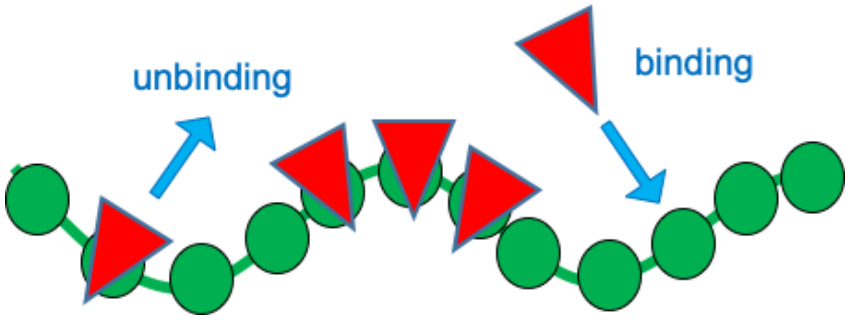

Figure 3.2 – Binding and unbinding of molecules with a finite spontaneous curvature of the membrane.

phase diagram of a membrane that can freely curve in equilibrium and to which curvature-inducing proteins can bind and interact via curvature-mediated interactions [19, 55, 103–105] deserves to be thoroughly investigated. As seen in the case of clathrin endocytosis, active chemical reactions play a role in the behavior of the protein, it is therefore important to determine how the related nonequilibrium collective behavior affects the phase diagram of the membrane/proteins system and modifies the membrane shapes and domain structures. In this chapter, we thus examine the binding/unbinding of proteins or other macromolecules onto a deformable membrane, whether in or out of thermal equilibrium, using theory and simulations.

In Section 3.2, the theoretical analysis of the protein binding/unbinding is presented. It leads to a phase diagram, in or out of equilibrium, for the membrane phases in terms of c_0 and of the chemical potential. In Section 3.3, the simulation model and method are described. In Sections a. and b., the simulation results of the thermal binding/unbinding process without and with active unbinding are presented, respectively. Comparison with the theoretical analysis shows good agreement. An outlook is presented in Section 3.5.

3.2 Theory

We assume that the binding of the molecule locally changes the bending rigidity and induces a spontaneous curvature c_0 of the membrane, as shown in Fig. 3.2. This spontaneous curvature is assumed to be isotropic, *i.e.*, the bound membrane has no preferred bending orientation.

We consider an incompressible membrane of fixed surface area A, which contains a surface density $\rho(\boldsymbol{x})$ of bound proteins that are exchanged with a reservoir of chemical potential μ. The membrane is assumed to be subjected to an external lateral frame tension γ conjugate to the projected area $A_p = L_p^2$ (area of the membrane average plane); for the sake of simplicity, the corresponding contribution will be introduced at a later stage. We assume an ideal mixture of protein-coated membrane and protein-free membrane so that the free energy of the system takes the form [102].

$$\mathcal{F} = \int_A dS \left\{ \left(1-\rho a^2\right) \left[\frac{\kappa_u}{2} \left(c_1+c_2\right)^2 + \bar{\kappa}_u c_1 c_2 \right] \right.$$
$$+ \rho a^2 \left[\frac{\kappa_b}{2} \left(c_1+c_2-c_0\right)^2 + \bar{\kappa}_b c_1 c_2 \right] - \mu\rho$$
$$\left. + T \left[\rho \ln(\rho a^2) + \left(a^{-2}-\rho\right) \ln\left(1-\rho a^2\right) \right] \right\}. \tag{3.1}$$

The first term, proportional to $1-\rho a^2$, where a^2 is the surface area covered by a bound protein, is the standard Canham-Helfrich Hamiltonian – presented in the previous chapter, Eq. (2.2) – describing the curvature energy of the unbound membrane fraction [57], with a bending rigidity κ_u and a Gaussian modulus $\bar{\kappa}_u$. Like $\rho(\boldsymbol{x})$, the membrane principal curvatures $c_1(\boldsymbol{x})$ and $c_2(\boldsymbol{x})$ are space-dependent. We shall assume that the saddle-splay modulus $\bar{\kappa}_u = -\kappa_u$, as this value satisfies the stability condition of the protein-free membrane [58] on the one hand and it will match the numerical simulations on the other.

The second term, proportional to ρ, is the standard Helfrich Hamiltonian (Eq. (2.1)) for the bound membrane fraction, with a spontaneous curvature c_0. We shall also choose $\bar{\kappa}_b = -\kappa_b$. In this case, the term in brackets reduces to $\frac{1}{2}\kappa_b(c_1-c_0)^2 + \frac{1}{2}\kappa_b(c_2-c_0)^2$ up to a constant that we may discard as it simply renormalizes the chemical potential μ. The proteins thus locally promote an isotropic curvature of magnitude c_0, as conically-shaped inclusions would do. Although curvature-inducing proteins presumably stiffen the bound membrane (otherwise they would fail to impose a local prescribed curvature), their bending strength is protein-dependent. For the sake of simplicity, we shall assume $\kappa_b \sim 10\kappa_u$ in this study.

The third term describes the equilibrium exchange of the proteins with the solvent, i.e., the binding/unbinding process, through a chemical potential μ. Note that the binding energy has been absorbed in the definition of the chemical potential [102]. The last term, with T the temperature in energy units, describes the entropy of mixing of proteins [102, 106].

For small deformations relative to the flat state, the shape of the membrane can be described in the Monge gauge by the height function $z = h(\boldsymbol{r})$, where $\boldsymbol{r}$ covers a two-dimensional (2D) plane. We recall that to second order in the deformation h, we have $c_1^2+c_2^2 \simeq (\partial_i\partial_j h)^2$, $(c_1-c_0)^2+(c_2-c_0)^2 \simeq (\partial_i\partial_j h - c_0\delta_{ij})^2$ and $dS \simeq [1+\frac{1}{2}(\boldsymbol{\nabla}h)^2]d^2r$, where we used Einstein's summation convention, which will be implicit throughout. Thus, to second order, the free energy becomes $\mathcal{F} \simeq \tilde{\mathcal{F}}$, with

$$\tilde{\mathcal{F}} = \int_{A_p} d^2r \left\{ \frac{(1-\rho a^2)\kappa_u + \rho a^2 \kappa_b}{2} (\partial_i\partial_j h)^2 - \rho a^2 \kappa_b c_0 \boldsymbol{\nabla}^2 h \right.$$
$$+ \left(1+\frac{1}{2}(\boldsymbol{\nabla}h)^2\right) \left[\rho a^2 \kappa_b c_0^2 + T\rho \ln(\rho a^2) \right.$$
$$\left. \left. + T\left(a^{-2}-\rho\right) \ln\left(1-\rho a^2\right) - \mu\rho \right] \right\}, \tag{3.2}$$

where A_p is the projected area of the membrane. Note that $0 < \rho a^2 < 1$ is not assumed to be small.

In this section, we will now work in dimensionless units by setting $a = T = 1$. In other words, we take T as the unit of energy and a as the unit of length. In addition, since we are interested in a system with a large projected membrane area A_p (and in accordance with the numerical simulations below), we will assume periodic boundary conditions.

3.2.1 Linear stability analysis in equilibrium

Due to the curvature promoted by the bound proteins, we expect the flat membrane to develop spatial undulations. The only term that may destabilize the flat membrane, however, is the second term of Eq. (3.2); but if ρ is uniform, it is a boundary term with no effect under periodic boundary conditions. In other words, the energy gain in the favorably curved parts would be compensated by the energy loss in the unfavorably curved parts.

We thus expect that at both low and high protein densities, the membrane will remain flat since the entropy of mixing will promote uniform density. At intermediate densities, however, lateral phase separation accompanied by spatial modulations of the membrane will be possible.

Therefore, we foresee three phases: an unbound uniform flat phase (U), i.e., a flat membrane with a low density of bound proteins, a bound uniform flat phase (B), i.e., a flat membrane with a high density of bound proteins, and a separated/corrugated phase (SC), i.e., a corrugated membrane with regions of different protein densities and curvatures. Since the U and B phases have the same symmetries, we expect either a first-order transition between them, a transition through an intermediate phase, or a continuous transformation similar to the gas–liquid transformation above the critical point.

Let us first examine the situation where the membrane is flat. For $h = 0$, the energy $\tilde{\mathcal{F}}$ becomes

$$\tilde{\mathcal{F}}_0 = L_0^2 \left[\rho \kappa_b c_0^2 + \rho \ln \rho + (1-\rho) \ln(1-\rho) - \mu \rho \right], \tag{3.3}$$

where $L_0^2 = A$ is the membrane area. Minimizing it with respect to ρ gives the equilibrium density [102]

$$\rho_0 = \frac{1}{1 + \mathrm{e}^{\kappa_b c_0^2 - \mu}}, \tag{3.4}$$

for which $\tilde{\mathcal{F}}_0 = L_0^2 \ln(1-\rho_0)$.

We now perform a linear stability analysis of this solution for a square membrane under a fixed external lateral tension γ at fixed total area L_0^2. Let us consider a small perturbation $h = h_1(\boldsymbol{r})$ and $\rho = \rho_0 + \rho_1(\boldsymbol{r})$ of the previous solution. Calling $L_p = L_0 + L_1$ the linear size of the perturbed membrane, the area constraint reads $L_p^2 + \int_0^{L_p} d^2 r \frac{1}{2} (\boldsymbol{\nabla} h)^2 =$

L_0^2, yielding to second order in the perturbation

$$L_1 \simeq -\frac{1}{2L_0}\int_0^{L_0} \mathrm{d}^2 r\, \frac{1}{2}(\boldsymbol{\nabla} h_1)^2. \tag{3.5}$$

Taking into account that $\kappa_b c_0^2 - \mu = \ln[(1-\rho_0)/\rho_0]$, the energy becomes at second order in the perturbation

$$\begin{aligned}\tilde{\mathcal{F}} \simeq \int_0^{L_p} d^2 r \Big[&\frac{\kappa_{\mathrm{eff}}}{2}(\boldsymbol{\nabla}^2 h_1)^2 - \rho_1 \kappa_b c_0 \boldsymbol{\nabla}^2 h_1 \\ &+ \left(1 + \frac{1}{2}(\boldsymbol{\nabla} h_1)^2\right)\ln(1-\rho_0) + \frac{\rho_1^2}{2\rho_0(1-\rho_0)}\Big],\end{aligned} \tag{3.6}$$

where $\kappa_{\mathrm{eff}} = (1-\rho_0)\kappa_u + \rho_0\kappa_b$. Note that we have discarded a term $\propto \boldsymbol{\nabla}^2 h_1$ that vanishes under periodic boundary conditions, and replaced $(\partial_i \partial_j h)^2$ by $(\boldsymbol{\nabla}^2 h)^2$, since the difference vanishes under periodic boundary conditions. Now, to second order in the perturbation, we have

$$\int_0^{L_p} d^2 r \ln(1-\rho_0) \simeq (L_0^2 + 2L_0 L_1)\ln(1-\rho_0), \tag{3.7}$$

therefore this term gives $\tilde{\mathcal{F}}_0 = L_0^2 \ln(1-\rho_0)$ plus a contribution that cancels the term proportional to $(\boldsymbol{\nabla} h_1)^2$ in Eq. (3.6), because of Eq. (3.5). Adding the energy associated with the external tension, the total energy becomes $\mathcal{F}^\star = \tilde{\mathcal{F}} - \gamma L_p^2$, which reads, up to a constant and at second order in the perturbation,

$$\begin{aligned}\mathcal{F}^\star \simeq \int_0^{L_0} d^2 r \Big[&\frac{\kappa_{\mathrm{eff}}}{2}(\boldsymbol{\nabla}^2 h_1)^2 - \rho_1 \kappa_b c_0 \boldsymbol{\nabla}^2 h_1 \\ &+ \frac{1}{2}\frac{\rho_1^2}{\rho_0(1-\rho_0)} + \frac{\gamma}{2}(\boldsymbol{\nabla} h_1)^2\Big].\end{aligned} \tag{3.8}$$

Calling $h_{1,\boldsymbol{q}}$ and $\rho_{1,\boldsymbol{q}}$ the Fourier transforms of the perturbation fields, we obtain

$$\mathcal{F}^\star \simeq \frac{1}{2} L_0^2 \sum_{\boldsymbol{q}} \begin{pmatrix} h_{1,\boldsymbol{q}} \\ \rho_{1,\boldsymbol{q}} \end{pmatrix}^t \mathsf{M}_{\mathrm{eq}} \begin{pmatrix} h_{1,-\boldsymbol{q}} \\ \rho_{1,-\boldsymbol{q}} \end{pmatrix}, \tag{3.9}$$

with

$$\mathsf{M}_{\mathrm{eq}} = \begin{pmatrix} \kappa_{\mathrm{eff}} q^4 + \gamma q^2 & \kappa_b c_0 q^2 \\ \kappa_b c_0 q^2 & \frac{1}{\rho_0(1-\rho_0)} \end{pmatrix}. \tag{3.10}$$

The flat membrane is unstable if M_{eq} has negative eigenvalues. Since $\mathrm{tr}(\mathsf{M}_{\mathrm{eq}}) > 0$, the corresponding condition is $\det(\mathsf{M}_{\mathrm{eq}}) < 0$, which reads

$$\left[\kappa_{\mathrm{eff}} - \kappa_b^2 c_0^2 \rho_0(1-\rho_0)\right] q^2 + \gamma < 0. \tag{3.11}$$

For tensionless membrane ($\gamma = 0$), all q modes are therefore destabilized when the quan-

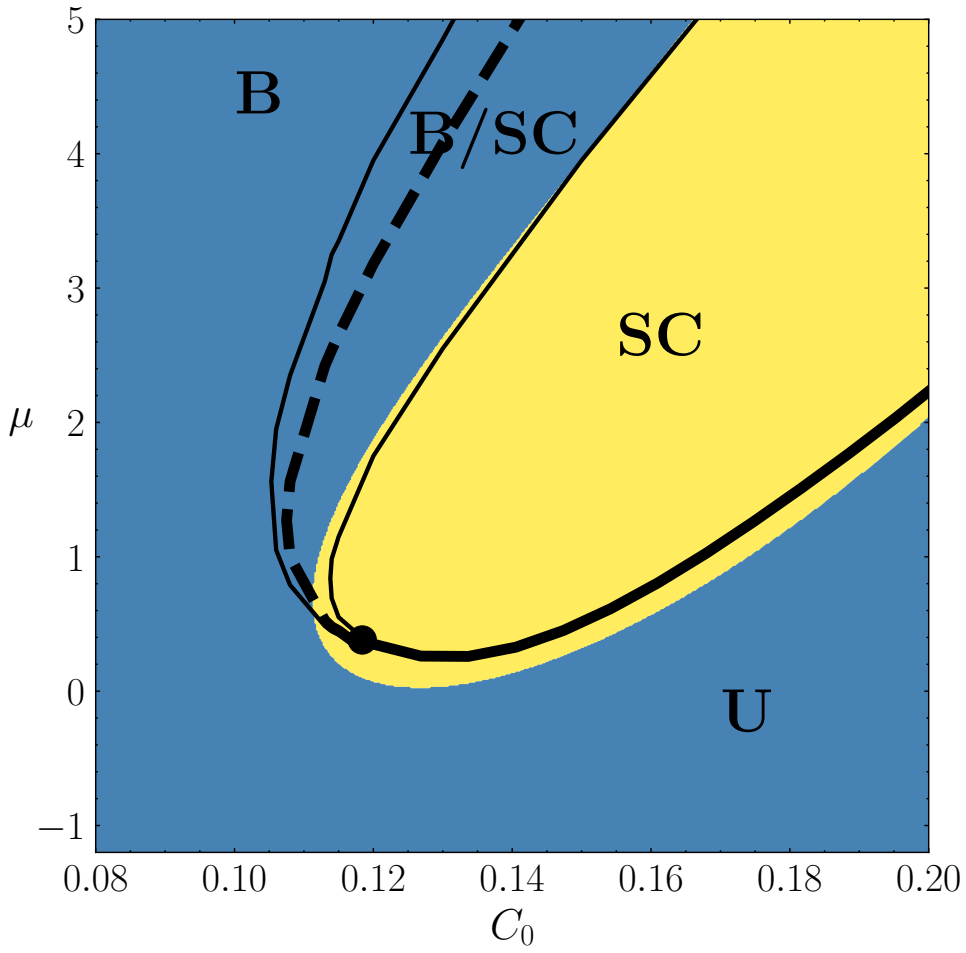

Figure 3.3 – Equilibrium phase diagram. In the blue region, the flat membrane is stable against small perturbations, while in the yellow region, it is unstable. The black lines show the phase diagram obtained from the bumpy 1D shapes studied in the nonlinear analysis. U: unbound flat phase (low protein density), B: bound flat phase (high protein density), SC: separated-corrugated phase where the membrane exhibits curved domains with a separation between protein-dense and protein-poor regions. The thick solid line indicates a second-order phase transition. The thick dashed line corresponds to a first-order phase transition, with a coexistence region delimited by the two thin solid lines. The black dot indicates a tricritical point. Parameters are $\kappa_u = 16$, $\kappa_b = 144$ and $\gamma = 0.5$.

tity $\delta = \kappa_{\text{eff}} - \kappa_b^2 c_0^2 \rho_0(1-\rho_0)$ in the square brackets above is negative. For $\gamma > 0$, the unstable modes are in the interval $q \in [q_{\min}, q_{\max}]$, with $q_{\max} = +\infty$ and $q_{\min} = \sqrt{\gamma/(-\delta)}$. Now, for membranes with proteins, our length scale a also corresponds to the smallest wavelength accessible to membrane fluctuations, which sets an upper cutoff $q_{\max}$ in Fourier space of order $1/a$, or, in dimensionless units, of order 1. Thus, if $q_{\min}$ is larger than 1 there is no physical range of q that can be excited by the instability, even if $\delta < 0$. Hence, we expect that when $\delta < -\gamma$ there will be a separated and modulated phase (SC) if the condition $\delta < 0$ is met. A necessary condition for $\delta < 0$ is given by $c_0 > C_{\text{th}}$, with

$$C_{\text{th}} = \frac{\sqrt{\kappa_u} + \sqrt{\kappa_b}}{\kappa_b}. \tag{3.12}$$

The instability condition $\delta < -\gamma$ is actually fulfilled in the range of μ shown in the yellow region of Fig. 3.3 whose borders is defined by the upper and lower expressions

$$\mu = c_0^2\kappa_b - \ln\left[\frac{-2\gamma - \kappa_u - \kappa_b + c_0^2\kappa_b^2 \mp \sqrt{-4(\gamma+\kappa_u)(\gamma+\kappa_b) + (2\gamma+\kappa_u+\kappa_b-c_0^2\kappa_b^2)^2}}{2(\gamma+\kappa_u)}\right] \tag{3.13}$$

This unstable region is slightly shrunk at smaller values of γ. As expected, spatial undulations occur when the membrane is neither too poor nor too rich in proteins, i.e., at intermediate values of μ where the entropy of the mixture allows phase separation, as evidenced by the presence of the $\rho_0(1-\rho_0)$ factor in the instability condition.

3.2.2 Nonlinear analysis in equilibrium

The linear stability analysis is of course unable to predict the corrugation pattern selected by the system in the nonlinear regime. Instead of solving the corresponding nonlinear PDEs (with the covariant Helfrich contribution to the energy) we follow an alternative route. We postulate that the system will adopt a corrugated phase, which we parametrize with a small number of parameters. To simplify, we assume in addition that the selected patterns are translationally invariant along one space direction.

To study the phase diagram of the system beyond the linear stability analysis, we thus consider a family of corrugated shapes of arbitrary amplitude (Fig. 3.4a). In the SC phase, we expect the system to develop periodic structures with large regions of curvature favorable to inclusions, surrounded by narrow regions of opposite curvature. Proteins will naturally accumulate in the favorable regions and deplete in the unfavorable regions. We thus consider the following three-parameter family of smooth shapes:

$$h(x) = R\theta\ \Gamma(x)\ \frac{\tanh\left(\frac{x+R}{\lambda}\right) - \tanh\left(\frac{x-R}{\lambda}\right)}{2\tanh\left(\frac{2R}{\lambda}\right)^2}, \tag{3.14}$$

with $\Gamma(x)$ the circular arc of equation $\sqrt{R^2 - x^2}$, which is replaced by its sixth order

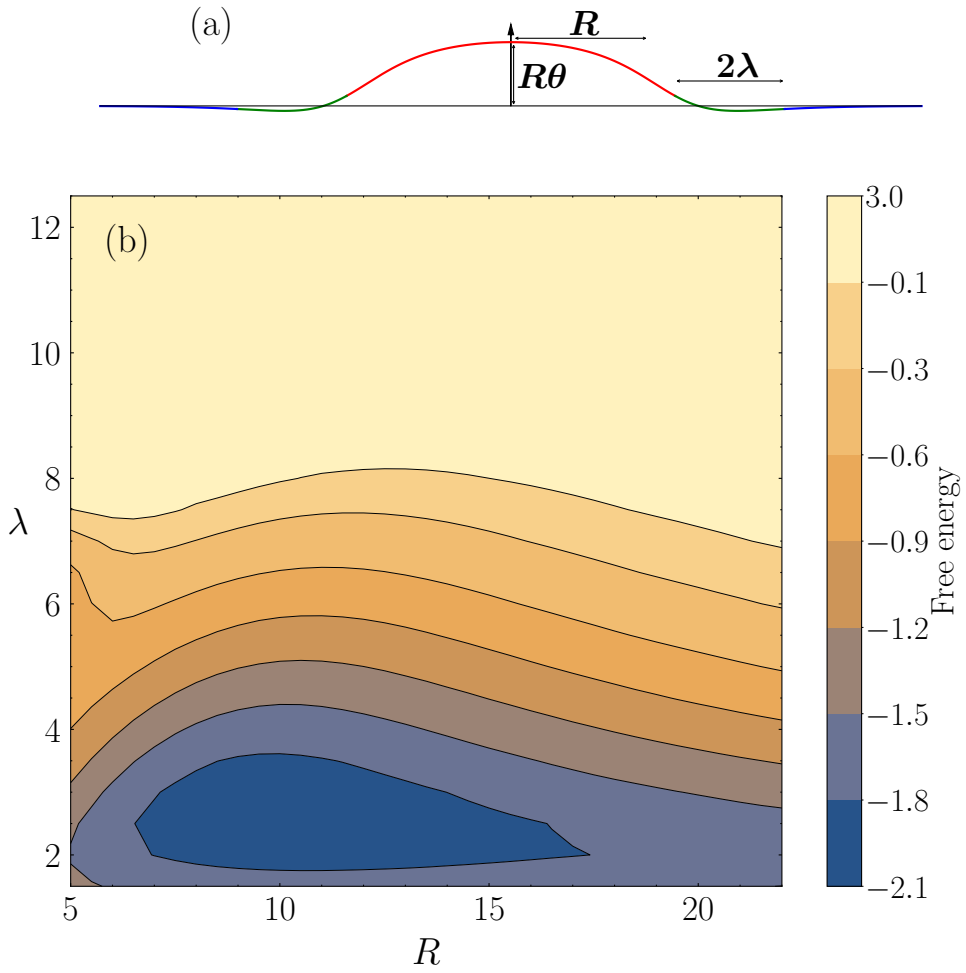

Figure 3.4 – (a) Typical membrane shape with a bump for use in the nonlinear analysis (cross-section). (b) Free energy f of the bump as a function of R and λ after numerical minimization with respect to θ. The blue regions of low energy correspond to $\lambda \ll R$. Parameters are $\kappa_u = 16$, $\kappa_b = 144$, $\gamma = 0.5$, $c_0 = 0.15$ and $\mu = 2$ (deep in the instability region).

Taylor expansion in order to allow $x > R$:

$$\Gamma(x) \simeq \left(R - \frac{x^2}{2R} - \frac{x^4}{8R^3} - \frac{x^6}{16R^5} \right). \tag{3.15}$$

The function (3.14), parametrized by (R, λ, θ), describes a membrane deformation having a central circular bump of width $2R$ and amplitude $R\theta$ surrounded by side channels of width 2λ in which the curvature changes sign and relaxes (Fig. 3.4a). This deformation can be repeated in space in order to produce a corrugation.

We then seek to determine the equilibrium state of the system. With $c_1 = c$ and $c_2 = 0$, the free energy (3.1) per unit length, supplemented by the contribution of the external tension, takes the exact nonlinear form:

$$\begin{aligned} f = \int_{-\frac{L_p}{2}}^{\frac{L_p}{2}} \sqrt{1+h'^2} \Big[(1-\rho)\frac{\kappa_u}{2} c^2 + \rho \frac{\kappa_b}{2}[(c-c_0)^2 + c_0^2] \\ + \rho \ln \rho + (1-\rho)\ln(1-\rho) - \mu\rho \Big] dx - \gamma L_p, \end{aligned} \tag{3.16}$$

with $c = h''/(1+h'^2)^{3/2}$, where $L = \int_{-L_p/2}^{L_p/2} dx \sqrt{1+h'^2}$, is the fixed total length perpendicular to the translational invariant direction and L_p is its variable projected length determined consistently. Constructed this way, f is a function of R, λ, θ and a functional of $\rho(x)$. Minimizing f with respect to $\rho(x)$ gives $\rho^\star(x) = [1+\exp(-\frac{1}{2}\kappa_u c(x)^2 + \frac{1}{2}\kappa_b[(c(x)-c_0)^2 + c_0^2] - \mu)]^{-1}$, and the free energy per unit length reduces to

$$f = \int_{-\frac{L_p}{2}}^{\frac{L_p}{2}} \sqrt{1+h'^2} \left[\frac{\kappa}{2} c^2 + \ln(1-\rho^\star) \right] dx - \gamma L_p. \tag{3.17}$$

Let us place ourselves in the region of instability of the linear stability analysis (Fig. 3.3), and numerically examine when the bumps described by $f(R, \lambda, \theta)$ are stable with respect to the flat state. It is worth mentioning that since we consider a particular family of deformations, the flat state can be found stable for a broader range of values of μ and c_0, *i.e.*, the instability region of the considered shapes is shrunk with respect to the yellow instability region found with the linear stability analysis. Scanning the (R,λ) plane and minimizing numerically the energy with respect to θ (Fig. 3.4b), we find that the stable bumps appear in a large R range but have a small, well-defined λ value. We therefore expect the SC phase to consist of large protein-filled bumps surrounded by narrow protein-depleted oppositely curved channels.

Since the system prefers narrow side channels, we set a small $\lambda \simeq 2.5$ (see Fig. 3.4) and we keep R and θ as parameters. We find that the one-dimensional bumps shapes, corresponding to the separated/corrugated (SC) phase, are stable with respect to the flat state within the region delimited by the thick solid and thick dashed lines in Fig. 3.3. Starting at small chemical potentials and increasing μ, the transition from the flat unbound phase (U) to the separated/corrugated phase (SC) is of second order to the right of a tricritical point and of first order to its left. Increasing μ, there is, as expected, a re-entrant first-order transition toward a flat state, the flat bound phase (B). The equi-

librium values of R and θ are shown in Fig. 3.5. Determining the equilibrium values of R and θ as function of μ for different values of c_0 allows us to determine the phase transitions represented by the black lines in Fig. 3.3

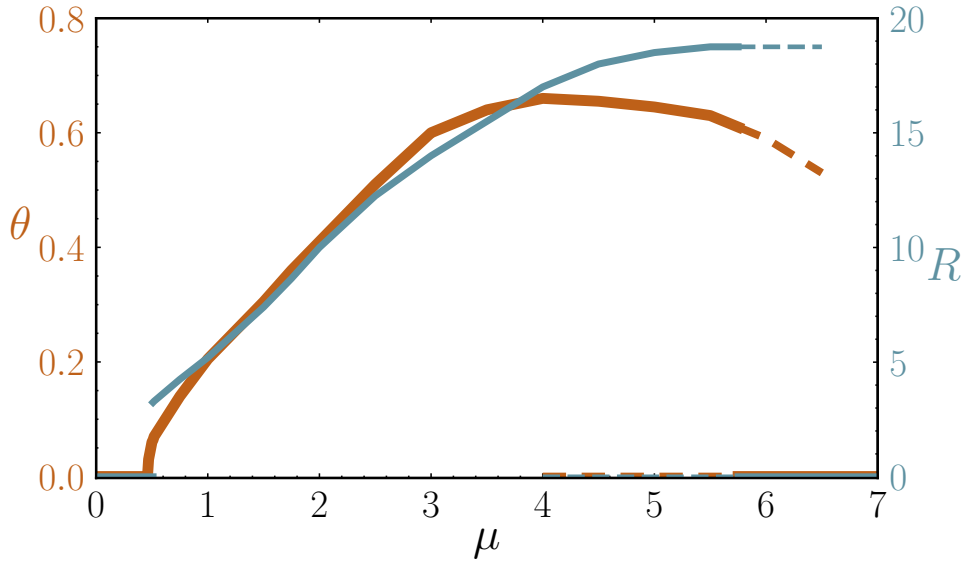

Figure 3.5 – Equilibrium amplitude θ (order-parameter) and width R of the 1D bumps used in the nonlinear analysis as a function of μ. The solid lines correspond to stable states and the dashed lines to metastable states. Parameters are the same as in Fig. 3.3 and $c_0 = 0.15$.

3.2.3 Linear stability analysis in the presence of active binding/unbinding

In nonequilibrium, it is necessary to specify the dynamics of the system to study its behavior. We model the binding-unbinding mechanism by a Poisson process with rates η_1 and η_2 :

$$\text{bound} \underset{\eta_1}{\overset{\eta_2}{\rightleftharpoons}} \text{unbound} \tag{3.18}$$

Neglecting the fluctuations caused by the binding/unbinding active processes and by the thermal exchanges with the thermostat, we consider the following noiseless dynamical equations for the density and height fields:

$$\begin{aligned}\dot{\rho}(\boldsymbol{r}) = \boldsymbol{\nabla}\cdot\left(m\rho(1-\rho a^2)\boldsymbol{\nabla}\frac{\delta\hat{\mathcal{F}}}{\delta\rho}\right) + \alpha_1(a^{-2}-\rho)\\ - \alpha_2\rho + \eta_1(a^{-2}-\rho) - \eta_2\rho,\end{aligned} \tag{3.19}$$

$$\dot{h}(\boldsymbol{r}) = -\Lambda\frac{\delta\hat{\mathcal{F}}}{\delta h}, \tag{3.20}$$

where $\hat{\mathcal{F}} = \tilde{\mathcal{F}} - \gamma L_p^2$. The first term in Eq. (3.19), proportional to the mobility m of the particles, stems from the conservation of their number in the absence of binding/unbinding processes. It is the divergence of the particle current, in which the

$\rho(1-\rho a^2)$ factor accounts for the vanishing of the current both for $\rho = 0$ (empty state) and $\rho = a^{-2}$ (filled state). Note that for small ρ this part of the equation reduces to the noiseless Dean-Kawasaki equation [107, 108]. The next two terms describe the equilibrium binding and unbinding of the proteins, respectively. Note that there is some freedom in choosing the thermal binding-unbinding rates, as long as the detailed balance condition is fulfilled i.e., $\alpha_1/\alpha_2 = e^{-\beta\Delta\mathcal{H}(\boldsymbol{r})}$. One possibility, which we adopt, is to resort to the Glauber rates defined by $\alpha_1 = \alpha e^{\beta\Delta\mathcal{H}(\boldsymbol{r})}/(1+e^{\beta\Delta\mathcal{H}(\boldsymbol{r})})$ and $\alpha_2 = \alpha e^{-\beta\Delta\mathcal{H}(\boldsymbol{r})}/(1+e^{-\beta\Delta\mathcal{H}(\boldsymbol{r})})$ where $\Delta\mathcal{H}(\boldsymbol{r}) = \frac{1}{2}\kappa_b(\partial_i\partial_j h - c_0\delta_{ij})^2 - \frac{1}{2}\kappa_u(\partial_i\partial_j h)^2 - \mu$ is the energy variation upon binding of a protein. While also being associated to local configuration changes, they further share with the Metropolis rates used in the simulations (that we will present in Section 3.3) the property that they remain bounded, regardless of the energy change involved. Other choices are of course possible. While these various choices leave the equilibrium phase diagram intact, the resulting nonequilibrium steady state in the presence of active processes will depend on the specific choice that is made. However, we have checked that alternative choices involving only local moves, *e.g.* $\alpha_1 = \alpha e^{-\frac{1}{2}\beta\Delta\mathcal{H}(\boldsymbol{r})}$ and $\alpha_2 = \alpha e^{\frac{1}{2}\beta\Delta\mathcal{H}(\boldsymbol{r})}$ or $\alpha_1 = \alpha e^{-\beta\Delta\mathcal{H}(\boldsymbol{r})}$ and $\alpha_2 = \alpha$, although they affect the specific location of phase and local stability boundaries, do not alter our physical conclusions for physically relevant values of c_0, μ and η_1 for which the effects of the active binding process do not dominate the ones of the thermal processes. Note that with our choice of rates that saturate when the energy difference increases by a large amount across a configuration change, we mimic the chemical/physical reality according to which diffusion constants are bounded.

The last two terms in Eq. (3.19) describe the active binding (η_1) and active unbinding (η_2) processes. Since the rates η_1 and η_2 are constant, these terms violate detailed balance and constitute the source of nonequilibrium. The second equation, which describes the dynamics of the membrane shape h, assumes a simple local dissipative dynamics with mobility Λ. Hydrodynamic interactions are thus neglected. We now switch to dimensionless units by setting $a = T = m = 1$. In other words, we take $a^2/(mT)$ as the unit of time.

Let us first investigate the steady state for the flat uniform state. The dynamical equation for ρ becomes

$$\begin{aligned}\dot{\rho} =& \alpha(1-\rho)\frac{e^{-(\kappa_b c_0^2-\mu)}}{1+e^{-(\kappa_b c_0^2-\mu)}} - \alpha\rho\frac{e^{\kappa_b c_0^2-\mu}}{1+e^{\kappa_b c_0^2-\mu}} \\ &+ \eta_1(1-\rho) - \eta_2\rho,\end{aligned} \tag{3.21}$$

and the steady-state solution is therefore

$$\bar{\rho}_0 = \frac{\alpha\rho_0 + \eta_1}{\alpha + \eta_1 + \eta_2}, \tag{3.22}$$

with ρ_0 given in Eq. (3.4). Note that $\bar{\rho}_0$ reduces as expected to ρ_0 in the absence of activity.

To perform a linear stability analysis in this nonequilibrium situation, we consider a small perturbation $h = h_1(\boldsymbol{r})$, $\rho = \bar{\rho}_0 + \rho_1(\boldsymbol{r})$ and $L = L_0 + L_1$, where L_1 is given by Eq. (3.5) in order to conserve the membrane area. To second order in the perturbation, we

find that $\hat{\mathcal{F}}$ takes the same form as Eq. (3.8) except for an additional term $\rho_1 \ln\{[\bar{\rho}_0(1-\rho_0)]/[\rho_0(1-\bar{\rho}_0)]\}$ in the integrand. At first order in the perturbation, the dynamical equations (3.19) and (3.20) take then the form

$$\begin{pmatrix} \dot{h}_{1,\boldsymbol{q}} \\ \dot{\rho}_{1,\boldsymbol{q}} \end{pmatrix} = -\mathsf{M} \begin{pmatrix} h_{1,\boldsymbol{q}} \\ \rho_{1,\boldsymbol{q}} \end{pmatrix}, \tag{3.23}$$

with

$$M_{11} = \Lambda \left(\bar{\kappa}_{\text{eff}} q^4 + \gamma q^2 \right), \tag{3.24}$$

$$M_{12} = \Lambda \kappa_b c_0 q^2, \tag{3.25}$$

$$M_{21} = \kappa_b c_0 q^2 \left(\bar{s} q^2 + \alpha s \right), \tag{3.26}$$

$$M_{22} = q^2 + \eta_1 + \eta_2 + \alpha, \tag{3.27}$$

where $\bar{\kappa}_{\text{eff}} = (1-\bar{\rho}_0)\kappa_u + \bar{\rho}_0 \kappa_b$, $s = \rho_0(1-\rho_0)$ and $\bar{s} = \bar{\rho}_0(1-\bar{\rho}_0)$.

The flat state is unstable when M has negative eigenvalues. Since $\text{tr}(\mathsf{M})$ is positive, this is achieved when $\det(\mathsf{M}) < 0$. Let us first discuss the equilibrium case again. For $\eta_1 = \eta_2 = 0$ and $\rho_0 = \bar{\rho}_0$, we get $\mathsf{M} = \mathsf{D}\,\mathsf{M}_{\text{eq}}$, with $\mathsf{D} = \text{diag}(\Lambda, s(q^2+\alpha))$ and M_{eq} given by Eq. (3.10). Since D is diagonal with strictly positive eigenvalues, the instability occurs when $\det(\mathsf{M}_{\text{eq}}) < 0$ in agreement with the equilibrium condition of Section 3.2.1.

In the general nonequilibrium case, the condition $\det(\mathsf{M}) < 0$ yields an instability region that is shifted relative to the equilibrium case (Fig. 3.6). Both in the active binding and unbinding cases, the instability is shifted towards larger values of c_0, whereas it is shifted towards larger values of μ in the unbinding case and towards lower values of μ in the binding case.

While our linear stability analysis predicts that the homogeneous phase is destabilized for active binding when c_0 exceeds a (η_1-dependent) threshold value (see Fig. 3.6(b)), we also note that the instability region has a similar shape for active binding and for active unbinding at moderate c_0 values, as seen in Fig. 3.6(c). However, we believe that the instability driven by a nonzero η_1 at large c_0 may not yield a simple SC phase, as more drastic nonlinear phenomena could take over in this regime. And as a matter of fact, in the simulations presented later in Section 3.3, right below Eq. (3.30), we have not considered the possibility of active binding, as the destabilization we have found translates, in terms of the self-assembled membrane, into particles detaching away and eventually dissolving the membrane.

3.2.4 Casimir-like interactions

In the previous sections, we have adopted a mean-field approach. Here we wish to study whether equilibrium fluctuation-induced forces, i.e., Casimir-like interactions, can induce a transition between the unbound flat phase (U) and the bound flat phase (B). If this transition exists, it must be of first order since the two phases have the same symmetries. To isolate the Casimir effect, we take $c_0 = 0$ and $\kappa_b \to \infty$, so that the only effect of

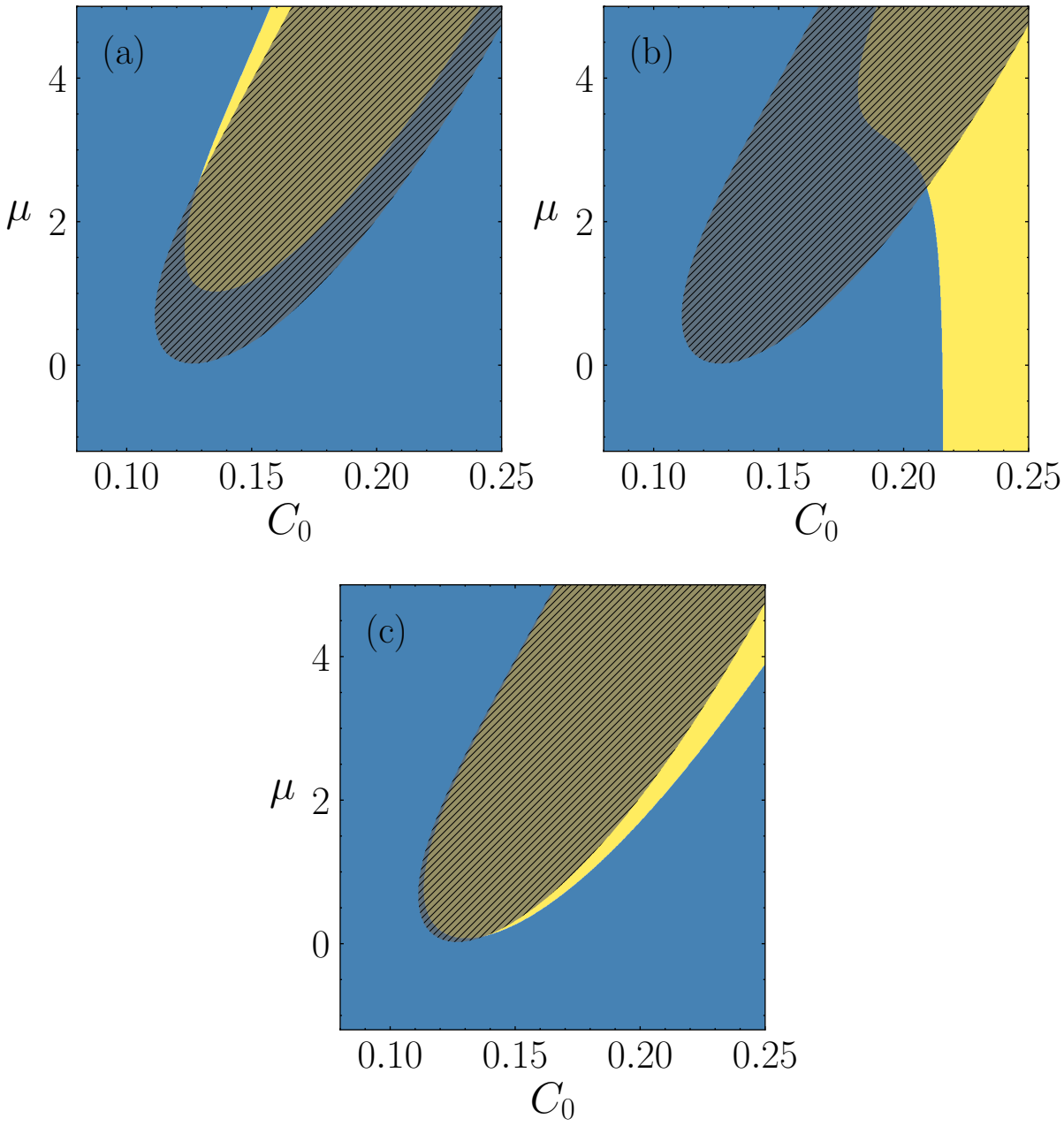

Figure 3.6 – Linear stability analysis in the presence of active binding and active unbinding. In the blue region, the flat membrane is stable against small perturbations, while in the yellow region, it is unstable. The hatched domain refers to the linearly unstable region in the equilibrium phase diagram of Fig. 3.3. (a) Active unbinding for $\eta_1 = 0$ and $\eta_2 = 1$. (b) Active binding for $\eta_1 = 1$ and $\eta_2 = 0$. (c) Active binding for $\eta_1 = 0.02$, $\eta_2 = 0$. At small values of η_1 and c_0, there is no qualitative difference with (a) in terms of the shape of the instability region. Parameters are $\kappa_u = 16$ and $\kappa_b = 144$, $\gamma = 0.5$ and $\alpha = 1$. Note that these phase diagrams are independent of Λ.

the adsorbed proteins is to locally stiffen the membrane. Because the protein has a zero spontaneous curvature, the SC phase will be absent. So, upon increasing μ we may either have a continuous increase of the protein density or a first-order phase transition.

Even in this simplified situation, it is very difficult to calculate exactly the free energy of the system for a given spatial distribution of proteins. We are going to rely on estimates based on the pointlike theory of Ref. [103]. In this work, the size a of the protein inclusions is set by an upper wavevector cutoff, which allows to recover the results of Ref. [55] for two extended inclusions. The multibody Casimir interaction is found to be exactly pairwise additive at leading order, given by the sum of $-6T(a/R_{ij})^4$, where the R_{ij}'s are the distances between pairs of inclusions. Note that contrary to the results of Ref. [109] for pinning inclusions, screening effects are very weak and occur only at the next orders.

At contact, i.e., for $R = 2a$, which corresponds to the distance between nearest neighbors (NN), the above interaction gives $E_{\mathrm{NN}} \simeq -0.4\,T$. For $R = 2\sqrt{2}a$, which corresponds to next nearest neighbors (NNN) in a square lattice, the interaction falls to 25% of this value, while for $R = 4a$, i.e., for second neighbors, it falls to 6%, which we will consider negligible. Note that these values should only be taken as estimates since only the leading-order interaction has been taken into account, while at such short distances higher-order terms and multibody corrections are expected to play a significant role (as for curving inclusions [110]). A quick inspection of these corrections in the pointlike model revealed to us an increase in the attractiveness of the Casimir interaction.

To examine the effect of these Casimir interactions, we have performed a Monte Carlo (MC) simulation where particles diffuse on a square lattice, interact through NN and NNN interactions only, and bind to the lattice, or detach from it by exchange with a reservoir of chemical potential μ. The results, shown in Fig. 3.7 indicate that the orders of magnitude given above are almost sufficient to produce an unbound-bound first-order phase transition.

3.3 Simulation Model and Method

In numerical simulations in thermal equilibrium, the protein binding to the membrane has been studied from molecular resolutions [111–113] to large-scale thin-surface membrane models [102, 105, 114–120]. When proteins generate an isotropic spontaneous curvature, bound sites are numerically found to assemble into circular domains or spherical buds [114–117, 119]. On the other hand, bound sites with anisotropic spontaneous curvature have been found to induce membrane tubulation [118–120]. The simulations presented below were performed by Pr. H. Noguchi.

3.3.1 Method

A fluid membrane is numerically modeled in our work by a self-assembled one-layer sheet of N particles (the model is illustrated Fig. 3.2). The position and orientational vectors of the i-th particle are $\boldsymbol{r}_i$ and $\boldsymbol{u}_i$, respectively. In the following we use a meshless membrane model, *i.e.*, the membrane particles are connected by means of an attractive potential.

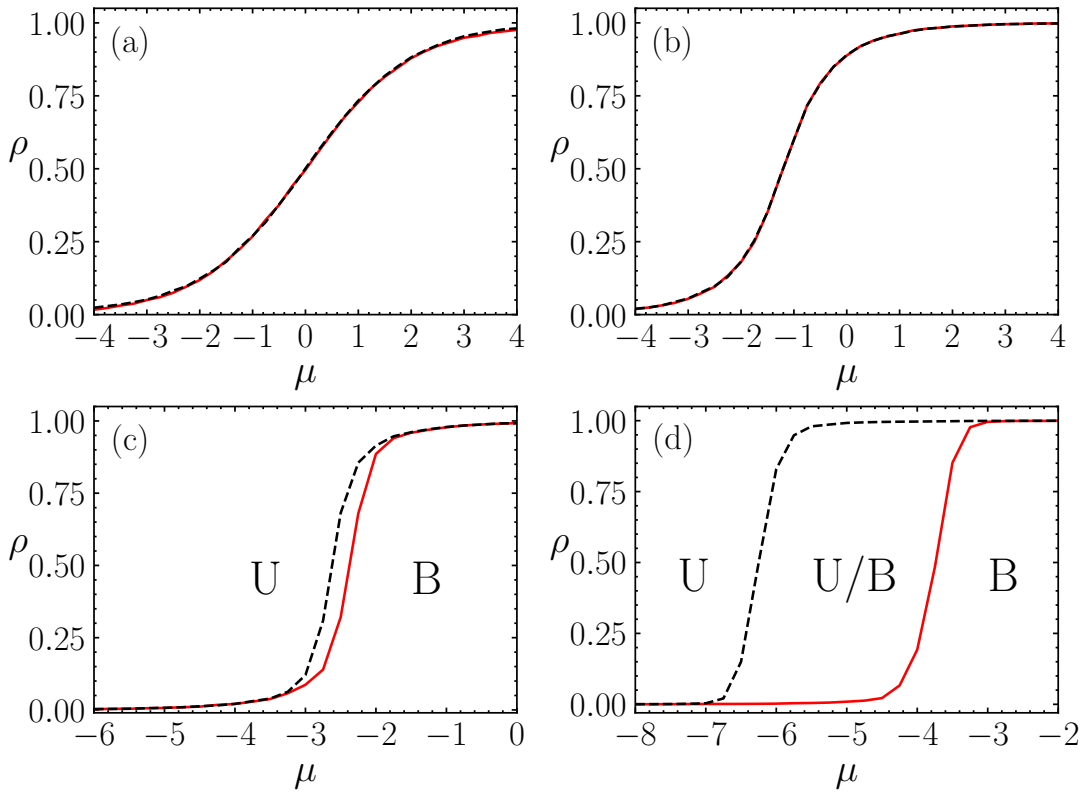

Figure 3.7 – Equilibrium protein inclusion density ρ versus chemical potential μ in an MC simulation of stiff membrane inclusions experiencing pure Casimir-like interactions (pairwise pointlike model). The solid red curve corresponds to an empty lattice initial condition. The dashed black curve corresponds to a fully occupied initial condition. (a) $E_{\rm NN} = E_{\rm NNN} = 0$. (b) $E_{\rm NN} = -0.5\,T$ and $E_{\rm NNN} = -0.1\,T$. (c) $E_{\rm NN} = -T$ and $E_{\rm NNN} = -0.25\,T$. (d) $E_{\rm NN} = -2\,T$ and $E_{\rm NNN} = -0.5\,T$. A first-order phase transition occurs in (c) and (d) as revealed by the coexistence between an unbound (U) and a bound (B) state with different values of ρ.

The model used is described in detail in [121, 122]. Below we review the key ingredients of this simulation.

The membrane particles interact with each other via a potential $U = U_{\rm rep} + U_{\rm att} + U_{\rm bend} + U_{\rm tilt}$. The potential $U_{\rm rep}$ is an excluded volume interaction with diameter σ for all pairs of particles. The solvent is implicitly accounted for by an effective attractive potential as follows:

$$\frac{U_{\rm att}}{T} = 2\sum_i \ln[1+\exp\{-4(\rho_i-\rho^*)\}] - C, \tag{3.28}$$

where $\rho_i = \sum_{j\neq i} f_{\rm cut}(r_{i,j})$, C is a constant, and ρ^* is the characteristic density with $\rho^* = 7$. $f_{\rm cut}(r)$ is a C^∞ cutoff function [121] and $r_{i,j} = |\mathbf{r}_{i,j}|$ with $\mathbf{r}_{i,j} = \mathbf{r}_i - \mathbf{r}_j$:

$$f_{\rm cut}(r) = \begin{cases} \exp\{b(1+\frac{1}{(r/r_{\rm cut})^n-1})\} & (r < r_{\rm cut}) \\ 0 & (r \geq r_{\rm cut}) \end{cases} \tag{3.29}$$

where $n = 6$, $b = \ln(2)\{(r_{\rm cut}/r_{\rm att})^n - 1\}$, $r_{\rm att} = 1.9\sigma$, and $r_{\rm cut} = 2.4\sigma$. The set of

parameters used above is described in detail in Ref. [123].

The bending and tilt potentials are given by $U_{\rm bend}/T = (k_{\rm bend}/2)\sum_{i<j}(\boldsymbol{u}_i - \boldsymbol{u}_j - C_{\rm bd}\hat{\boldsymbol{r}}_{i,j})^2 w_{\rm cv}(r_{i,j})$ and $U_{\rm tilt}/T = (k_{\rm tilt}/2)\sum_{i<j}[(\boldsymbol{u}_i\cdot\hat{\boldsymbol{r}}_{i,j})^2 + (\boldsymbol{u}_j\cdot\hat{\boldsymbol{r}}_{i,j})^2] w_{\rm cv}(r_{i,j})$, respectively, where $\hat{\boldsymbol{r}}_{i,j} = \boldsymbol{r}_{i,j}/r_{i,j}$ and $w_{\rm cv}(r_{i,j})$ is a weight function. The energy $U_{\rm bend}$ penalizes the splay of $\boldsymbol{u}_i$, and hence penalizes the curvature of the membrane when $C_{\rm bd} = 0$, while it favors a spontaneous curvature $c_0 = C_{\rm bd}/(2\sigma)$ when $C_{\rm bd}$ is nonzero [122]. As for $U_{\rm tilt}$, it penalizes the lipid tilt, therefore favors the normal orientation of the lipids relative to the membrane plane.

The membrane consisting of 25 600 membrane particles is simulated under periodic boundary conditions with $N\gamma T$ ensemble, where γ is the surface tension that is conjugate to the projected area onto the xy plane as defined in Section 3.2. The projected area of the square membrane ($A_p = L_p^2$) is a fluctuating quantity [124, 125]. The motion of the particle position $\mathbf{r}_i$ and the orientation $\mathbf{u}_i$ are given by underdamped Langevin equations, which are integrated by the leapfrog algorithm [126, 127] with $\Delta t = 0.002\tau_0$ where $\tau_0 = \sigma^2/D_0$ for the time unit, where D_0 is the diffusion coefficient of the free membrane particles.

Here, each membrane particle is a binding site and can be found in two—bound or unbound—states. In this study, $c_0 = 0$ and $k_{\rm bend} = k_{\rm tilt} = 10$ for the unbound membrane particles and $k_{\rm bend} = k_{\rm tilt} = 80$ for the bound membrane particles, in which $\kappa_u/T = 16\pm1$ and $\kappa_b/T = 144 \pm 7$. In the bending and tilt potentials, for a pair of neighboring bound and unbound particles, we use the mean value $k_{\rm bend} = k_{\rm tilt} = 45$. We find that the ratio of the Gaussian modulus $\bar{\kappa}$ to κ is uniform, independently of the local binding fraction [128]: $\bar{\kappa}/\kappa = -0.9 \pm 0.1$.

In the following, we shall mainly consider tensionless membranes and membranes with tension $\gamma = 0.5T/\sigma^2$. With typically $\sigma \approx 10\,\text{nm}$ and $T \approx 4\times10^{-21}\,\text{J}$, this corresponds to an average tension $\approx 0.02\,\text{mN/m}$, well below usual lysis tensions (1–25 mN/m) [129–131].

For the unbound particles, the membrane area per particle is $1.251\sigma^2$ and $1.257\sigma^2$ at $\gamma = 0$ and $0.5T/\sigma^2$, respectively. It is slightly larger (by a few percent) for bound particles: $1.294\sigma^2$ and $1.300\sigma^2$ at $\gamma = 0$ and $0.5T/\sigma^2$, for $c_0\sigma = 0.1$. The unit length a of the theory (governing the surface area a^2 covered by a bound protein, defined in Section 3.2) is thus found to be $a \simeq 1.1\sigma$.

The bound and unbound states are stochastically switched by a Metropolis MC procedure with the acceptance rate $p_{\rm acpt}$:

$$p_{\rm acpt} = \begin{cases} \exp(\pm\Delta H/T) & \text{if } \pm\Delta H < 0, \\ 1 & \text{otherwise,} \end{cases} \tag{3.30}$$

where the $+$ and $-$ signs refer to the unbinding and binding processes, respectively. Here, $\Delta H = \Delta U - \mu$ where ΔU is the energy difference between the bound and unbound states and μ is the chemical potential of particles attempting to bind. We also consider active unbinding in which the particles change from bound to unbound states with a rate η_2 independent of the state of the system, as defined in Eq. (3.18). Our simulations are carried out at $\eta_1 = 0$, otherwise, membrane particles spontaneously detach, because active binding can lead to a higher bending energy than the attractive energy between membrane

particles. In thermal equilibrium ($\eta_2 = 0$), static properties are independent of the rates of the binding/unbinding processes. Out of equilibrium, however, the steady-state reached by the system *a priori* depends on the details of the binding and unbinding processes (compared with the thermal binding-unbinding rates and with the membrane dynamics), as long as the detailed balance is broken. Here, we choose to consider relatively fast binding/unbinding processes compared to the membrane motion. For each membrane particle, the Metropolis MC and active unbinding processes are performed every $\tau_\mathrm{b} = 0.01\tau_0$ with probabilities $\alpha_\mathrm{mp}\tau_\mathrm{b}$ and $\eta_2\tau_\mathrm{b}$ respectively. We fix $\alpha_\mathrm{mp}\tau_0 = 10$ and vary the ratio $\eta_2/\alpha_\mathrm{mp}$ in our investigation. The binding fraction is essentially controlled by the ratio $\eta_2/\alpha_\mathrm{mp}$, as the binding/unbinding is faster than membrane deformation. We have checked it by varying $\alpha_\mathrm{mp}\tau_0$ at $c_0\sigma = 0.1$, $\gamma = 0.5T/\sigma^2$, and $\mu = 6T$.

In our analysis, in order to characterize the various phases we find, we resort to the concept of cluster. Two sites are considered to belong to the same cluster when the distance between them is less than r_att. The probability $P(i_\mathrm{cl})$ that a site belongs to a cluster of size i_cl is $P(i_\mathrm{cl}) = \langle n_\mathrm{cl} i_\mathrm{cl}\rangle/N$, where n_cl is the number of clusters consisting of i_cl sites. The vertical span of the membrane is calculated from the membrane height variance as $z_\mathrm{mb}^2 = \sum_i^N (z_i - z_\mathrm{G})^2/N$, where $z_\mathrm{G} = \sum_i^N z_i/N$.

The results of the simulations are normalized by the particle diameter σ, by temperature T, and by the time step τ_0 for lengths, energies, and times, respectively. The subscripts b and u indicate bound and unbound states, while U, B, and SC refer to the unbound, bound and separated-corrugated phases, respectively. The error bars show the standard deviation calculated from three or more independent runs.

3.3.2 Results

a. Phase separation in thermal equilibrium

We now describe the membrane behavior in thermal equilibrium (without the active unbinding, at $\eta_2 = 0$). First, we work at $c_0 = 0$, so that the only action of the bound and unbound particles is to locally alter the bending rigidity. As the chemical potential μ increases, the membrane exhibits a discontinuous transition from the unbound state (U) to the bound state (B) (see Fig. 3.8). The two states can exist at the same chemical potential in the vicinity of the phase transition. This transition occurs due to the suppression of membrane fluctuations by the high bending rigidity of the bound sites. It is therefore Casimir interactions that drive this transition, as discussed in Section 3.2.4. As the surface tension γ increases, the transition occurs at slightly lower values of μ and the coexistence range becomes narrower.

At this stage, we would like to compare with the theoretical results shown in Fig. 3.7. In both approaches, a first-order transition is observed. Because surface tension flattens out the membrane by stretching it, we expect that Casimir interactions will be all the weaker as surface tension increases. For the finite spontaneous curvatures ($c_0 \neq 0$), the bound sites prefer to assemble to a curved domain leading to the formation of spatial patterns (Figs. 3.9–3.14). At a high spontaneous curvature ($c_0\sigma = 0.1$) and a medium surface tension ($\gamma\sigma^2/T = 0.5$), an SC state, where micro-domains of bound sites are

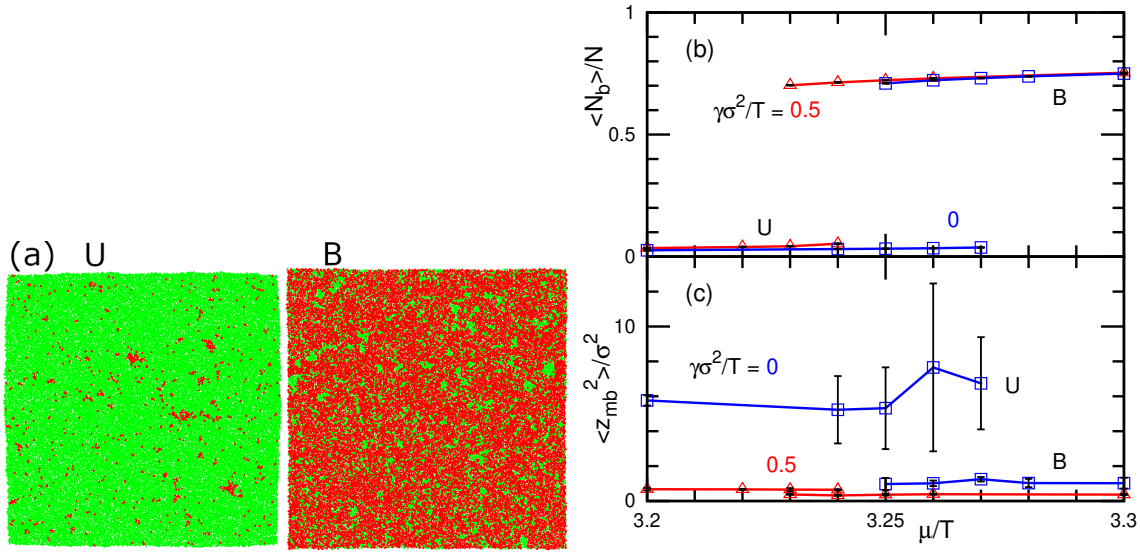

Figure 3.8 – Discontinuous binding transition at $c_0 = 0$ in thermal equilibrium ($\eta_2 = 0$). (a) Snapshots of the unbound (U) and bound (B) phases existing at the same chemical potential $\mu/T = 3.26$ for $\gamma = 0$. The bound and unbound sites are displayed in red and in green, respectively. (b) Binding density $\langle N_b \rangle / N$ and (c) vertical membrane span $z_{\rm mb}$ as a function of the chemical potential μ at $\gamma\sigma^2/T = 0$ and 0.5.

formed, appears between the U and B phases (see Fig. 3.9). To maintain a flat membrane on average under the periodic boundary condition, the bound sites form finite-size bowl-shaped domains and the unbound membrane between the bound domains is bent in the opposite direction [see Figs. 3.9(f)]. When the membrane is sliced along a vertical plane, the cross-section has a bump shape as depicted in Fig. 3.4. A hexagonal-shaped pattern is formed instead of the 1D bump pattern, since a spherical shape is preferred by the isotropic spontaneous curvature. However, the essential feature of the stability is captured in the 1D shape. Similar curved domains can be formed on protein-free membranes. Such curve-shaped domains were observed in three-component lipid vesicles [132–135]. These domains are, however, caused by their strong line tension unlike our case (we have almost no line tension as there is no direct repulsion between bound and unbound particles).

Examples of the initial relaxation dynamics at $\mu/T = 7$ are shown in Movies 1 and 2 provided in the Electronic supplementary information (ESI) of [86]. The unbound domains elongate leading to a percolated network. When initial states are set to the smaller or larger domains obtained at low or high μ, the domains grow or are reduced, respectively, but do not completely converge to the same size even in the long simulation runs by a hysteresis (see Fig. 3.8). In the SC states, the simulations are performed from several different initial states to check this hysteresis. The error bars in Figs. 3.10, 3.11, and 3.16 show the width of the obtained values due to the hysteresis. The bound domain size increases with increasing μ [compare Figs. 3.9(c) and (d)].

At $c_0\sigma = 0.1$ and $\gamma\sigma^2/T = 0.5$, the transition between the U and SC phases is continuous, but the transition between the SC and B phases is discontinuous and two phases coexist around the phase boundary [see Figs. 3.9(d)–(f) and 3.10(a)]. This agrees with the theoretical prediction in Section 3.2.2. To detect the discreteness of the transition between the SC and B states more clearly, the ratio of the average number of sites in the

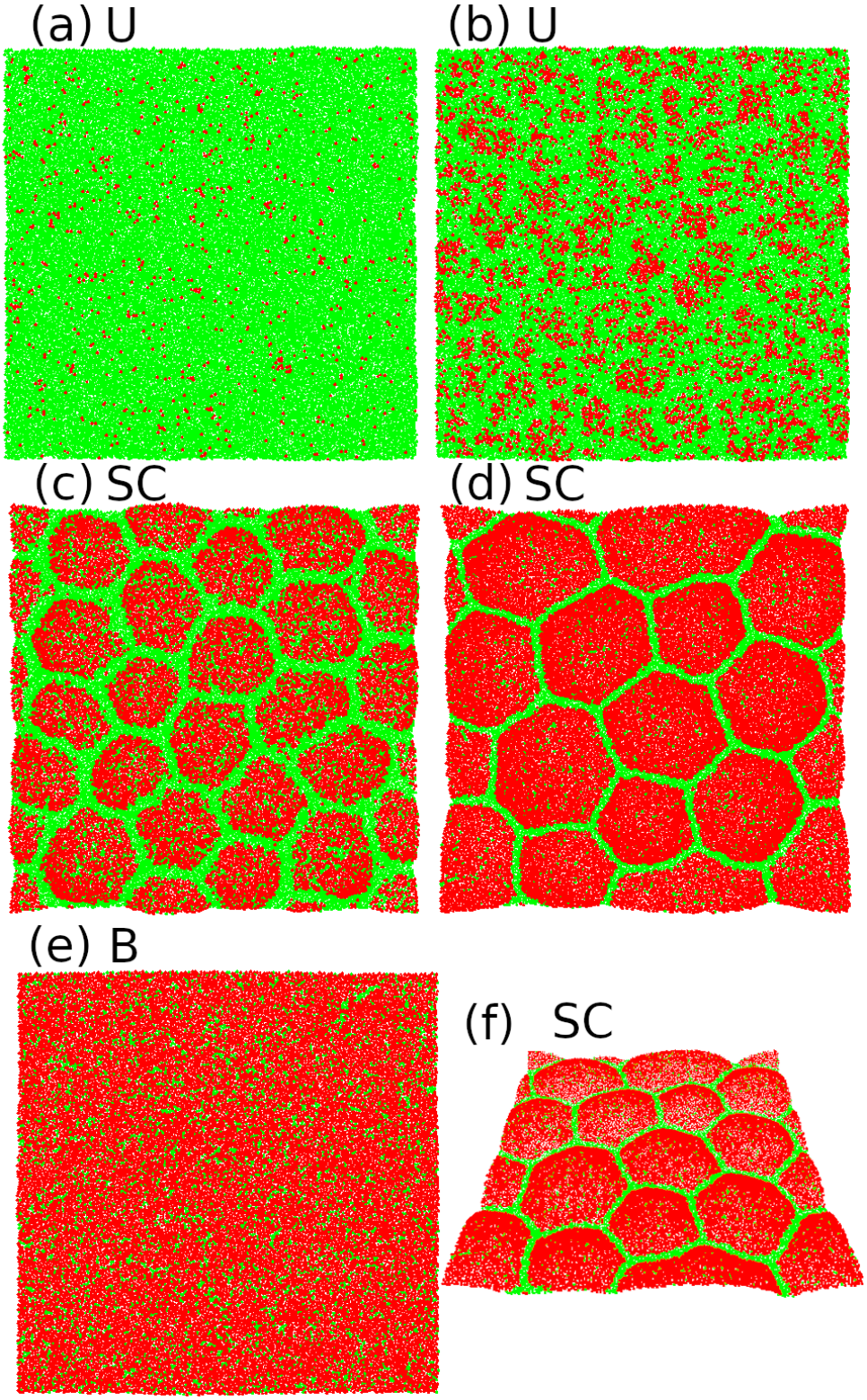

Figure 3.9 – Snapshots of membranes at $c_0\sigma = 0.1$, $\gamma\sigma^2/T = 0.5$, and $\eta_2 = 0$. (a) U phase at $\mu/T = 4$, (b) Close to the phase boundary between U and SC at $\mu/T = 5$, (c) SC phase at $\mu/T = 6$. (d)–(f) SC and B phases at $\mu/T = 8$. The top views are shown in (a)–(e) and a bird's eye view of the snapshot of (d) is shown in (f).

largest unbound cluster to that in the unbound sites, $\langle N_{u,\mathrm{cl}}\rangle/\langle N_u\rangle$, is shown with respect to $\langle N_b\rangle/N$ in Fig. 3.10(b). This ratio is close to unity in the SC phase and close to zero in the B phase because the unbound region percolates. A large gap exists between the two states at $c_0\sigma = 0.08$ and 0.1. In the SC state, most of the unbound sites belong to the largest cluster so that the unbound sites form a single percolated domain. The mean membrane vertical span $\langle z^2_{\mathrm{mb}}\rangle$ also exhibits a discrete gap [see Fig. 3.10(c)], since the SC membranes are largely bent whereas not in the B phase.

For the low spontaneous curvatures ($c_0\sigma = 0.04$ and 0.06 at $\gamma\sigma^2/T = 0.5$) or high surface tension ($\gamma\sigma^2/T = 1$ at $c_0\sigma = 0.1$), the transition between the SC and B phases becomes continuous [see Fig. 3.10 and 3.11]. In the SC phase, the unbound domains are of anisotropic shapes but do not form a fixed network structure so that stable microdomains are not formed (see Fig. 3.12(d) and Movies 3 provided in the ESI of [86]). This corresponds to the single phase at $c_0 < C_{\mathrm{th}}$ in the theory, where the binding ratio gradually changes. For zero or low surface tension ($\gamma\sigma^2/T = 0$ or 0.25), the microdomains of the bound sites form vesicles via budding [Figs. 3.12(a),(b)] or membrane rupture [Fig. 3.12(c)]. Therefore, finite tension is required to stabilize the SC phase.

As theoretically analyzed in Fig. 3.3, the phase boundary of the uniform (unbound and bound) phases is shown in Fig. 3.13. In the region between two lines, the uniform phase does not exist even as a metastable state. At $\eta_2 = 0$, the unstable region becomes wider at higher values of c_0. The lower boundary is determined by the appearance of a peak in the cluster size distribution $P_b(i_{\mathrm{cl}})$ of the bound sites, as shown in Fig. 3.14(a).

b. Phase separation out of equilibrium

In this section, we describe the membrane behavior in the nonequilibrium regime with active unbinding ($\eta_2 > 0$). As η_2 increases, the ratio of the bound sites linearly decreases, and the bound and unbound sites are mixed more randomly as shown in Figs. 3.15 and 3.16(a). From Fig. 3.16(b), we see that the SC phase becomes unstable and eventually disappears as η_2 is increased at not that large chemical potential. This property is also apparent in Fig. 3.13 where the lower boundary rises upwards. As the fraction of bound sites decreases with increasing η_2, the domain structure in the SC phase becomes less pronounced (Fig. 3.15), and the membrane adopts a flatter shape (Fig. 3.16(c)). The SC and uniform phases are clearly distinguished from the fraction of unbound sites belonging to the largest cluster at $\mu/T = 7$ and 7.5, while, as η_2 is increased, the SC phase is continuously blurred out when $\mu/T \lesssim 6.5$ (Figs. 3.16(b)). With increasing η_2, $P_b(i_{\mathrm{cl}})$ has a lower and broader peak, and subsequently, it monotonously decreases (see Fig. 3.14(b)). This is different from the transition between the U and SC phases in equilibrium, where large clusters are exponentially rare in the U phase, as shown in Fig. 3.14(a).

In the theoretical analysis of Section 3.2 we observe (Fig. 3.6(a)) that a nonzero η_2 shifts the lower boundary of the yellow metastability region upwards, in agreement with the simulation results in Fig. 3.13, but it also shifts its upper boundary upwards, which is not consistent with the observed numerics (Fig. 3.13). Such nonequilibrium features as the increased fuzziness cannot be accounted for within the framework of linear stability analysis.

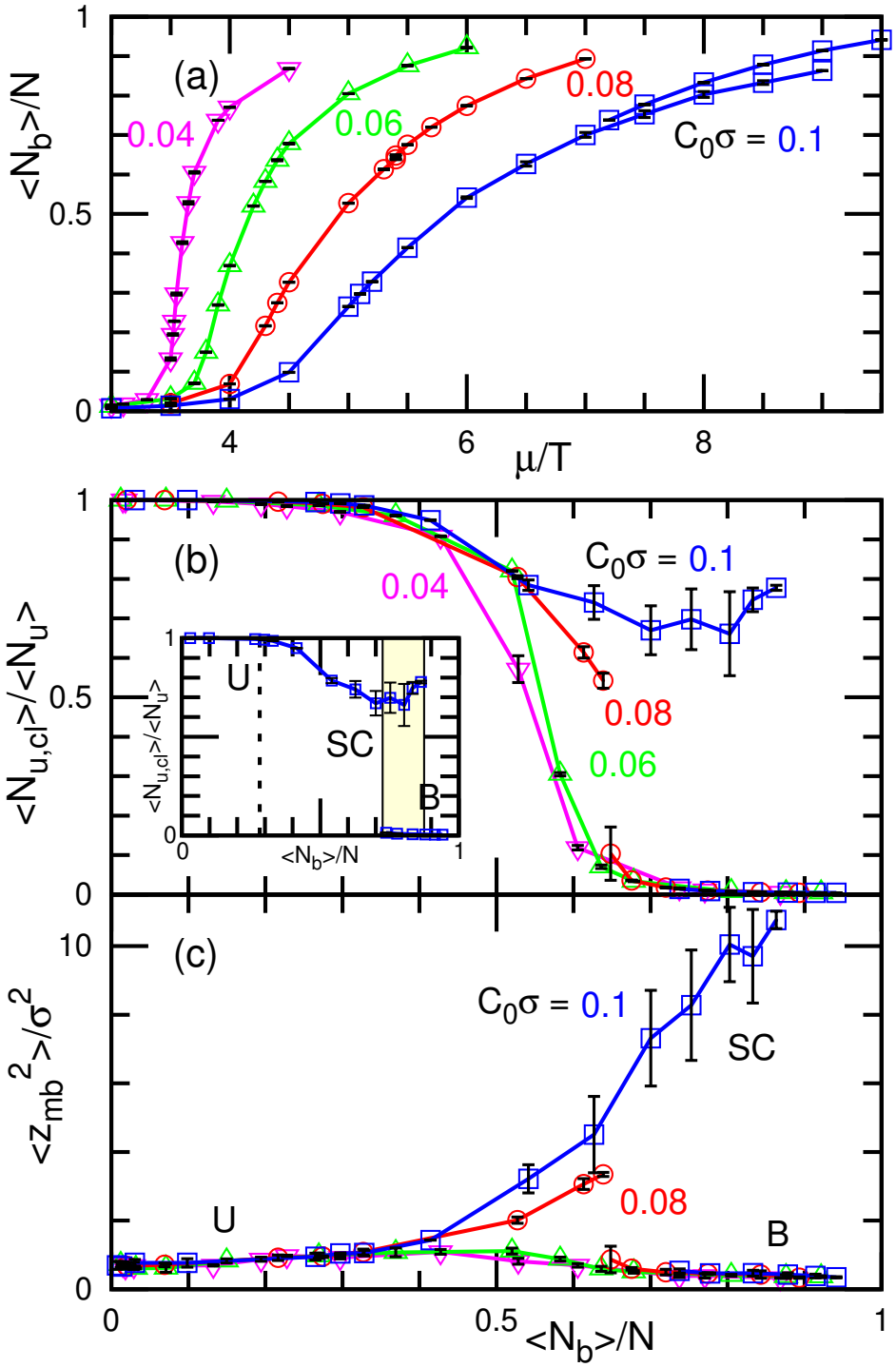

Figure 3.10 – Binding at $\gamma\sigma^2/T = 0.5$ and $\eta_2 = 0$. (a) binding density $\langle N_b\rangle/N$. (b) ratio of the largest cluster of unbound sites $\langle N_{u,\mathrm{cl}}\rangle/\langle N_u\rangle$. As shown for $c_0\sigma = 0.1$, the U, SC and B phases can be determined by the value of $\langle N_{u,\mathrm{cl}}\rangle/\langle N_u\rangle$. The dashed line corresponds to the transition between the U and SC phases and the yellow domain corresponds to the region where the SC and B phases coexist. (c) vertical membrane span z_{mb}.

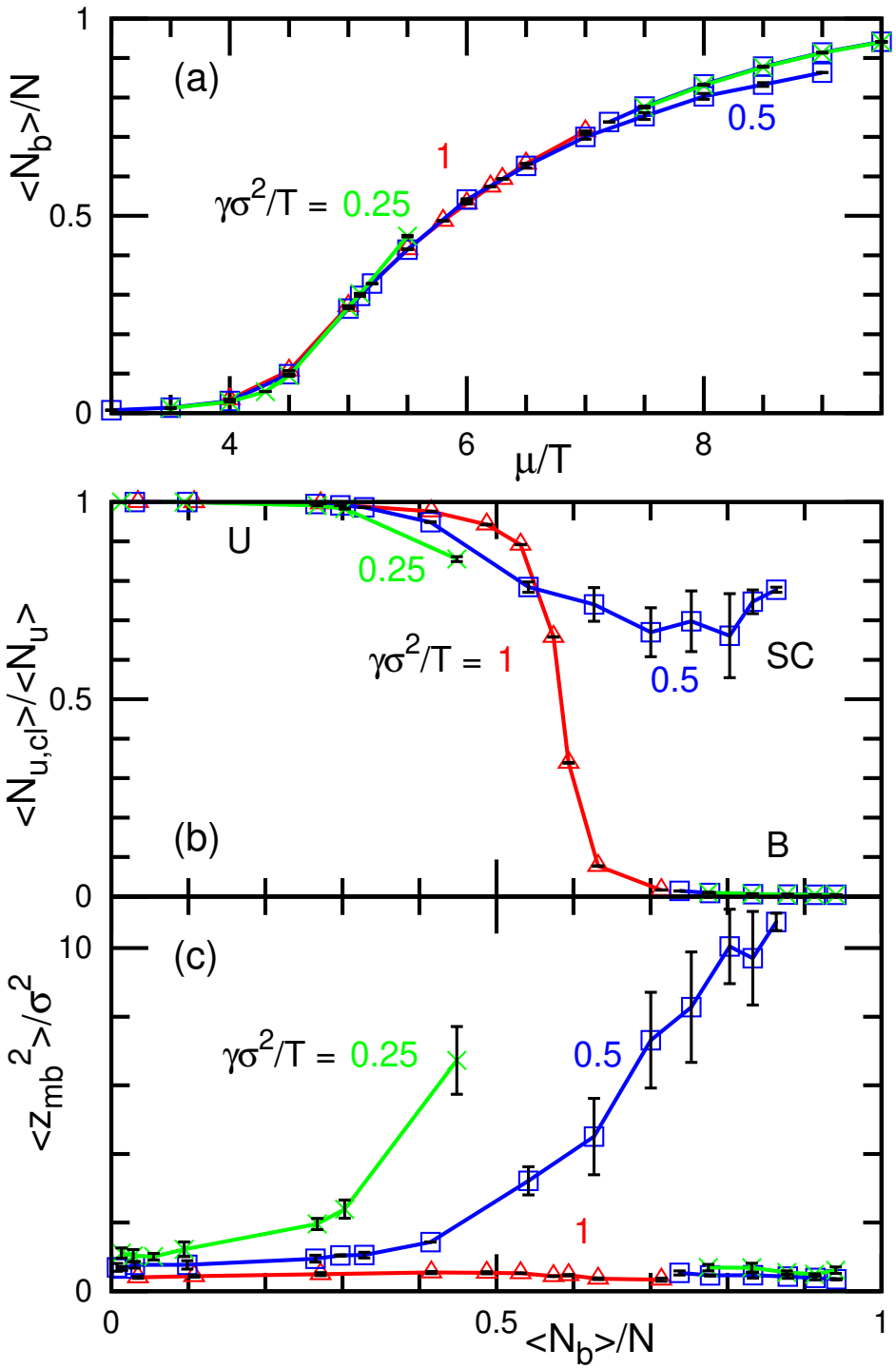

Figure 3.11 – Surface tension γ dependence at $c_0\sigma = 0.1$ and $\eta_2 = 0$. (a) Binding density $\langle N_b\rangle/N$. (b) ratio of the largest cluster of unbound sites $\langle N_{u,\mathrm{cl}}\rangle/\langle N_u\rangle$. (c) vertical membrane span z_{mb}. At $\gamma\sigma^2/T = 0.25$, the SC phase is unstable for $\mu/T \gtrsim 6$.

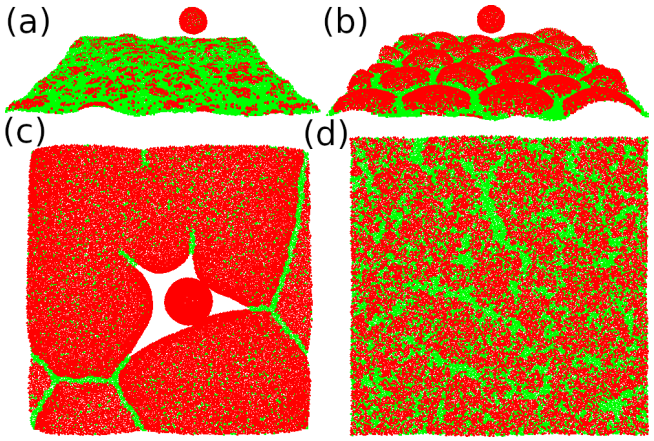

Figure 3.12 – Snapshots of membranes at $\eta_2 = 0$. (a),(b) Vesicle formation (a) at $c_0\sigma = 0.1$, $\gamma = 0$, and $\mu/T = 4.7$ and (b) at $c_0\sigma = 0.1$, $\gamma\sigma^2/T = 0.25$, and $\mu/T = 6$. (c) Membrane rupture at $c_0\sigma = 0.1$, $\gamma\sigma^2/T = 0.25$, and $\mu/T = 8.5$. (d) Anisotropic clusters of unbound particles at $c_0\sigma = 0.06$, $\gamma\sigma^2/T = 0.5$, and $\mu/T = 4.3$. Bird's eye and top views are shown in (a),(b) and in (c),(d), respectively.

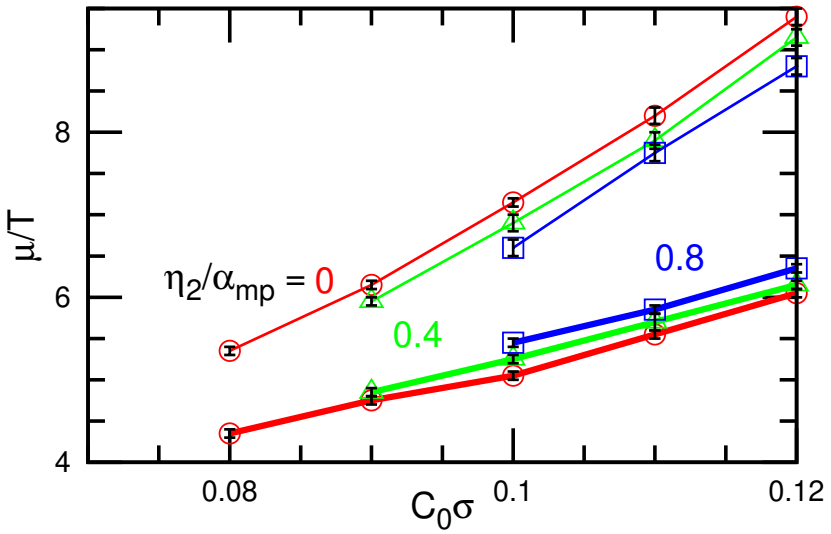

Figure 3.13 – Phase boundaries for the metastability of the unbound (lower branch) and bound (upper branch) states for $\eta_2/\alpha_{\rm mp} = 0$ ($\circ$), 0.4 ($\triangle$), and 0.8 ($\square$) at $\gamma\sigma^2/T = 0.5$. The unbound and bound states exist as stable or metastable states in the regions below the lower line and above the upper line, respectively. The membrane is phase-separated in the region between two lines. Note that the membrane continuously changes from the U to B phases at $\mu/T = 0.06$. We conjecture that the red branches eventually merge at around $c_0\sigma \simeq 0.06$ and continue into a line for lower values of $c_0\sigma$.

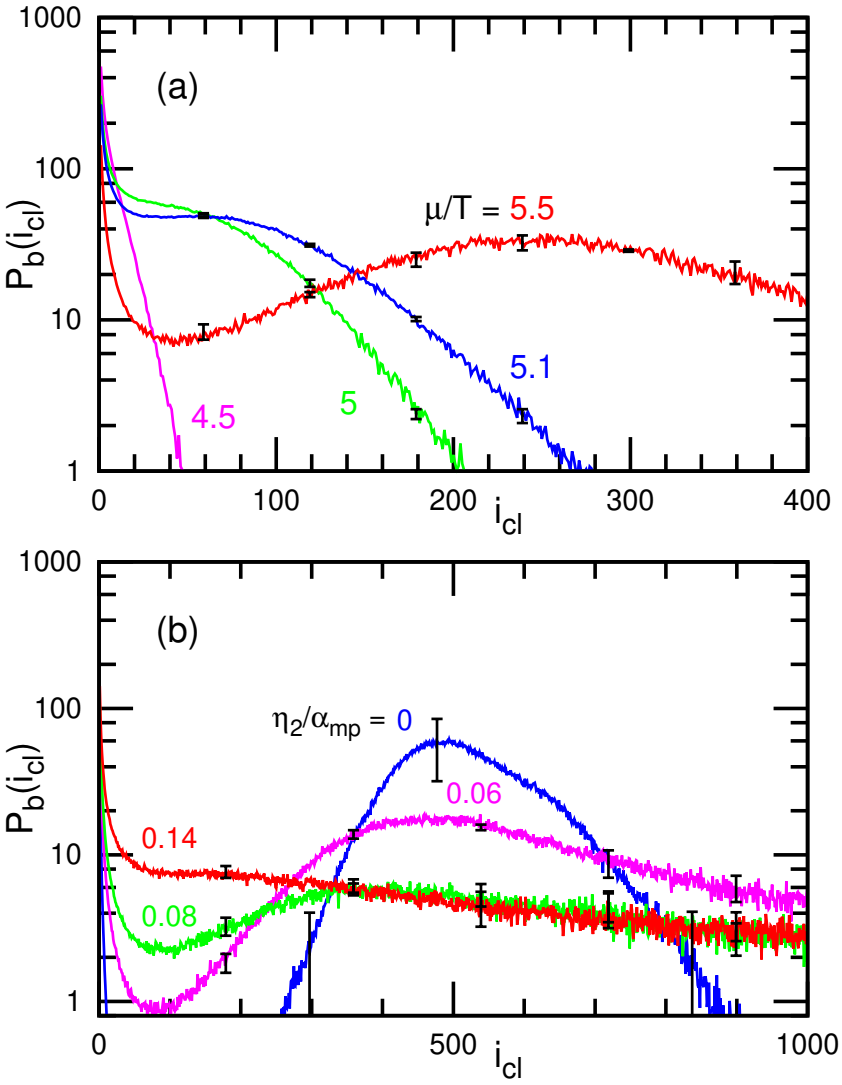

Figure 3.14 – Size distribution $P_b(i_{\rm cl})$ of bound-site cluster at $c_0\sigma = 0.1$ and $\gamma\sigma^2/T = 0.5$. (a) $\mu/T = 4.5$, 5, 5.1, and 5.5 at $\eta_2 = 0$. (b) $\eta_2/\alpha_{\rm mp} = 0$, 0.6, 0.8, and 1.4 at $\mu/T = 6$.

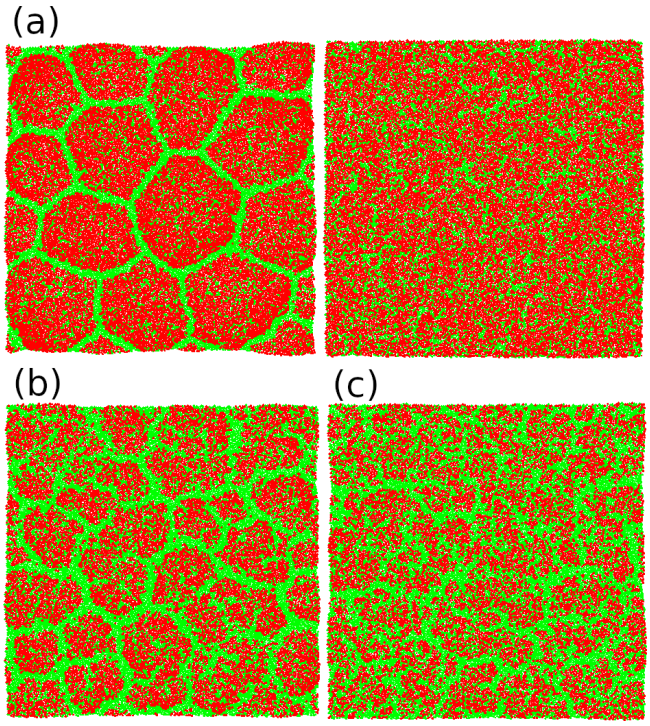

Figure 3.15 – Snapshots of membranes with active unbinding at $c_0\sigma = 0.1$ and $\gamma\sigma^2/T = 0.5$ for (a) $\{\mu/T, \eta_2/\alpha_{\rm mp}\} = \{7, 0.08\}$, (b) $\{6, 0.06\}$, and (c) $\{6, 0.12\}$.

3.4 Comparison between theory and simulations

The aforementioned theoretical and simulation results agree qualitatively well, but some differences are seen. We now discuss these in more detail. In comparing the phase diagrams in Figs. 3.3 and 3.13, the chemical potential μ for the SC phase is roughly $5T$ higher in the simulation than μ in the theory, but the range of the SC phase is compatible. In the theory, the binding changes only the bending energy. Conversely, in the simulation, it also modifies the other energy ($U_{\rm rep}, U_{\rm att}$) and the local membrane area is slightly changed by the binding. Hence, this shift of μ might be caused by this different energy change so that higher μ is required for binding to occur in the simulation. On the other hand, the differences in the typical threshold values of c_0 in the phase diagrams are small. Part of these differences are due to the differences in the length units ($a \simeq 1.1\sigma$), and the rest are likely due to thermal fluctuations. Indeed, the phase boundaries can be affected by thermal fluctuations.

In the analytical approach, a first-order transition between U and SC phases is predicted in the vicinity of the critical point ($c_0 < C_{\rm th}$), as shown in Fig. 3.3. By contrast, this transition is always found to be continuous in the simulation. Since this appears only in the vicinity of the critical point, the free-energy barrier between the two states is presumably small. Thermal fluctuations may smear out the free-energy barrier in the simulation.

The active unbinding shrinks the region of the SC phase in the phase diagram of the simulation (see Fig. 3.13). By contrast, a shift to higher μ is predicted in the analytical model (see Fig. 3.6(a)). This difference may be due to the setting of the bind-

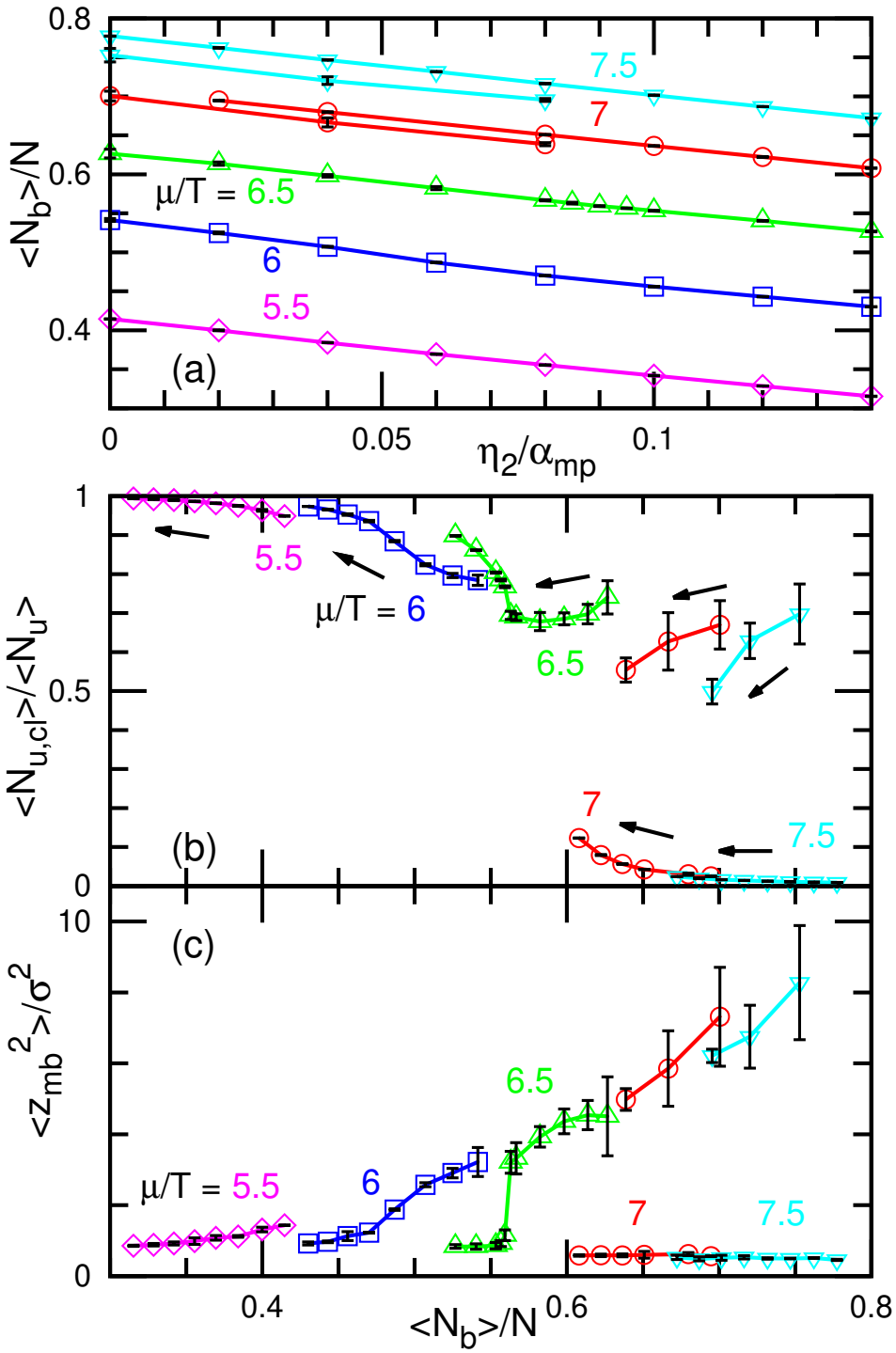

Figure 3.16 – Membrane with active unbinding at $c_0\sigma = 0.1$ and $\gamma\sigma^2/T = 0.5$. (a) Binding density $\langle N_b\rangle/N$ as a function of the active unbinding rate η_2. (b) Ratio of the largest cluster of (a) unbound sites $\langle N_{u,\mathrm{cl}}\rangle/\langle N_u\rangle$ as a function of the binding density $\langle N_b\rangle/N$. The black arrows show the direction of increasing η_2. (c) Vertical membrane span z_{mb}.

ing/unbinding using different choices for the rates $\alpha_{1,2}$ and $\alpha_{\rm mp}p_{\rm acpt}$ in the continuum equation and in the MC method.

3.5 Conclusion

In this chapter, we have studied the structuring of membranes interacting with binding molecules that locally constrain the membrane curvature and increase its bending rigidity. Our analysis has relied on simulations of a meshless membrane model and on an analytical coarse-grained description of the dynamics (based on the Helfrich energy).

In thermal equilibrium, without any active binding/unbinding, we have found that for high spontaneous curvatures and intermediate densities, bound sites locally self-assemble into a bowl-like shape. The membrane then exhibits, at the macroscopic scale, a hexagonally corrugated shape (SC phase). At low density or high density, the membrane adopts a flat state with a uniform distribution of particles (unbound or bound phase, respectively). Second and first-order transitions occur between the SC and unbound phases and between the SC and bound phases, respectively. For a small nonzero spontaneous curvature or under high surface tension, the density of bound sites gradually increases from the completely unbound state up to the bound state as the chemical potential is increased. At zero spontaneous curvature, we have found that Casimir-like interactions induce a first-order transition from the unbound to bound states. Both analytical approaches and simulations agree with each other.

Out of equilibrium, in the presence of an active binding or unbinding, our analytical analysis, based on Glauber equilibrium transition rates, predicts a shift of the SC phase towards higher spontaneous curvatures, as observed in the simulations. It also predicts a shift of the SC phase to lower chemical potentials in the active binding case and to higher chemical potentials in the active unbinding case, while the simulations show a simple shrinkage of the SC phase in the latter case. We expect this discrepancy to be due to the difference in the implementation of the equilibrium transition rates (Glauber vs Metropolis). Simulations show that active unbinding makes the bowl-shaped domains of the SC phase fuzzier. We observe that the SC phase disappears at small curvatures, and because we have a discontinuous transition between the U and B phases at zero curvature, we conjecture the closing of the SC phase is continued by a line connecting to that zero curvature point.

Casimir interactions are the result of thermal fluctuations. Because of their attractive nature, we expect a difference between simulations (that take these forces into account) and the nonlinear analysis which neglects fluctuations. Casimir forces act as a stabilizing force for the SC phase, which should thus appear for a broader range of parameters in the simulation than in the analysis of the mean-field PDEs.

We have assumed the thermal and active binding/unbinding rates to be time-independent. This means that the protein diffusion in the bulk is faster than the binding/unbinding and the protein concentration of the bulk in the vicinity of the membrane surface is maintained constant. However, it is known that large proteins exhibit slow diffusion and the lowering of the density of proteins in the vicinity of the membrane suppresses the binding.

When the binding/unbinding is compatible and faster, the dynamics of the protein in the bulk might also play an important role in determining the nonequilibrium steady state, in which a convection flow may be generated. And in fact, a more realistic description should also incorporate the combined hydrodynamics of the membrane and of the solvent and the diffusion/convection of the bulk particles.

Chapter 4

Pointlike modeling of a diffusing membrane protein

In this chapter, we present analytical generalizations of the Saffman-Delbrück's (SD) law (mobility of a bio-membrane protein) obtained from the velocity field produced by a pointlike force in a 2D fluid embedded in a 3D bulk and by using a small wavelength cutoff of the order of the protein's size. First, we show that this method gives a very good analytical approximation of the usual SD law. Furthermore, we are able to take into account the bilayer nature of the membrane and the intermonolayer friction, as well as derive the correction to the SD law for a protein that creates a local spontaneous curvature. For a protein spanning a flat bilayer, the SD law is found to hold by replacing the viscosity of the membrane with the sum of the monolayer viscosities, without the influence of the intermonolayer friction as long as it is above a threshold well below known experimental values in practice. For a protein located in or adhering to only one of the two monolayers, the SD law is influenced by the intermonolayer friction when the latter is below a threshold that depends on the monolayer viscosity and the protein size. Finally, for a protein inducing a local isotropic spontaneous curvature, we show that the total friction is the sum of the SD friction and that due to the pull-back created by the membrane deformation, a point that was assumed without demonstration in the literature. This work was published in [136].

4.1 Introduction

As mentioned in Sec. a., An object moving in a viscous fluid under the action of an applied force generates a flow and acquires a velocity proportional to the mobility. In three dimensions (3D), at low Reynolds numbers, Stoke's law states that the mobility of a spherical particle of radius a dragged in a fluid of viscosity η, is given by $\mu_{3D} = (6\pi\eta a)^{-1}$ [76]. However, considering the equivalent system in two dimensions (2D), *i.e.*, a disk particle, the mobility diverges, which is known as the Stokes' paradox [76].

To illustrate this, let us consider a protein initially located at the origin of a fluid.

When a pointlike force is applied to the origin of a fluid, the velocity field is given (in the limit of low Reynolds numbers) by the Oseen tensor [76]. In reciprocal space, this reads $\boldsymbol{v}(\boldsymbol{q}) = (\eta q^2)^{-1}(\mathbb{1} - \hat{\boldsymbol{q}} \otimes \hat{\boldsymbol{q}})$, where $\mathbb{1}$ is the identity tensor and $\hat{\boldsymbol{q}}$ the unit vector parallel to $\boldsymbol{q}$. Now, assuming that the force is applied to the protein that transmits it to the fluid, we can determine the velocity v_p of the protein by looking at the velocity of the fluid at the origin.

Discarding angular factors, the latter is given by $v_p/f \propto \int \mathrm{d}^d q/(\eta q^2)$, with d the space dimensions. In 3D, this integral converges at low q but diverges at high q, so an ultraviolet cutoff is necessary to regularize. Taking $q_{\max} = 1/a$, where a is the size of the particle, we obtain $v_p/f = 1/(3\pi^2 \eta a)$. We therefore recover the Stokes law except for an incorrect multiplicative factor which can be viewed as an imprecision on the particle's size. In 2D, however, the integral diverges at low q and so the mobility is found to be infinite.

Nevertheless, this infrared divergence can be regularized in two different ways for steady flows: either by restricting the 2D fluid to a finite area or by embedding the infinite 2D fluid in an immiscible 3D fluid [70, 77]. The latter is physically relevant for biological membranes which are surrounded by a 3D bulk. Hence, the Saffman-Delbrück (SD) law states that the mobility of a protein in a membrane of viscosity η_2 embedded in a solvent above and below of viscosity η^+ and η^-, respectively, is given by $\mu_{\mathrm{SD}} = (4\pi\eta_2)^{-1}\{\ln[\eta_2/(\eta a)] - \gamma\}$, where $\eta = \frac{1}{2}(\eta^+ + \eta^-)$ and $\gamma \simeq 0.577$ is Euler's constant [70, 77]. This expression is valid for $a \ll \ell$, with $\ell = \eta_2/(2\eta)$ the Saffman-Delbrück length that regularizes the infrared divergence of the mobility in 2D.

As far as we know, there is no easy way to establish the SD law and its generalizations. Available proofs require heavy calculations [77, 137–139]. In the following, we present an elegant simple derivation based on a pointlike approximation for the protein regularized by a sharp ultraviolet cutoff of the order of the inverse of the protein size. This derivation is not exact, because the dimension of the inclusion is only taken into account up to a multiplicative factor of order unity inside the log. However, since the particle's radius appears within a logarithm in the SD law, it turns out to be excellent. Pointlike approximations are standard in soft matter to calculate interactions among particles [54, 64, 103, 104, 140] and dynamical behaviors such as mobility and diffusion [141–146]. Either sharp cutoffs are used, with excellent approximate results [54, 103, 104, 140, 142], or smooth cutoffs in numerical works that have the effect of distributing the applied forces over small finite regions [141, 143–146].

Owing to the relative simplicity of the pointlike approach, it is possible to go beyond the SD problem and to provide analytical or semi-analytical results while taking into account several additional physical ingredients otherwise too complicated to include in the description, such as (i) the bilayer character of the membrane [146, 147] and (ii) the spontaneous curvature of the inclusion [43, 60, 68].

In Sec. 4.2, we apply our pointlike method to swiftly rederive the well-known SD mobility. In Secs. 4.3.1 and 4.3.2, we take into account the bilayer nature of the membrane, both for a protein embedded in one monolayer and a protein that spans the whole bilayer, respectively. The possibility of a protein that induces a local isotropic curvature of the membrane is considered in Sec. 4.4. Finally, we compare the results we get for a curvature-inducing protein with the literature, especially with [43].

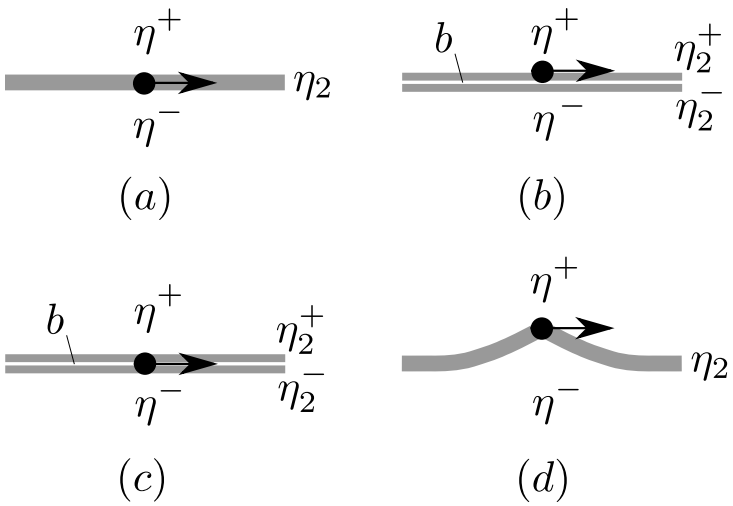

Figure 4.1 – Sketch of a membrane embedded in a solvent with 3D viscosities η^+ above and η^- below. The membrane is treated (a) as a medium with 2D viscosity η_2 (Saffman-Delbrück), (b) and (c) as two adjacent media (monolayers) of 2D viscosities η_2^+ and η_2^-, subject to an intermonolayer friction with coefficient b. In (d) the protein curves locally the membrane. In (a), (c) and (d) the depicted inclusion spans the bilayer membrane; in (b) it is located in the upper monolayer only.

4.2 Pointlike approach to the Saffman-Delbrück mobility

In the Saffman-Delbrück problem, a particle of position $\boldsymbol{R}(t)$ is dragged by a constant force $\boldsymbol{f}$ in a fluid membrane embedded in a solvent (Fig. 4.1a). The membrane is treated as a structureless 2D fluid of viscosity η_2 in the $z = 0$ plane, and inertia is neglected. The membrane lies in a bulk solvent of viscosities $\eta^\pm$ in the two half-spaces (indicated with the superscript $\epsilon = \pm$). Here, contrary to the traditional approach [77] we are going to treat the particle as pointlike, which will greatly simplify the calculations. This entails an approximation, hence validity conditions that we shall discuss in detail at the end of Sec. 4.3.1. Calling $\boldsymbol{v}$ the velocity field in the membrane and $\boldsymbol{V}^\pm$ the velocity fields in the bulk, the equations describing the problem are (see Sec. 2.2.2)

$$\eta^\pm \nabla^2 \boldsymbol{V}^\pm - \boldsymbol{\nabla} P^\pm = 0, \tag{4.1}$$

$$\eta_2 \bar{\nabla}^2 \boldsymbol{v} - \bar{\boldsymbol{\nabla}} p + \boldsymbol{\sigma}^+ + \boldsymbol{\sigma}^- + \boldsymbol{f}\delta(\boldsymbol{r} - \boldsymbol{R}) = 0, \tag{4.2}$$

$$\dot{\boldsymbol{R}} = \boldsymbol{v}(\boldsymbol{R}), \tag{4.3}$$

where

$$\boldsymbol{\sigma}^\pm = \pm\eta^\pm \left(\partial_z \bar{\boldsymbol{V}}^\pm + \bar{\boldsymbol{\nabla}} V_z^\pm\right)\Big|_{z=0} \tag{4.4}$$

are the tangent viscous stresses transmitted to the membrane by the bulk flow. The first equation is the 3D Stokes equation describing the flow in the solvent, the second equation is the Stokes equation in the membrane, and the third equation is a no-slip condition on the pointlike particle reflecting its transport by the membrane flow. Note that since inertia is neglected, the force $\boldsymbol{f}$ applied to the particle is directly transmitted to

the 2D membrane fluid. Here, p and $P^\pm$ are the excess pressure fields (pressure minus the pressure at infinity), the dot denotes time derivative and the bar denotes the projection onto the (x,y) plane of 3D vectors ($\bar{\boldsymbol{\nabla}} = \boldsymbol{e}_x\partial_x + \boldsymbol{e}_y\partial_y$ and $\bar{\boldsymbol{V}} = V_x\boldsymbol{e}_x + V_y\boldsymbol{e}_y$). These equations are supplemented by the incompressibility conditions $\boldsymbol{\nabla}\cdot\boldsymbol{V}^\pm = 0$ and $\bar{\boldsymbol{\nabla}}\cdot\boldsymbol{v} = 0$, and by the no-slip and continuity conditions $\bar{\boldsymbol{V}}^\pm|_{z=0} = \boldsymbol{v}$ and $V_z^\pm|_{z=0} = 0$.

As we are dealing with a pointlike force, solving for the membrane flow is equivalent to determining the Oseen-like tensor in this geometry [73, 74]. We start by eliminating the bulk variables. For this, as detailed in 2.2.2, we Fourier transform in the (x,y) plane while keeping z in real space. We recall briefly the procedure and results. Let $\boldsymbol{V}^\pm(\boldsymbol{q},z) = \int \mathrm{d}^2r\, \boldsymbol{V}^\pm(\boldsymbol{r},z)e^{-i\boldsymbol{q}\cdot\boldsymbol{r}}$. We decompose it as $\boldsymbol{V}^\pm = V_\parallel^\pm\hat{\boldsymbol{q}} + V_\perp^\pm\hat{\boldsymbol{q}}_\perp + V_z^\pm\hat{\boldsymbol{e}}_z$, where $\hat{\boldsymbol{q}} = \boldsymbol{q}/q$ and $\hat{\boldsymbol{q}}_\perp = \hat{\boldsymbol{e}}_z\times\hat{\boldsymbol{q}}$, and likewise $\boldsymbol{v} = v_\parallel\hat{\boldsymbol{q}} + v_\perp\hat{\boldsymbol{q}}_\perp$. Incompressibility yields $v_\parallel(\boldsymbol{q}) = 0$. The bulk equations read $\eta^\pm(\partial_z^2 - q^2)(V_\parallel^\pm, V_\perp^\pm, V_z^\pm) = (iqP^\pm, 0, \partial_z P^\pm)$ and $\partial_z V_z^\pm + iqV_\parallel^\pm = 0$. Solving them with the boundary condition $\boldsymbol{V}^\pm(\boldsymbol{q},z)|_{z=0} = v_\perp(\boldsymbol{q})\hat{\boldsymbol{q}}_\perp$ yields $P^\pm(\boldsymbol{q},z) = 0$ and $\boldsymbol{V}^\pm(\boldsymbol{q},z) = v_\perp(\boldsymbol{q})\exp(\mp qz)\hat{\boldsymbol{q}}_\perp$. It follows that $\boldsymbol{\sigma}^\pm = -\eta^\pm q v_\perp(\boldsymbol{q})\hat{\boldsymbol{q}}_\perp$ [148], and the hydrodynamic equations in the membrane reduce simply to

$$-\eta_2 q^2 v_\perp - 2\eta q v_\perp + \boldsymbol{f}e^{-i\boldsymbol{q}\cdot\boldsymbol{R}}\cdot\hat{\boldsymbol{q}}_\perp = 0, \tag{4.5}$$

$$v_\parallel = 0, \tag{4.6}$$

where $2\eta = \eta^+ + \eta^-$. The solution for $\boldsymbol{v}(\boldsymbol{q})$ is then

$$\boldsymbol{v}(\boldsymbol{q}) = \boldsymbol{O}(\boldsymbol{q})\cdot\boldsymbol{f}e^{-i\boldsymbol{q}\cdot\boldsymbol{R}}, \quad \boldsymbol{O}(\boldsymbol{q}) = \frac{\mathbb{1} - \hat{\boldsymbol{q}}\otimes\hat{\boldsymbol{q}}}{2\eta q + \eta_2 q^2}, \tag{4.7}$$

with $\boldsymbol{O}$ the Oseen-like tensor in the SD geometry [73, 74]. Assuming then $\boldsymbol{f} = f\boldsymbol{e}_x$, we obtain the particle's velocity as

$$v_p = \boldsymbol{e}_x\cdot\boldsymbol{v}(\boldsymbol{R}) = \int \frac{q\,dq\,d\theta}{(2\pi)^2}\frac{(1-\hat{q}_x^2)f}{(\eta^+ + \eta^-)q + \eta_2 q^2}, \tag{4.8}$$

where $\hat{q}_x = \cos\theta$. However, due to its ultraviolet (high-q) behavior, this integral diverges logarithmically. Since the short-scale velocity gradients of $v(\boldsymbol{r})$ are located near $\boldsymbol{r} = \boldsymbol{R}$ while in reality, the particle has a uniform velocity field for $r < a$ (it is solid), we may resolve this problem by eliminating the Fourier modes with wavevectors larger than the inverse particle radius a^{-1} (see a similar approach in Appx. B of [146]). To simplify, we use a sharp cutoff $q_{\max} = a^{-1}$, and integrating over q in the range $[0, a^{-1}]$ yields

$$v_p = \frac{f}{4\pi\eta_2}\ln\left(1 + \frac{\ell}{a}\right), \tag{4.9}$$

with the SD length

$$\ell = \frac{\eta_2}{\eta^+ + \eta^-} \tag{4.10}$$

We shall discuss more precisely in Sec. 4.3.1 the validity conditions of our pointlike method. Let us simply note here that we need to assume $a \ll \ell$ otherwise, we would be neglecting the Fourier modes at the scale of the SD length, which are physically

important. The condition $a \ll \ell$ is also a condition of validity of the original SD law [70, 77, 137]. Note that it is very well satisfied for proteins in membranes since a lies in the nanometer range while ℓ lies in the micron range.

In this limit we thus obtain $v_p \simeq f(4\pi\eta_2)^{-1}\ln(\ell/a)$. Therefore the particle's mobility $\tilde{\mu} = v_p/f$ is given, within our approximation scheme, by

$$\tilde{\mu} = \frac{1}{4\pi\eta_2}\ln\frac{\ell}{a}. \tag{4.11}$$

This is the SD law, except for an extra factor of order unity multiplying the particle radius, namely $2/e^{\gamma} \simeq 1.1$. Because this factor is within the logarithm, the prefactor obtained here, i.e., $(4\pi\eta_2)^{-1}$, is exactly that of the SD law (contrary to the 3D case in which the radius appears in the Stokes power law). Numerically, with the typical parameters $a \simeq 3\,\mathrm{nm}$, $\eta^{\pm} \simeq 10^{-3}\,\mathrm{J\,s\,m^{-3}}$ and $\eta_2 \simeq 10^{-9}\,\mathrm{J\,s\,m^{-2}}$, we find that μ and $\tilde{\mu}$ differ only by 2%. Note that while it is formally important to have an exact result for a perfect disc (the SD law), real objects embedded in membranes, like integral proteins, are not perfect cylinders, but rather cylindrical-like or conical-like inclusions with an inhomogeneous radius, so that uncertainties on the radius are actually not so important.

4.3 Mobility in bilayer membranes

As seen in Chap. 1, a real membrane is not simply a 2D viscous slab, it is made up of two contacting fluid monolayers (labeled as $\pm$), each with its own 2D viscosity $\eta_2^{\pm}$. The question of the continuity, or discontinuity, of the lipids' velocity across the separation between the two monolayers, is important [148–150]. While it is legitimate to impose a no-slip boundary condition at the interface between each monolayer and its contacting solvent, and at the interface between an inclusion's boundary and its contacting monolayer, it is in general necessary to allow for some velocity discontinuity $\Delta\boldsymbol{v} = \boldsymbol{v}^+ - \boldsymbol{v}^-$ at the interface between the two monolayers [148]. Intermonolayer sliding occurs essentially because there is very little interdigitation of the lipids' tails at the interface between the two monolayers. The relevant parameter is the intermonolayer friction coefficient b, which plays the role of a discrete viscosity: the stress transmitted through the interface is $b\Delta\boldsymbol{v}$ [149], very much like the viscous stress $\eta\partial V_x/\partial z$ in a bulk fluid. The larger b, the more continuity is imposed, and the smaller b, the more sliding is allowed. In practice, for membranes, b has been reported over a wide range $10^6 - 10^9\,\mathrm{J\,s\,m^{-4}}$ [151, 152], so we shall leave open the possibility of intermonolayer sliding. Below, we consider two cases: either the protein is located in one monolayer, as peripheral proteins are, or it occupies the bilayer, like integral proteins.

4.3.1 Mobility of a protein in one monolayer

The diffusion behavior of solid particles embedded in a single monolayer of a bilayer membrane was studied numerically in [146], and discussed analytically in [153] for supported membranes using a phenomenological friction/slip description. The related

problem of the diffusion of liquid domains within a monolayer (thus involving lipid flow inside the domains) was discussed in [147].

We consider an inclusion embedded in the upper monolayer of a membrane, or simply adhering to it (Fig. 4.1b). The membrane is treated as a bilayer with monolayer viscosities $\eta_2^\pm$ and intermonolayer friction b, embedded in a bulk fluid with viscosities $\eta^\pm$. The force $\boldsymbol{f}^+$ applied to the particle is transmitted to the upper monolayer, so that the dynamical equations presented Sec. 2.2.2 become

$$\eta^\pm \nabla^2 \boldsymbol{V}^\pm - \boldsymbol{\nabla} P^\pm = 0, \tag{4.12}$$
$$\eta_2^+ \bar{\nabla}^2 \boldsymbol{v}^+ - \bar{\boldsymbol{\nabla}} p^+ + \boldsymbol{\sigma}^+ - b\Delta\boldsymbol{v} + \boldsymbol{f}^+ \delta(\boldsymbol{r} - \boldsymbol{R}) = 0, \tag{4.13}$$
$$\eta_2^- \bar{\nabla}^2 \boldsymbol{v}^- - \bar{\boldsymbol{\nabla}} p^- + \boldsymbol{\sigma}^- + b\Delta\boldsymbol{v} = 0, \tag{4.14}$$
$$\dot{\boldsymbol{R}} = \boldsymbol{v}^+(\boldsymbol{R}), \tag{4.15}$$

where $\Delta\boldsymbol{v} = \boldsymbol{v}^+ - \boldsymbol{v}^-$. These equations are supplemented by the following incompressibility and continuity equations: $\boldsymbol{\nabla}\cdot\boldsymbol{V}^\pm = 0$, $\bar{\boldsymbol{\nabla}}\cdot\boldsymbol{v}^\pm = 0$, $\bar{\boldsymbol{V}}^\pm|_{z=0} = \boldsymbol{v}^\pm$ and $V_z^\pm|_{z=0} = 0$. With respect to the previous problem, eq. (4.2) has been split into two equations (one for each monolayer), intermonolayer friction has been added, and the no-slip condition (4.15) expressing the transport of the particle involves now only the upper monolayer flow. Going to Fourier space and eliminating the bulk variables as previously yields the membrane equations:

$$-\eta_2^+ q^2 v_\perp^+ - \eta^+ q v_\perp^+ + b(v_\perp^- - v_\perp^+) + \boldsymbol{f}^+ \mathrm{e}^{-i\boldsymbol{q}\cdot\boldsymbol{R}}\cdot\hat{\boldsymbol{q}}_\perp = 0, \tag{4.16}$$
$$-\eta_2^- q^2 v_\perp^- - \eta^- q v_\perp^- + b(v_\perp^+ - v_\perp^-) = 0, \tag{4.17}$$
$$v_\parallel^\pm = 0. \tag{4.18}$$

Solving for the monolayer velocities, we obtain $\boldsymbol{v}^\pm(\boldsymbol{q}) = \mathbf{O}_+^\pm(\boldsymbol{q})\cdot\boldsymbol{f}^+\mathrm{e}^{-i\boldsymbol{q}\cdot\boldsymbol{R}}$, with

$$\boldsymbol{O}_+^\epsilon(\boldsymbol{q}) = A_+^\epsilon(q)\,(\mathbb{1} - \hat{\boldsymbol{q}}\otimes\hat{\boldsymbol{q}})\,, \tag{4.19}$$
$$A_+^\epsilon(q) = \frac{b + q(\eta^- + \eta_2^- q)\delta_{\epsilon,+}}{qD(q)}, \tag{4.20}$$

where

$$D(q) = b\left[\eta^+ + \eta^- + (\eta_2^+ + \eta_2^-)q\right] + q(\eta^+ + \eta_2^+ q)(\eta^- + \eta_2^- q) \tag{4.21}$$

The tensor $\mathbf{O}_-^\pm$ giving the velocities for a pointlike force $\boldsymbol{f}^-$ applied to the lower monolayer is obtained by exchanging the $+$ and $-$ signs. These Oseen-like tensors were first derived in [146].

In order to calculate, within our regularized pointlike approximation, the mobility $\tilde{\mu}_m$ of a particle embedded in the upper monolayer, we take $\boldsymbol{f}^+ = f^+\boldsymbol{e}_x$, which yields the particle velocity $v_p = \boldsymbol{e}_x\cdot\boldsymbol{v}^+(\boldsymbol{R}) = \tilde{\mu}_m f^+$, with

$$\tilde{\mu}_m = \int_0^{a^{-1}} \frac{q\,dq\,d\theta}{(2\pi)^2}\, A_+^+(q)\sin^2\theta. \tag{4.22}$$

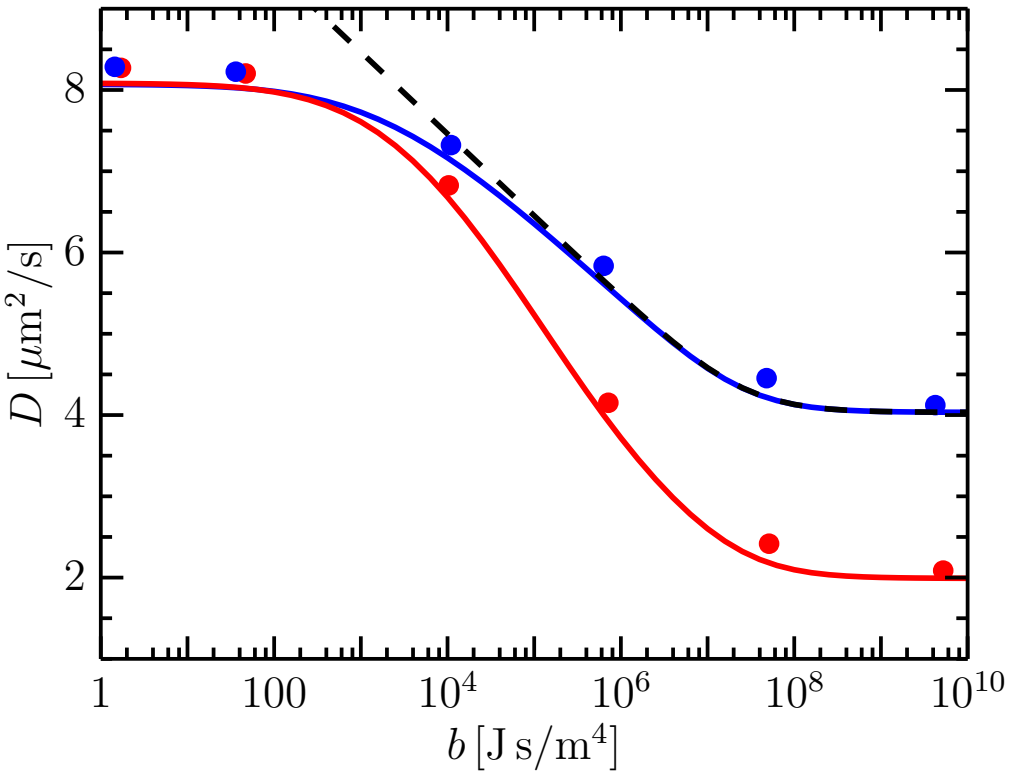

Figure 4.2 – Diffusion coefficient $D = k_{\kappa_\mathrm{p}} T \tilde{\mu}_m$, as a function of the intermonolayer friction b, for a protein in the upper monolayer of a membrane (i) in an infinite solvent, i.e., $H = \infty$ (blue line) and (ii) in a supported membrane at a distance H from a substrate (red line). Dashed black line: approximation $D \simeq k_{\kappa_\mathrm{p}} T \tilde{\mu}_m^{(1)}$, valid for large b in an infinite solvent. The parameters are identical to those of Camley and Brown in [146], Fig. 7, i.e., $T = 319\,\mathrm{K}$, $\eta^\pm = 10^{-3}\,\mathrm{J\,s\,m^{-3}}$, $\eta_2^\pm = 2 \times 10^{-10}\,\mathrm{J\,s\,m^{-2}}$, $a = 2\,\mathrm{nm}$ and $H = 1\,\mathrm{nm}$. The red and blue data points were extracted from the Fig. 7 of [146]. Our theory fits well the numerical data with no adjustable parameter.

As previously, we have regularized the integral by using an upper wavevector cutoff equal to the inverse of the particle's radius.

We first consider the symmetric situation where $\eta^+ = \eta^- = \eta^\pm$ and $\eta_2^+ = \eta_2^- = \eta_2^\pm$. In this case, the solution is analytic, given exactly by

$$\tilde{\mu}_m = \frac{1}{8\pi\eta_2^\pm} \ln\left[\left(1 + \frac{\eta_2^\pm}{\eta^\pm a}\right)\sqrt{1 + \frac{\eta_2^\pm + \eta^\pm a}{2a^2 b}}\,\right] + \frac{\eta \ln\left(\frac{4ab+\eta^\pm - \sqrt{\eta^{\pm 2} - 8b\eta_2^\pm}}{4ab+\eta^\pm + \sqrt{\eta^{\pm 2} - 8b\eta_2^\pm}}\right)}{16\pi\eta_2^\pm \sqrt{\eta^{\pm 2} - 8b\eta_2^\pm}}. \tag{4.23}$$

Assuming $a \ll \ell = \eta_2^\pm/\eta^\pm$ as in the previous section, the first term $\tilde{\mu}^{(1)}$ of $\tilde{\mu}$, which is also the term dominant at large b, can be simplified into

$$\tilde{\mu}_m^{(1)} \simeq \frac{1}{8\pi\eta_2^\pm} \ln\left(\frac{\ell}{a}\sqrt{1 + \frac{\eta_2^\pm}{2a^2 b}}\right). \tag{4.24}$$

The mobility is related to the diffusion coefficient by Einstein's relation $D = k_\mathrm{B} T \tilde{\mu}_m$.

The blue curve of Fig. 4.2 shows D versus the intermonolayer friction b for infinite solvents, as obtained from eq. (4.23). We see that $\tilde{\mu}_m \simeq \tilde{\mu}_m^{(1)}$ for large b, as evidenced by the black dashed line in Fig. 4.2. Since the usual physical range of b for lipid membranes lies in this region, we infer that in practice

$$\tilde{\mu}_m \simeq \tilde{\mu}_m^{(1)}. \tag{4.25}$$

This formula is typically valid for b larger than $10^5\,\mathrm{J\,s\,m^{-4}}$.

We deduce that the SD law is influenced by b when $b < \eta_2^{\pm}/(2a^2)$. The limit $b \to \infty$ gives exactly the SD law. Indeed, $\tilde{\mu}_m \to \tilde{\mu}$ with η_2 replaced by $2\eta_2^{\pm}$. This comes from the fact that both monolayers are fully dragged by the applied force. The limit $b \to 0$ gives $\tilde{\mu}_m \to 2\tilde{\mu}$, as apparent in Fig. 4.2, a result already pointed out in Refs. [146, 147]. This stems from the fact that only the monolayer containing the inclusion is dragged by the force. These behaviors are easily deduced from the form of $\mathbf{O}_+^+(q)$, which converges to $\mathbf{O}(q)$ with $\eta_2 = 2\eta_2^{\pm}$ when $b \to \infty$ and to $\mathbf{O}(q)$ with $\eta_2 = \eta_2^{\pm}$ when $b \to 0$.

In Fig. 4.2, we plotted together with our analytical curves several data points extracted from the numerical calculations of Camley and Brown [146] who addressed the same problem. Note the fair agreement, with no adjustable parameter. The presence of a substrate at a distance H below the membrane can be taken into account very simply within our model by replacing η^- by $\eta^- \coth(qH)$ in the Oseen-like tensor (4.19) [73, 74]. Then the numerical integral (4.22) gives the red curve in Fig. 4.2 which displays also a fair agreement with the numerical results of [146].

In the general asymmetric situation, such that $\eta^+ \neq \eta^-$ or $\eta_2^+ \neq \eta_2^-$, the integral (4.22) giving $\tilde{\mu}_m$ must be done numerically, because the roots of $D(q)$ are complicated. It is possible, however, to get analytical results in the following two situations:

(i) For $b \to \infty$, $\mathbf{O}_+^+(q) \to \mathbf{O}(q)$ with η_2 replaced by $\eta_2^+ + \eta_2^-$. Therefore the mobility $\tilde{\mu}_m$ tends to $\tilde{\mu}_\infty$ with

$$\tilde{\mu}_\infty = \frac{1}{4\pi(\eta_2^+ + \eta_2^-)} \ln \frac{\eta_2^+ + \eta_2^-}{(\eta^+ + \eta^-)a}. \tag{4.26}$$

We recover the SD law. Everything happens as if the particle were embedded in a single layer with a 2D viscosity equal to the sum of those of the monolayers (recall that the 2D viscosity of a thin layer is proportional to its thickness). For ordinary values of the viscosities, i.e., $\eta^{\pm} \simeq 10^{-3}\,\mathrm{J\,s\,m^{-3}}$ and $\eta_2^{\pm} \simeq 10^{-9}\,\mathrm{J\,s\,m^{-2}}$, $\tilde{\mu}_m$ is well approximated by $\tilde{\mu}_\infty$ as soon as $b \gtrsim 10^8\,\mathrm{J\,s\,m^{-4}}$ (like in Fig. 4.2).

(ii) In the somewhat formal proportional case $\eta^-/\eta^+ = \eta_2^-/\eta_2^+ = \alpha$, we obtain analytically the following generalization of eq. (4.24):

$$\tilde{\mu}_m \simeq \frac{1}{4\pi(1+\alpha)\eta_2^+} \ln \left[\frac{\ell}{a} \left(1 + \frac{2\alpha}{1+\alpha} \frac{\eta_2^+}{2a^2 b} \right)^{\alpha/2} \right], \tag{4.27}$$

valid also typically for $b \gtrsim 10^5\,\mathrm{J\,s\,m^{-4}}$, like in Fig. 4.2.

Let us now discuss in more detail the conditions of validity of our pointlike approximation. We do eliminate all the Fourier modes with wavevectors larger than the inverse particle radius a^{-1}. Obviously, we must not eliminate modes having a physical meaning

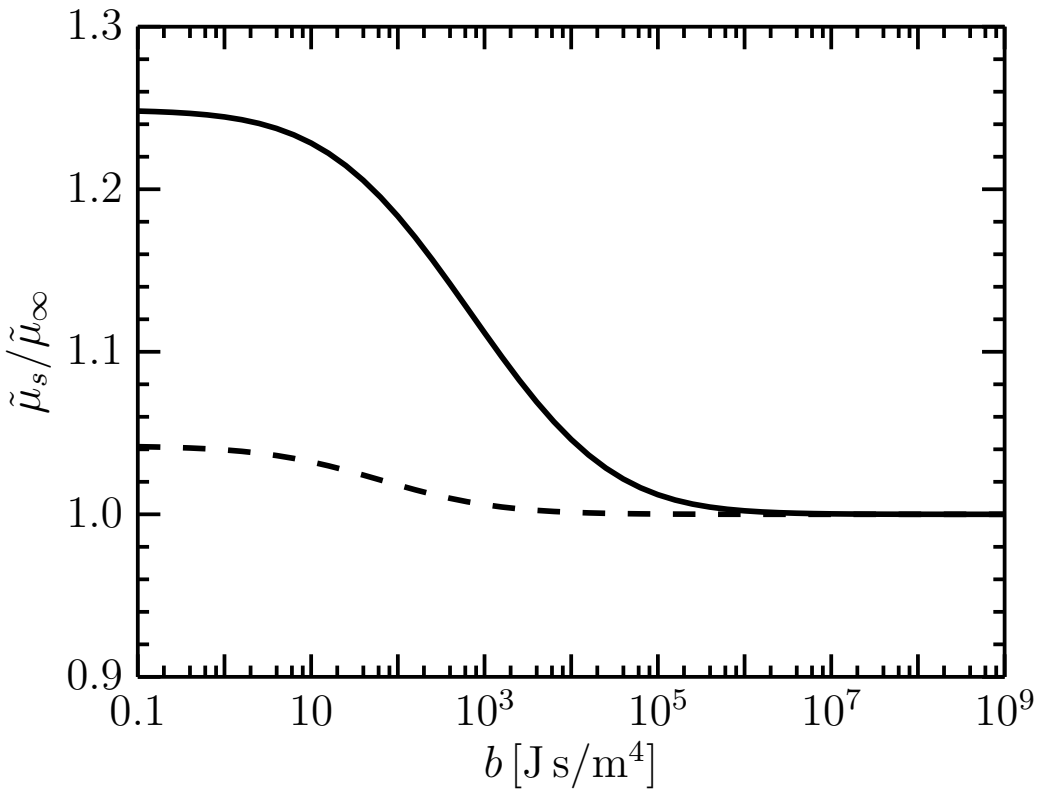

Figure 4.3 – Mobility $\tilde{\mu}_s$ of a particle with radius $a = 3\,\mathrm{nm}$ spanning an asymmetric bilayer as a function of the intermonolayer friction b, normalized by its limit $\tilde{\mu}_\infty$ for $b \to \infty$. The viscosities are $\eta^- = 10\eta^+ = 10^{-2}\,\mathrm{J\,s\,m^{-3}}$, $\eta_2^+ = 10\eta_2^- = 10^{-8}\,\mathrm{J\,s\,m^{-2}}$ (solid curve) and $\eta^+ = \eta^- = 10^{-3}\,\mathrm{J\,s\,m^{-3}}$, $\eta_2^+ = 10\eta_2^- = 10^{-8}\,\mathrm{J\,s\,m^{-2}}$ (dashed curve).

(stemming from relevant characteristic lengths) and contributing significantly to the integral of the Oseen-like tensor. First, let us note that this will never significantly be the case for transmembrane proteins because a is in the nanometer range and Fourier modes with smaller wavelengths are unphysical (they are of the order of the membrane thickness or of several lipid widths). In other words, there is already an implicit cutoff in the nanometer range in the system. So, whatever the characteristic lengths involved in the Oseen-like tensor, our approximate method can be safely applied to membrane proteins. Now, if we were to apply our method to somewhat larger particles, e.g., liquid domains, it would be necessary to investigate whether the integral of the modes between a^{-1} and the inverse nanometer range contribute negligibly to the total integral or not. For instance, our method would fail for solid particles larger than the SD length since it would yield a mobility different from that calculated by Hughes et al. [137] who generalized the mobility for proteins with size above the SD length.

4.3.2 Mobility of a protein spanning the bilayer

We now apply our method in order to calculate the mobility $\tilde{\mu}_s$ of an inclusion spanning the whole membrane, while taking into account the bilayer structure of the latter. The force $\boldsymbol{f}$ applied to the inclusion is now transmitted to both monolayers in the form of

two pointlike forces $\boldsymbol{f}^{\pm}$. If $\eta_2^+ \neq \eta_2^-$ (or $\eta^+ \neq \eta^-$) we expect, by lack of symmetry, these forces to be different. They are determined by the conservation of the total force and by the no-slip boundary condition at the surface of the particle:

$$\boldsymbol{f}^+ + \boldsymbol{f}^- = \boldsymbol{f}, \tag{4.28}$$

$$\boldsymbol{v}^+(\boldsymbol{R}) = \boldsymbol{v}^-(\boldsymbol{R}) = \dot{\boldsymbol{R}}. \tag{4.29}$$

Using eq. (4.19) and the linearity of the problem, we get

$$\begin{aligned} \boldsymbol{v}^{\pm}(\boldsymbol{q}) &= (O_+^{\pm} \cdot \boldsymbol{f}^+ + O_-^{\pm} \cdot \boldsymbol{f}^-)\mathrm{e}^{-i\boldsymbol{q}\cdot\boldsymbol{R}} \\ &= \frac{\mathbb{1} - \hat{\boldsymbol{q}} \otimes \hat{\boldsymbol{q}}}{qD(q)} \cdot \left[b\boldsymbol{f} + q(\eta^{\mp} + \eta_2^{\mp} q)\boldsymbol{f}^{\pm}\right] \mathrm{e}^{-i\boldsymbol{q}\cdot\boldsymbol{R}}. \end{aligned} \tag{4.30}$$

Using our regularized pointlike approximation, we obtain $\boldsymbol{v}^{\pm}(\boldsymbol{R}) = bI_0\boldsymbol{f} + (\eta^{\mp} I_1 + \eta_2^{\mp} I_2)\boldsymbol{f}^{\pm}$, with

$$I_n = \int_0^{a^{-1}} \mathrm{d}q \, \frac{q^n}{4\pi D(q)}. \tag{4.31}$$

Solving then eqs. (4.28)–(4.29) gives

$$\boldsymbol{f}^{\pm} = \frac{\eta^{\pm} I_1 + \eta_2^{\pm} I_2}{(\eta^+ + \eta^-)I_1 + (\eta_2^+ + \eta_2^-)I_2}\boldsymbol{f}, \tag{4.32}$$

and then $\boldsymbol{v}_p = \tilde{\mu}_s \boldsymbol{f}$, with

$$\tilde{\mu}_s = bI_0 + \frac{(\eta^- I_1 + \eta_2^- I_2)(\eta^+ I_1 + \eta_2^+ I_2)}{(\eta^+ + \eta^-)I_1 + (\eta_2^+ + \eta_2^-)I_2}. \tag{4.33}$$

Note that in the completely symmetric case $\eta^+ = \eta^- = \eta$ and $\eta_2^+ = \eta_2^- = \frac{1}{2}\eta_2$ the dependence in b disappears and $\tilde{\mu}_s$ reduces to $\tilde{\mu}$. The mobility $\tilde{\mu}_s$ must be studied numerically because I_n has no simple analytical form. We find that $\tilde{\mu}_s$ increases slightly as b decreases, in a way that is enhanced by the asymmetry of the viscosities (fig. 4.3). However, this effect is actually rather negligible, since for ordinary viscosities (as in Fig. 4.3) it requires $b \lesssim 10^4\,\mathrm{J\,s\,m^{-4}}$, well below any experimental value. We may therefore take the limit $b \to \infty$, which yields $D(q) \simeq b[\eta^+ + \eta^- + (\eta_2^+ + \eta_2^-)q]$, $I_n \propto 1/b$, and thus

$$\tilde{\mu}_s \simeq bI_0 \to \tilde{\mu}_\infty. \tag{4.34}$$

We recover again the SD law with η_2 replaced by $\eta_2^+ + \eta_2^-$. Physically, intermonolayer friction can be disregarded for particles spanning the bilayer, because monolayer slippage nearby the particle is forbidden by the no-slip conditions (4.28)–(4.29) at the particle's boundary.

4.4 Mobility of a curvature-inducing protein

Let us finally apply our method to membrane inclusions that curve the membrane. Such particles are usually either transmembrane proteins with a conical shape that bind the surrounding lipids, thus imposing a local curvature of the membrane [55, 154, 155], or non-flat capping proteins adhering to the membrane [156], with the same result (see Sec. 1.3). Experiments have been made also with larger adhering beads [157].

We will confine ourselves to weakly deformed membranes, described by their elevation $z = h(\boldsymbol{r})$ above the reference plane $\boldsymbol{r} = (x, y)$. The elastic energy of the system consisting of the membrane and the inclusion can be expressed as

$$\mathcal{H} = \int d^2r \left[\frac{\kappa}{2}(\nabla^2 h)^2 + \frac{\sigma}{2}(\boldsymbol{\nabla} h)^2 + \bar{\kappa}_p\, G(\boldsymbol{r} - \boldsymbol{R})\nabla^2 h\right]. \tag{4.35}$$

The first two terms correspond to the Helfrich Hamiltonian and describe the bending energy of the membrane and the energy associated with its tension σ [57]. The third term models an isotropic inclusion located at the in-plane position $\boldsymbol{R}$ that promotes membrane curvature with strength $\bar{\kappa}_p$, in the way of [43]. Here that we rely on a simple linear membrane-protein coupling to keep the calculations as simple as possible. Note that, with respect to the linear coupling expression 2.16, the rigidity $\bar{\kappa}_p$ contains the favored curvature c_0, *i.e.*, $\bar{\kappa}_p \sim \kappa_p c_0$. The function $G(r)$ is a generic function describing the envelope of the protein influence over the membrane, e.g., a Gaussian with a width comparable to the protein's radius [43, 68]. Note that in this model the actual curvature set by the inclusion depends on the elastic response of the membrane.

Assuming that the flow within the membrane remains quasi-2D, which is standard in the limit of small deformations [148, 158], and disregarding the membrane bilayer structure for the sake of simplicity, the dynamical equations of the system presented Sec. 2.2.2 can be written as

$$\eta^{\pm}\nabla^2 \boldsymbol{V}^{\pm} - \boldsymbol{\nabla} P^{\pm} = 0, \tag{4.36}$$

$$\eta_2 \bar{\nabla}^2 \boldsymbol{v} - \bar{\boldsymbol{\nabla}} p + \boldsymbol{\sigma}^{+} + \boldsymbol{\sigma}^{-} + \left(\boldsymbol{f} - \frac{\partial \mathcal{H}}{\partial \boldsymbol{R}}\right)\delta(\boldsymbol{r} - R) = 0, \tag{4.37}$$

$$-\frac{\delta \mathcal{H}}{\delta h} + \Sigma^{+} + \Sigma^{-} = 0, \tag{4.38}$$

$$\dot{\boldsymbol{R}} = \boldsymbol{v}(\boldsymbol{R}). \tag{4.39}$$

where

$$\Sigma^{\pm} = \pm(2\eta^{\pm}\partial_z V_z^{\pm} - P^{\pm})|_{z=0}. \tag{4.40}$$

The first equation is the bulk Stokes equation. The second equation is the Stokes equation for the membrane planar flow, including the force density transmitted by the particle. The third equation is the balance of the stresses normal to the membrane, with $\Sigma^{\pm}$ the stresses transmitted by the bulk. The last equation is the no-slip condition expressing the transport of the particle. These equations must be supplemented by the incompressibility relations $\boldsymbol{\nabla} \cdot \boldsymbol{V}^{\pm} = 0$ and $\bar{\boldsymbol{\nabla}} \cdot \boldsymbol{v} = 0$, and by the continuity conditions $\bar{\boldsymbol{V}}^{\pm}|_{z=0} = \boldsymbol{v}$ and

$V_z^{\pm}|_{z=0} = \dot{h}$.

Let us now express them in mixed reciprocal-direct space, as in Sec. 4.2, so as to eliminate the bulk velocities [148]. The boundary conditions read $V_z^{\pm}(\boldsymbol{q}, z)|_{z=0} = \dot{h}(q)$ and $\bar{\boldsymbol{V}}^{\pm}(\boldsymbol{q}, z)|_{z=0} = \boldsymbol{v}(\boldsymbol{q}) = v_{\perp}(\boldsymbol{q})\hat{\boldsymbol{q}}_{\perp}$. The bulk Stokes equations (see Sec. 4.2) give $P^{\pm} = \pm 2\eta^{\pm} q\dot{h}(\boldsymbol{q}) \exp(\mp qz)$, $V_{\parallel}^{\pm} = -iqz\dot{h}(\boldsymbol{q}) \exp(\mp qz)$, $V_{\perp}^{\pm} = v_{\perp}(\boldsymbol{q}) \exp(\mp qz)$ and $V_z^{\pm} = (1 \pm qz)\dot{h}(\boldsymbol{q}) \exp(\mp qz)$. One can thus calculate the stresses transmitted by the bulk onto the membrane: $\boldsymbol{\sigma}^{\pm} = -\eta^{\pm} q v_{\perp} \hat{\boldsymbol{q}}_{\perp}$ and $\Sigma^{\pm} = -2\eta^{\pm} q\dot{h}$. The dynamical equations of the membrane, i.e., Eqs. (4.37)-(4.38), read then in Fourier space

$$(2\eta q + \eta_2 q^2) v_{\perp}(\boldsymbol{q}) = \boldsymbol{f}' e^{-i\boldsymbol{q}\cdot\boldsymbol{R}} \cdot \hat{\boldsymbol{q}}_{\perp}, \tag{4.41}$$

$$v_{\parallel}(\boldsymbol{q}) = 0, \tag{4.42}$$

$$4\eta q\dot{h}(\boldsymbol{q}) = -(\kappa q^4 + \sigma q^2) h(\boldsymbol{q}) + \kappa_p q^2 G(q) e^{-i\boldsymbol{q}\cdot\boldsymbol{R}}, \tag{4.43}$$

where $2\eta = \eta^+ + \eta^-$, and where

$$\boldsymbol{f}' = \boldsymbol{f} - \kappa_p \int \mathrm{d}^2 r \, G(\boldsymbol{r} - \boldsymbol{R}) \boldsymbol{\nabla} \nabla^2 h \tag{4.44}$$

is the applied force reduced by the pull-back due to the membrane-inclusion coupling. The last equation, Eq. (4.43), determines the deformation of the membrane produced by the dragged inclusion.

Let us consider a steady state with $\dot{\boldsymbol{R}} = v_p \boldsymbol{e}_x$, where v_p is the constant particle's velocity and $\boldsymbol{e}_x$ is the direction in which the force is applied, as in Refs. [43, 159]. In the coordinate system comoving with the inclusion, we have $\boldsymbol{R} = \boldsymbol{0}$ and and $\dot{h}(\boldsymbol{r})$ becomes $-v_p \partial_x h(\boldsymbol{r})$, so that Eq. (4.43) gives

$$h(\boldsymbol{q}) = \frac{\kappa_p G(q)}{\kappa q^2 + \sigma} \left(1 + \frac{4i\eta q_x v_p}{\kappa q^3 + \sigma q} \right) + \mathcal{O}(v_p^2). \tag{4.45}$$

The effective force applied to the protein is then given by eq. (4.44), yielding, at linear order in the velocity, $f' = f - \gamma v_p$, with

$$\gamma = 2\eta \kappa_p^2 \int_{\boldsymbol{q}} \frac{q^3 G(q)^2}{(\kappa q^2 + \sigma)^2}, \tag{4.46}$$

where $\int_{\boldsymbol{q}} = (2\pi)^{-2} \int_0^{\Lambda} \mathrm{d}^2 q$, with an upper wavevector cutoff $k_{\max} = \Lambda$ of the order of the inverse membrane thickness. Injecting $\boldsymbol{f}'$ in Eqs. (4.41) and (4.42) yields $\boldsymbol{v}(\boldsymbol{q}) = \mathbf{O}(\boldsymbol{q}) \cdot \boldsymbol{f}'$, where $\mathbf{O}$ is the Oseen-like tensor (4.7) of the SD problem. Proceeding like in Sec. 4.2, we thus obtain $v_p = \tilde{\mu}(f - \gamma v_p)$, where $\tilde{\mu}$ is the SD mobility (4.11). Hence, $f = (\tilde{\mu}^{-1} + \gamma) v_p$, so that the mobility $\tilde{\mu}_c$ for an inclusion curving the membrane is given by

$$\frac{1}{\tilde{\mu}_c} = \frac{1}{\tilde{\mu}} + \gamma. \tag{4.47}$$

This implies, thanks to the Einstein relation, that the effective diffusion coefficient $D_{\mathrm{eff}} =$

$k_{\mathrm{B}}T\tilde{\mu}_c$ is given in terms of the bare diffusion coefficient $D_0 = k_{\mathrm{B}}T\tilde{\mu}$ by

$$D_{\mathrm{eff}} = D_0 \left(1 + \frac{D_0\gamma}{k_{\mathrm{B}}T}\right)^{-1}. \tag{4.48}$$

The extra friction γ comes from the mechanism introduced in [159], which is the following. At rest, the inclusion sits in equilibrium at the top of the bump it creates. The pulling deforms the bump in such a way that the inclusion does not sit any longer at the minimum energy position: there is therefore a force that pulls it back; this force, the second term of Eq. (4.44), is responsible for the extra drag. The work produced by this drag is dissipated by the dynamics of the membrane deformation within the surrounding solvent. Indeed, as shown in [68], this dynamics produces precisely the dissipation (4.46).

4.5 Analysis of the results of Quemeneur et al.

By comparing the diffusion coefficients of AQP0 proteins that do not deform the membrane with KvAP proteins that induce a local curvature C_0 to the membrane, S. Aimon and coworkers [42] highlight the curvature sensing of KvAP proteins. In a later work, Quemeneur and coworkers [43] observe KvAP proteins mobility exhibits a tension dependence: in the high tension regime, the diffusion coefficients of AQP0 (blue points in Fig. 4.4) and KvAP (red points in Fig, 4.4) are similar and correspond to the expected value predicted by the SD model. However, when the tension decreases, while the AQP0 diffusion coefficient remains unchanged, KvAP drops as low as half the SD diffusion. Investigating this effect using a linear coupling between the membrane height and the proteins, Quemeneur et al. [43] find a diffusion coefficient that coincides with the one derived above (4.48), with the correspondence $\kappa_p = \frac{1}{2}\kappa\Theta$ and $\Lambda = 2\pi/a$. However they postulate that the total friction is the sum of the usual SD friction and the extra friction coming from the membrane deformation. With our approach, we are able to derive this total friction from first principles.

As shown in Fig. 4.4, a linear membrane-protein coupling is able to fit the diffusion coefficient of KvAP proteins [43]. To get this fit, A delta function for $G(\boldsymbol{r})$ is assumed and the parameters taken are $a = 5\,\mathrm{nm}$, $\eta = 10^{-3}\,\mathrm{Jsm}^{-3}$, $\eta_2 = 6 \times 10^{-10}\,\mathrm{Jsm}^{-2}$, $\kappa = 20\ k_{\mathrm{B}}T$ and $\kappa_p \simeq 1.4 \times 10^{-17}\,\mathrm{Jnm}$. These values gives a coupling strength comparable to the bending strength and corresponds to a spontaneous curvature $C_0 \simeq 1\,\mathrm{nm}^{-1}$, which is 25 times bigger than the actual curvature (for KvAP, $C_0 \simeq 0.04\,\mathrm{nm}^{-1}$, see Chap. 1). It is therefore unlikely that the linear coupling alone can explain the behavior of KvAP proteins

Authors of [60] and [160] state that "a completely rigid conical protein (otherwise resembling KvAP) will never diffuse like a cylindrical one, such as AQP0" and so propose a mechanism where the protein shape depends on the membrane tension.

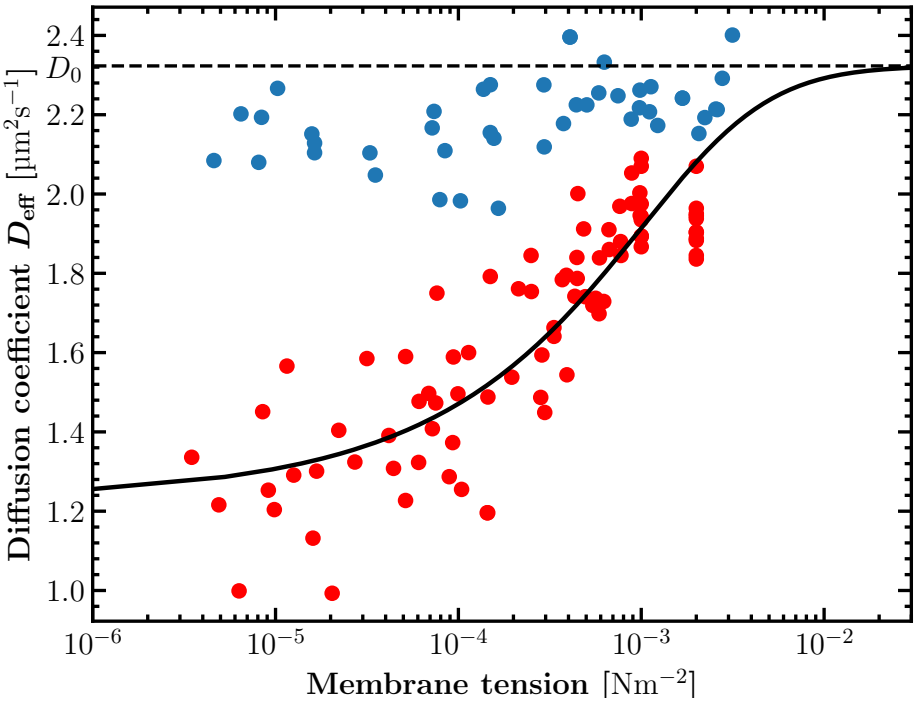

Figure 4.4 – Semilogarithmic plot of the diffusion coefficient D_{eff} as a function of the membrane tension for AQP0 (blue points) and KvAP (red points) proteins. the dashed line indicates the value of the SD diffusion coefficient determined with Eq. (4.11). The points are experimental data scraped from [43]. The thick black line corresponds to a fit of the KvAP diffusion coefficient performed in a similar fashion of [43]. The parameters are given in the main text.

4.6 Discussion

We have shown that an excellent analytical approximation to SD law can be obtained very simply from the SD "Stokeslet" (the Oseen-like tensor of the SD problem) evaluated at the origin, upon regularizing it with an upper wavevector cutoff of the order of the inverse of the particle size a. Using this method, we have investigated the consequences of the bilayer structure of the membrane (and of its asymmetry) and the role of the intermonolayer friction coefficient b. We have also investigated the consequences of the deformation (bump) caused by a curvature-inducing particle.

In the case of an inclusion embedded in only one of the two monolayers, or simply adhering to one of them, we found that for large values of b the SD law holds upon replacing the 2D viscosity η_2 of the membrane by the sum of the 2D viscosities of the monolayers. Indeed, b can be neglected when it is large, as it effectively sets a no-slip boundary condition between the two monolayers (they then act as an effective medium of viscosity $\eta_2 = \eta_2^+ + \eta_2^-$). This breaks down when b is smaller than $\eta_2/(4a^2)$, in which case the mobility gets larger since the monolayer opposite to the inclusion is not fully dragged by the inclusion around the latter.

In the case of an inclusion spanning the whole bilayer, we found that for all practical values of b, the rule of replacing the 2D viscosity of the membrane by the sum of the monolayer viscosities holds. This is because the no-slip boundary condition between the inclusion and each of the two monolayers effectively imposes a no-slip condition between the monolayers around the inclusion.

Finally, for curvature-inducing inclusions, we showed (in the small deformation regime) that the total friction is the sum of the SD friction and that due to the pull-back caused by the velocity-induced deformation of the bump. It would be interesting to investigate whether this remains true in a more general model involving a quadratic membrane-inclusion coupling.

Chapter 5

Collective behavior of curvature-inducing proteins with hydrodynamic couplings

The goal of this chapter is to study the diffusion of an assembly of proteins. By taking into account the hydrodynamic couplings between proteins, the authors of [161] have found the emergence of collective motion. First, we focus on the diffusion of an assembly of proteins in a membrane held flat, where our numerical simulations allow us to confirm the validity of the approximations made in [161] to predict the long-time evolution of the diffusion coefficient. We then go further by taking the thermal fluctuations of the membrane into account, and by assuming curvature-inducing proteins to study the effect of membrane deformations on the assembly's diffusion.

5.1 Introduction

In the previous chapter, we considered a pointlike protein linearly coupled to a membrane at thermal equilibrium and we studied its diffusion when it induces a curvature of the membrane. Of course, in the literature, we can find more refined models; the protein size is considered, the membrane-protein coupling is quadratic and the membrane deformation is taken into account, as well as thermal fluctuations [65–68]. An interesting result these articles highlight about this more realistic model is the reduction of the diffusion of a curvature-inducing protein relative to the "flat" protein case (the initial problem considered by Saffman and Delbrück [70]). As stated in [66], this reduction comes from the negative correlations $\langle \boldsymbol{\xi}(t) \cdot \boldsymbol{f}(t') \rangle$ where $\boldsymbol{\xi}(t)$ is the stochastic force applied on the protein at time t and $\boldsymbol{f}(t')$ the force the membrane applies on the protein at time $t' > t$. These correlations stand for the membrane reaction to the stochastic force exerted on the protein and is similar to the mechanism presented in Sec. 4.4 and [159]: when the random force moves the protein during a small discrete time step, the latter, via its interaction with the membrane, will change the shape of the membrane so that the energy of the

system tends towards the minimum. However, this minimum energy cannot be reached in such a short time, therefore, the membrane pulls the protein back to its initial position through the force $\boldsymbol{f}(t')$, leading to overall negative correlations. Note that it is essential to consider the membrane's reaction to the protein's displacement, *i.e.*, to consider the deformation force the protein exerts on the membrane. Otherwise, these correlations would not exist as the membrane shape would evolve independently from the protein's position, leading to a diffusion coefficient greater than the one of a "flat" protein [65–67].

When there are $N > 1$ proteins, they do not move independently due to interprotein forces mediated by the membrane and the fluid [80, 161, 162]. In [161], the authors use both theoretical and numerical Brownian dynamics simulations to highlight the effects of the hydrodynamic correlations on the diffusion of an assembly of proteins (see Fig. 5.1). Since the membrane is a viscous fluid, it generates hydrodynamic correlations between proteins [80, 161] affecting the diffusion of the ensemble. Besides the self-diffusion coefficient of an isolated protein, D_0, to study the diffusion of the assembly of proteins, one has therefore to consider also the diffusion coefficient of both the center of mass of the assembly, D_{CM}, and of the growth of the gyration radius, $D_{\mathrm{g}} = D_0 - D_{\mathrm{CM}}$ [161], where this radius is the characteristic radius of the assembly defined by $R_g^2 = N^{-1}\sum_i(\boldsymbol{r}_i - \boldsymbol{R}_{\mathrm{CM}})^2$, with $\boldsymbol{r}_i$ the position of the ith protein. The ratio of these diffusion coefficients impacts the collective diffusion of the assembly; when D_{CM} is greater than D_{g}, then the hydrodynamic couplings are strong enough to generate a collective motion between the proteins where the diffusion of the assembly's center of mass behaves like the diffusion of the rigid protein disk with a characteristic radius the radius of the assembly [161]; in the opposite case, the proteins' assembly disperses more than it diffuses collectively so that the effect of the hydrodynamic couplings over the motion of each protein becomes negligible [161]. Furthermore, the diffusion coefficients are time-dependent; in the initial time for a dense assembly, the collective effects are strong, then, as time goes by, proteins move away from each other, weakening the collective effects and the regime becomes more dispersive [161].

In addition to the hydrodynamic couplings, there are mediated interactions between curvature-inducing proteins [55, 103] that have not been taken into account to study the diffusion of a protein's assembly in the literature yet. When proteins induce a curvature of the membrane, the latter is deformed and, in return, generates elastic forces between proteins. Let us consider two pointlike curvature-inducing proteins embedded in a membrane. By assuming that the spontaneous curvatures C_1 and C_2 are imposed as local constraints on the membrane, one can determine the elastic interaction through the partition function of the system [103] and, as in Chap. 4, by using a cutoff of the order the size of the proteins. Fig. 5.2 shows the typical behavior of the elastic interaction between two proteins for different curvatures: when the curvatures have the same sign, the interprotein interaction is always repulsive; in the case of curvatures of opposite sign [19], at a distance shorter than a length of the order the characteristic length $\xi = \sqrt{\kappa/\sigma}$, the interaction is repulsive and, at larger distances, it becomes attractive. It is worth mentioning that in the case of a tensionless membrane ($\sigma = 0$), the elastic interaction is always repulsive [110]

In the first section, we will present the modelization and the numerical methods we use to study the collective behavior of an assembly of proteins. We then use simulations to

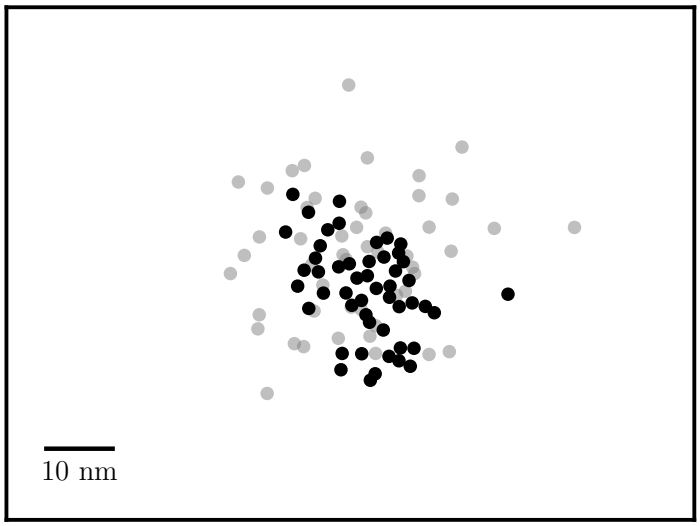

Figure 5.1 – Numerical simulation snapshot of an assembly of $N = 50$ proteins at time $t = 20\,\mu s$ with and without hydrodynamic correlations. The gray and black circles correspond to the positions of the proteins of radius $a_p = 0.5\,nm$ without and with hydrodynamic coupling, respectively. The dispersion of the assembly highlight the emergence of a collective behavior between proteins when the hydrodynamic couplings are taken into account. The parameters of the simulation are the membrane fluid viscosity $\eta_2 = 10^{-9}\,Jsm^{-2}$, the initial assembly's radius $R_0 = 10\,nm$, the time step of the evolution $\tau = 1\,ns$. The simulation reproduced the results of [161] and is performed with the method described below.

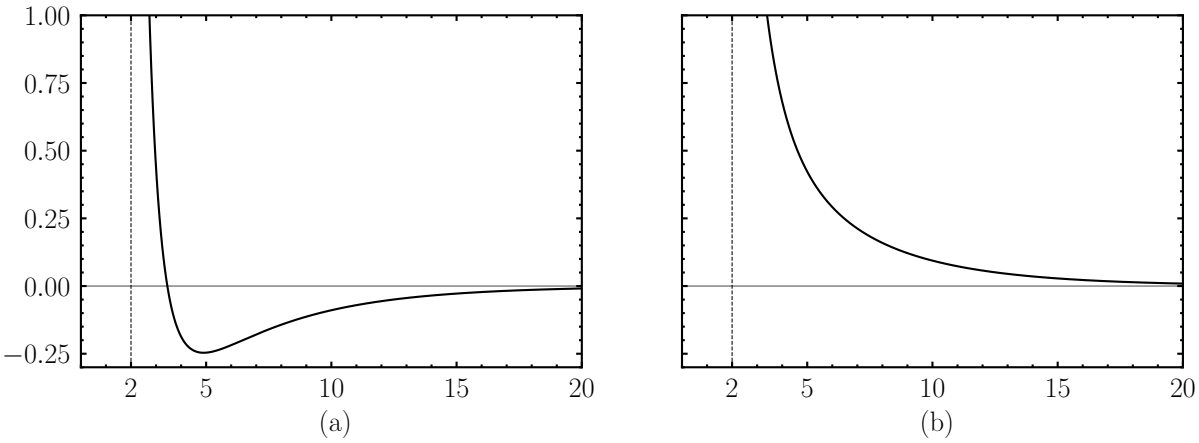

Figure 5.2 – Elastic interactions in units of k_BT between two pointlike proteins as a function of the dimensionless interprotein separation r/a_p, where a_p is the effective radius of proteins, in two cases: (a) for opposite curvatures, $C_1 = -C_2 = 0.04\,nm^{-1}$ and identical curvatures, $C_1 = C_2 = 0.04\,nm^{-1}$. The vertical dashed line indicates the length below which the steric repulsion occurs (overlapping between proteins is forbidden). The other parameters are $\kappa = 30k_BT$, $\xi = \sqrt{\kappa/\sigma} = 5a_p$ and $a_p = 10\,nm$.

recover the results of [161] which include hydrodynamics but not membrane fluctuations. In the second section, we will extend our simulation to take into account the membrane curvature and so the mediated interactions between proteins.

5.2 Diffusion of an assembly of proteins within a flat membrane

We consider N proteins placed randomly in a fluid membrane held flat and surrounded by a bulk fluid. We recall that the hydrodynamic couplings are taken into account through the positive definite mobility tensor $\tilde{\boldsymbol{O}}$ presented in Chap. 2 and Appx. A. The dynamics of such a system is described by the Langevin equation

$$\dot{\boldsymbol{r}}_n(t) = -\sum_m \tilde{\boldsymbol{O}}(\boldsymbol{r}_n - \boldsymbol{r}_m) \cdot \mathcal{H}_{\boldsymbol{r}_m} + \boldsymbol{\xi}_n(t), \tag{5.1}$$

where $-\mathcal{H}_{\boldsymbol{r}_n}$ is the force exerted on the protein located at $\boldsymbol{r}_n$ and $\boldsymbol{\xi}_n$ are Gaussian white noises with zero mean and variance

$$\langle \boldsymbol{\xi}_n(t) \boldsymbol{\xi}_m(t') \rangle = 2k_\mathrm{B}T\tilde{\boldsymbol{O}}(\boldsymbol{r}_n - \boldsymbol{r}_m)\delta(t - t'). \tag{5.2}$$

Note that, since the membrane remains flat, proteins do not act on the membrane and therefore $\mathcal{H}_{\boldsymbol{r}_n} = 0$, and the only forces are the stochastic ones, just as in [161].

5.2.1 Numerical method

To perform the simulations, we use the methods of Brownian dynamics with hydrodynamic interactions; we first discretize the equations by means of the Ermak-McCammon scheme [82, 163], *i.e.*, a stochastic first-order forward integration scheme. Therefore, we describe the displacements of proteins with the equation

$$r_{i,n}(t + \tau) = r_{i,n}(t) + \sqrt{2k_\mathrm{B}T\tau}\, \Gamma_{ij}(\boldsymbol{r}_n - \boldsymbol{r}_m)\, \eta_j(t), \tag{5.3}$$

where $\tau > 0$, η_j are independent Gaussian variables with 0 mean and standard deviation 1 which are simulated by generating uniform variables and transforming them into Gaussian ones with a Box-Müller algorithm [164]. Since the mobility tensor $\tilde{\boldsymbol{O}}(\boldsymbol{r}_n - \boldsymbol{r}_m)$ is positive definite, we can use the Cholesky decomposition that introduces a sort of square-root of matrix: $\tilde{O}_{ij} = \Gamma_{ij}\Gamma^T_{ij}$, with $\boldsymbol{\Gamma}(\boldsymbol{r}_n - \boldsymbol{r}_m)$ the unique lower triangle matrix giving this decomposition. Therefore, the variance of the second term of the rhs is consistent with the fluctuation-dissipation relation (5.2). Numerically, we use the positive definite tensor $\tilde{\boldsymbol{O}}$ given by [80]

$$\tilde{O}_{ij}^{\alpha=\beta} = \frac{1}{4\pi\eta_2}\left(\ln\frac{2\ell_\mathrm{SD}}{a_p} - \gamma\right)\delta_{ij}, \tag{5.4}$$

$$\tilde{O}_{ij}^{\alpha\neq\beta} = \frac{1}{4\pi\eta_2}\left[\left(\ln\frac{2\ell_\mathrm{SD}}{r} - \gamma - \frac{1}{2}\left(1 - \frac{2a_p^2}{r^2}\right)\right)\delta_{ij} + \left(1 - \frac{2a_p^2}{r^2}\right)\frac{r_i r_j}{r^2}\right], \tag{5.5}$$

where $\ell_{\mathrm{SD}} = \eta_2/(2\eta)$ is the Saffman-Delbrück length, γ Euler's constant and a_p the proteins' radius. From the first equation, one can recognize the Saffman-Delbrück law that defines the self-mobility ($\tilde{O}^{\alpha\alpha}$). We then get the matrix $\mathbf{\Gamma}$ by implementing a Cholesky decomposition algorithm on $\tilde{\boldsymbol{O}}$ [165].

Thus, at each time step τ, we compute simultaneously the new positions $\boldsymbol{r}_n(t+\tau)$. Then, we update the current positions preventing overlapping between proteins, *i.e.*, we check one protein by one that the distance between its new position and another protein is less than $2a_p$, rejecting the new position if this condition is not fulfilled.

To perform the simulation, we also need to choose physically consistent parameter values. First, we take $a = k_{\mathrm{B}}T = \eta = 1$, *i.e.*, the unit of length is a, which is the membrane thickness, the energy unit is $k_{\mathrm{B}}T$ and the time unit is $4\eta a^3/k_{\mathrm{B}}T$ where η is the bulk fluid viscosity. Typical values for the parameters are $a \simeq 5\,\mathrm{nm}$, $T \simeq 300\,\mathrm{K}$, $\eta \simeq 10^{-3}\,\mathrm{J\,s\,m^{-3}}$ (water), which yields a unit of time around $1\,\mu\mathrm{s}$ and $\eta_2 \simeq 10^{-9}\,\mathrm{J\,s\,m^{-2}}$. We take $\tau \simeq 0.1\,\mu\mathrm{s}$, the largest characteristic time for which the algorithm converges. Finally we consider an assembly of up to $N = 50$ proteins placed randomly inside a circle of radius $R_0 = 10\,\mathrm{nm}$ like in [161]. It may be worth noting that unlike [161] where the authors consider a finite patch of fluid with periodic conditions, we do not need this assumption; otherwise, we would have needed to take into account the infinite images due to the long-rangedness of the hydrodynamic couplings.

5.2.2 Short time diffusion coefficients

We remind that the diffusion coefficient D of a two-dimensional system is related to its mean square displacement $\langle R^2\rangle$ by the equation

$$D(t) = \frac{1}{4}\frac{\mathrm{d}\langle R^2\rangle}{\mathrm{d}t}. \tag{5.6}$$

The authors of [161] simulated the evolution of the protein assembly up to a time of order 0.1 ms. At such a short time, the mean square displacements of both the center of mass $\langle R^2_{\mathrm{CM}}\rangle$ and the gyration radius $\langle R^2_g\rangle$ are approximately linear, *i.e.*, the associated diffusion coefficients are constants given by the generic relation $\langle R^2\rangle = 4Dt$. Repeating the simulation for different numbers N of proteins in the assembly, the center of mass diffusion coefficient D_{CM} is found to decay with N without hydrodynamic correlations whereas it is almost unchanged in their presence [161].

Since our model is similar, we should be able to retrieve the results of [161]. Therefore, we reproduce their simulations using their parameter values, especially, we take $a_p = 0.5\,\mathrm{nm}$; a value that will be changed to 5 nm in the following to be closer to the real proteins' radius (see Chap 1).

Thereby, in Fig. 5.3 we compare our results of D_{CM} as a function of N with [161]. First, the diffusion coefficients D_{CM} and D_{g} are comparable, which is expected in the presence of hydrodynamic correlation. Since we perform an average over 1000 runs, we get more accurate diffusion coefficients values than [161] (the authors performed an average on 100 runs). Therefore our results are closer to the expected diffusion coefficients.

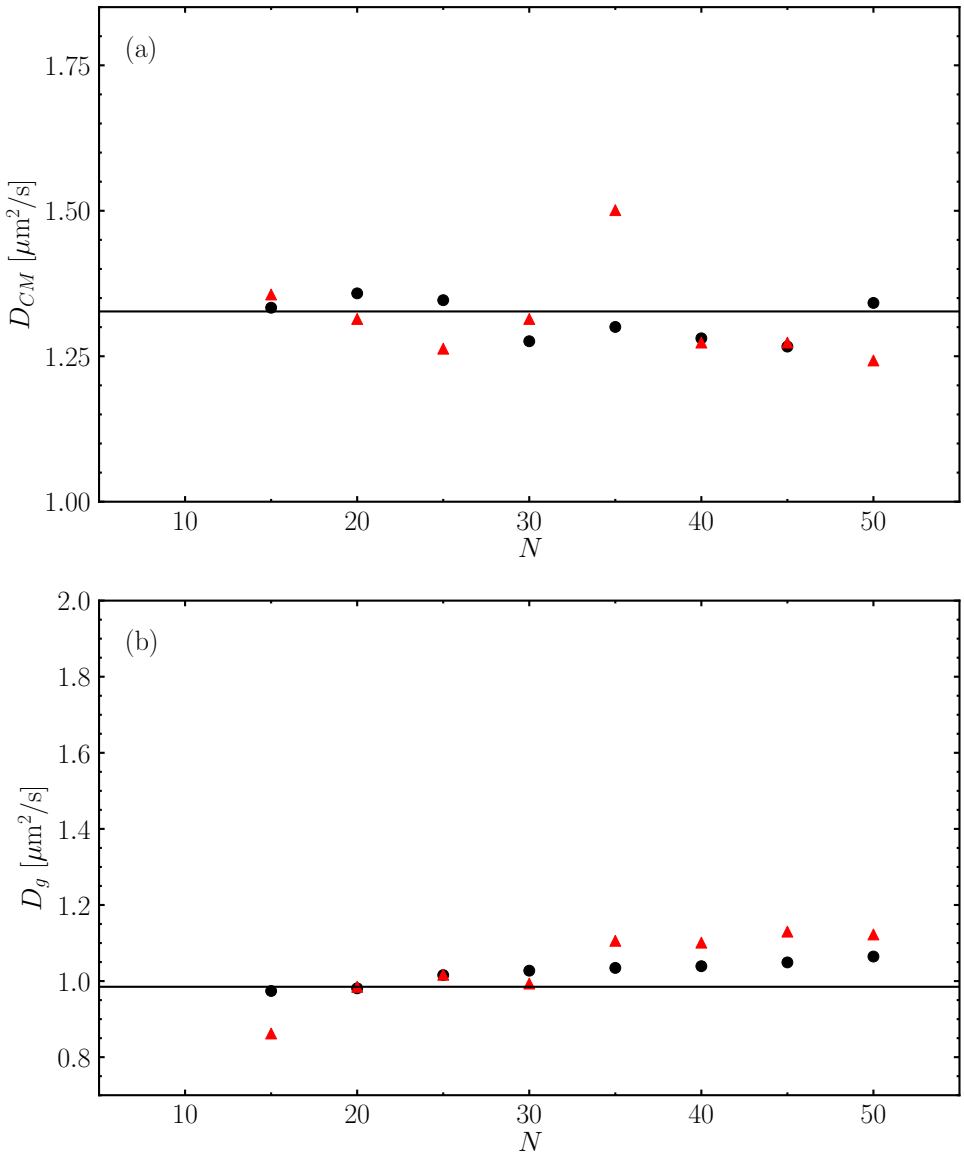

Figure 5.3 – Numerical diffusion coefficients of the center of mass (a) and growth of the gyration radius (b) as a function of the number N of proteins in the assembly. The red triangles and black circles correspond to the diffusion coefficient values given in [161] and those obtained numerically with our own simulations, respectively. (a) the solid line corresponds to the expected diffusion coefficient D_0 for an isolated protein determined with the SD law [70], which gives $D_0 \simeq 2.31\,\mu\text{m}^2\text{s}^{-1}$ for $\ell_{\text{SD}} = 500\,\text{nm}$, $a_p = 0.5\,\text{nm}$, $\eta_2 = 10^{-9}\,\text{Jsm}^{-2}$ and $T = 300\,\text{K}$. (b) the solid line corresponds to the analytical prediction of D_g for $N \gg 1$ and $R_0 = 10\,\text{nm}$ determined in [161]. The diffusion coefficient values are averaged over 1000 runs.

5.2.3 Time evolution of the diffusion of the center of mass

By assuming a time-independent interprotein distribution and using the Einstein relation that links the diffusion coefficient to the positive definite mobility tensor $\tilde{\boldsymbol{O}}(\boldsymbol{r})$, one can

determine analytically a self-consistent equation for the time evolution of D_{CM} [161]:

$$D_{\mathrm{CM}}(t) = \frac{k_{\mathrm{B}}T}{8\pi\eta_2}\left\{-\ln\left[\frac{1}{4\ell_{\mathrm{SD}}^2}(R_0^2 + 4D_0 t - 4\int_0^t D_{\mathrm{CM}}(s)\mathrm{d}s)\right] - 2\gamma - 2b\right\}, \tag{5.7}$$

where b is a geometric factor that depends on the interprotein separation distribution. For instance, if the interprotein distribution is a Gaussian, $b = \frac{1}{2}(\ln 2 - \gamma)$ and if it is a uniform distribution, $b = -\frac{1}{4}$ [161]. Unfortunately, the authors of [161] did not perform simulations where the time evolution of the diffusion of the center of mass can be determined numerically. We have simulated the evolution of an assembly of proteins up to $t = 1\,\mathrm{ms}$ to compare with the analytic predictions of this article. In Fig. 5.4, we compare the evolution of the numerical diffusion coefficient D_{CM} to analytical ones where either a uniform or Gaussian interprotein distribution is assumed. Qualitatively, as predicted in [161], initially and at short time, the interprotein distances are distributed along the initial distribution (uniform in our simulations), and then, at a time long enough, the distribution of the interprotein distances tends to a Gaussian, regardless of the initial distribution. Thereby, our numerical method allows us to perform long time simulations, and, in doing so, to validate the approximations used in [161] to determine analytically the behavior of the collective diffusion.

5.3 Collective diffusion of curvature-inducing proteins in a fluctuating membrane

Now, let us consider a membrane deformed locally by proteins and that can fluctuate. Therefore, we consider a membrane fluid whose dynamics is described through its height field $h(\boldsymbol{r})$ and of viscosity η_2 surrounded by a three-dimensional bulk fluid with viscosity η. The membrane contains N curvature-inducing proteins with spontaneous curvature $\pm c_0$. The dynamics of such a system was derived in Sec. 2.2.2:

$$\dot{h}_{\boldsymbol{q}}(t) = -\frac{1}{4\eta q}\frac{\delta\mathcal{H}}{\delta h} + \nu_{\boldsymbol{q}}(t), \tag{5.8}$$

$$\dot{\boldsymbol{r}}_n(t) = -\sum_m \tilde{\boldsymbol{O}}(\boldsymbol{r}_n - \boldsymbol{r}_m)\cdot\frac{\partial\mathcal{H}}{\partial\boldsymbol{r}_m} + \boldsymbol{\xi}_n(t), \tag{5.9}$$

where $\mathcal{H}$ is the Hamiltonian composed of the usual Canham-Helfrich energy and the elastic interaction between membrane-proteins with a coupling strength κ_p (see Chap. 2). The dynamics of the membrane field $h(\boldsymbol{q}, t)$ has been discretized in space since we perform the simulations on a finite lattice membrane patch of size L. The noises follow the fluctuation-dissipation relation ($k_{\mathrm{B}} = 1$):

$$\langle\nu_{\boldsymbol{q}}(t)\nu_{\boldsymbol{q}'}(t')\rangle = \frac{T}{2\eta q}L^2\delta_{\boldsymbol{q}+\boldsymbol{q}',\boldsymbol{0}}\,\delta(t-t'), \tag{5.10}$$

$$\langle\boldsymbol{\xi}_n(t)\boldsymbol{\xi}_m(t')\rangle = 2k_{\mathrm{B}}T\tilde{\boldsymbol{O}}(\boldsymbol{r}_n - \boldsymbol{r}_m)\delta(t-t'), \tag{5.11}$$

$$\langle\nu_n\boldsymbol{\xi}_m\rangle = \boldsymbol{0}. \tag{5.12}$$

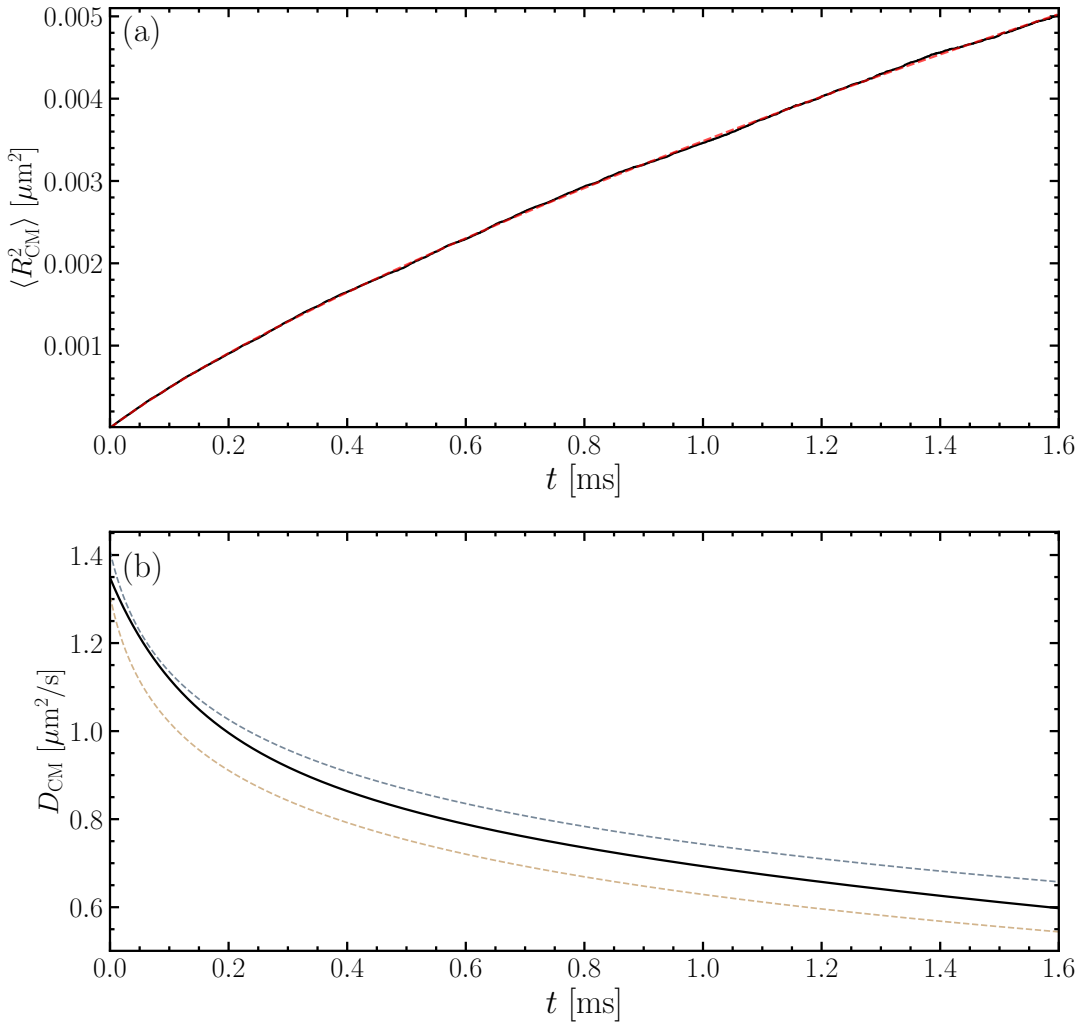

Figure 5.4 – Determination of the time evolution of center of mass diffusion coefficient D_{CM}. (a) Evolution of the mean square displacement of the center of mass $\langle R^2_{\mathrm{CM}} \rangle$ for $N = 50$ proteins. The average was performed over 10000 runs with parameters $a_p = 0.5\,\mathrm{nm}$, $R_0 = 10\,\mathrm{nm}$, $\eta_2 = 10^{-9}\,\mathrm{Jsm}^{-2}$ and $\ell_{\mathrm{SD}} = 500\,\mathrm{nm}$. The red dashed curve is a fractional fit of the form $(a_1 t + a_2 t^2)/(b_0 + b_1 t + b_2 t^2)$ whose derivative gives an estimate of the diffusion coefficient. (b) Time evolution of the diffusion coefficient D_{CM}. The black curve corresponds to the numerical coefficient we get with the derivative of the former fit. The grey and tanned dashed curves correspond to the analytical expectations determined with Eq. (5.7) for a uniform interprotein separation and a Gaussian one, respectively.

Since we have two coupled dynamical equations we first study their decoupled dynamics to determine their respective characteristic time evolution, *i.e.*, we estimate the displacement of a disk-like protein in a non-fluctuating membrane fluid and the relaxation of membrane modes from a deformation regardless of the coupling with proteins. The former phenomenon is described by a Brownian motion with a diffusion coefficient given by the Saffman-Delbrück law [70], D_0. Therefore, during a time Δt, the characteristic displacement Δl of the protein is given by

$$\Delta l \sim \sqrt{D_0 \Delta t}. \tag{5.13}$$

The latter case can be studied using the noiseless version of Eq. (5.8) with the standard Canham-Helfrich Hamiltonian (see Sec. 2.1.1) in Fourier space:

$$4\eta q \dot{h}_{\boldsymbol{q}} = -(\kappa q^4 + \sigma q^2) h_{\boldsymbol{q}}. \tag{5.14}$$

The solution of this first order differential equation introduces the characteristic time $\tau_{\boldsymbol{q}}$ of the relaxation given by

$$\tau_{\boldsymbol{q}} = \frac{4\eta}{\kappa q^3 + \sigma q}. \tag{5.15}$$

Moreover we use the physical parameters $\eta_2 = 10^{-9}\,\mathrm{Jsm}^{-2}$, $\eta = 10^{-3}\,\mathrm{Jsm}^{-3}$, $a = 5\,\mathrm{nm}$, $\kappa = 20 k_\mathrm{B} T$ and a weak surface tension $\sigma = 8.3\,10^{-6}\mathrm{Jm}^{-2}$ to ensure long-range protein-protein interactions. The protein displacement causes membrane deformations at different length scales, from the shortest meaningful length $2a_p$ to wavelengths of the order the size L of the patch. Therefore, we compare the characteristic time on these two extrema. For a mode of a length comparable to the size of a protein, *i.e.*, $\pi/q = 2a_p = 10\,\mathrm{nm}$, the relaxation time is around $\tau_{\boldsymbol{q}} \simeq 1.6\,\mathrm{ns}$. In the meantime, the protein moves a characteristic distance of $\Delta l \simeq 50\,\mathrm{pm}$. The time it takes for the protein to move a distance comparable to this mode, *i.e.*, $\Delta l = 2a_p$, is $\Delta t \simeq 64\,\mu\mathrm{s}$. Now, considering a mode comparable to the membrane patch length $L = 300\,\mathrm{nm}$, $\pi/q = L$, the characteristic relaxation time of the membrane is $\tau_{\boldsymbol{q}} \simeq 22\,\mu\mathrm{s}$. A displacement of the same order, $\Delta l = L$ needs a characteristic time $\Delta t \simeq 58\,\mathrm{ms}$. Therefore, while the dynamics of the membrane operates at fast time scales, the proteins have a slow dynamics. Thus, the relaxation of the membrane field can be considered instantaneous with respect to the dynamics of the proteins.

5.3.1 Simulation method

Since we take into account the membrane height field, we simulate a finite membrane square patch of size L and we assume periodic boundary conditions (PBCs) for the membrane only. As for proteins, if we assume PBCs, we will have to consider the interactions between the original proteins and their images through Ewald summation [166, 167] because the hydrodynamic correlations are long-range. Thereby, to avoid these additional computations we do not take PBCs for proteins, and we simulate at times short enough to keep proteins away from the original membrane patch. Besides, since we take a patch

of length $L = 330\,\mathrm{nm}$ that is close to the Saffman-Delbrück length, $\ell_{\mathrm{SD}} = 500\,\mathrm{nm}$, the mobility tensor $\tilde{\boldsymbol{O}}(\boldsymbol{r})$ derived earlier is invalid to describe the hydrodynamic interactions in assemblies whose size becomes comparable to the membrane patch length.

We introduce an ultraviolet cutoff $\Lambda = \pi/a$ in order to get rid of Fourier modes associated with lengths smaller than the membrane thickness a as we assume the membrane to be bi-dimensional. In the following Therefore the modes are according to

$$\boldsymbol{q} = \frac{2\pi}{La}(n, m), \qquad n, m \text{ integers} \in \left[-\frac{L}{2}, \frac{L}{2}\right]. \tag{5.16}$$

Since we assume a discretized membrane field, we use the following discrete Fourier transform and discrete inverse Fourier transform

$$h_{\boldsymbol{q}} = \sum_{\boldsymbol{r}} h_{\boldsymbol{r}} \mathrm{e}^{-i\boldsymbol{q}.\boldsymbol{r}}, \qquad h_{\boldsymbol{r}} = \frac{1}{L^2} \sum_{\boldsymbol{q}} h_{\boldsymbol{q}} \mathrm{e}^{i\boldsymbol{q}.\boldsymbol{r}}. \tag{5.17}$$

Numerically, these transforms will be performed via Fast Fourier Transform algorithms when needed.

To simulate the dynamics we use an Ermak's scheme similar to that used in the previous section:

$$h_{\boldsymbol{q}}(t+\tau) = h_{\boldsymbol{q}}(t) - \frac{1}{4\eta}\left[(\kappa q^3 + \sigma q) h_{\boldsymbol{q}}(t) + \kappa_p \sum_{n=1}^{N} \frac{q_i q_j}{q} K_{ij}(\boldsymbol{r}_n) \mathrm{e}^{-i\boldsymbol{q}\cdot\boldsymbol{r}_n}\right]\tau + \nu_{\boldsymbol{q}}(t), \tag{5.18}$$

where the second term is composed of the non-interacting Helfrich Hamiltonian and the membrane-protein couplings with $K_{ij}(\boldsymbol{r}_n)$ the elements of the deviation curvature tensor at position $\boldsymbol{r}_n$ given by

$$K_{ij}(\boldsymbol{r}_n) = -\frac{1}{L^2} \sum_{\boldsymbol{k}} k_i k_j h_{\boldsymbol{k}} \mathrm{e}^{i\boldsymbol{k}\cdot\boldsymbol{r}_n} - c_0 \delta_{ij}. \tag{5.19}$$

Since the modes are complex, we first need to decompose this equation into real and imaginary parts. The deterministic part is straightforward as only $h_{\boldsymbol{q}}$ and $\mathrm{e}^{-i\boldsymbol{q}\cdot\boldsymbol{r}_n}$ are complex. For the noise, we use the correlations $\langle \xi_{\boldsymbol{q}} \xi_{\boldsymbol{q}} \rangle = 0$ and $\langle \xi_{\boldsymbol{q}} \xi_{-\boldsymbol{q}} \rangle = 0$ to determine the variance of both its real and imaginary parts and we introduce independent identically distributed Gaussian variables $\zeta_{\boldsymbol{q}}$ that satisfy the fluctuation-dissipation theorem such that

$$\langle \zeta_{\boldsymbol{q}}^2 \rangle = \frac{k_{\mathrm{B}} T}{8\eta q} L^2 \tau, \tag{5.20}$$

$$\mathrm{Re}\, \xi_{\boldsymbol{q}} = \zeta_{\boldsymbol{q}} + \zeta_{-\boldsymbol{q}}, \tag{5.21}$$

$$\mathrm{Im}\, \xi_{\boldsymbol{q}} = \zeta_{\boldsymbol{q}} - \zeta_{-\boldsymbol{q}}, \tag{5.22}$$

$$\tag{5.23}$$

to decouple the modes, *i.e.*, while the complex variables $\xi_{\boldsymbol{q}}$ and $\xi_{-\boldsymbol{q}}$ are coupled, the real variables $\zeta_{\boldsymbol{q}}$ and $\zeta_{-\boldsymbol{q}}$ are independent. We use a Box-Müller algorithm to generate these variables.

Regarding the dynamics of the proteins, the novelty lies in the elastic forces applied by the membrane in addition to the stochastic forces. These forces are given by

$$-\mathcal{H}_{\boldsymbol{r}_n} = -\kappa_p K_{ij}(\boldsymbol{r}_n)\boldsymbol{\nabla}\partial_i\partial_j h(\boldsymbol{r})|_{\boldsymbol{r}=\boldsymbol{r}_n}. \tag{5.24}$$

Therefore, we simulate the dynamics of the proteins in the same way as previously, we apply an Ermak-McCammon scheme to get the equation

$$r_{i,n}(t+\tau) = r_{i,n}(t) - \sum_m \tilde{O}_{ij}(\boldsymbol{r}_n - \boldsymbol{r}_m)\frac{\partial \mathcal{H}}{\partial \boldsymbol{r}_m, j}\,\tau + \sqrt{2k_\mathrm{B}T\tau}\,\Gamma_{ij}(\boldsymbol{r}_n - \boldsymbol{r}_m)\,\eta_j(t), \tag{5.25}$$

and we compute the mobility tensor elements $\tilde{O}_{ij}$ for all proteins at each time step along the matrix elements Γ_{ij} determined by a Cholesky decomposition.

Note that the dynamics of the proteins is in continuous space despite the coupling with the space-discretized membrane field. Since $K_{ij}(\boldsymbol{r}_n)$ is just a number updated at each step, we do not need to place the proteins on lattice sites to perform the computation of the membrane-protein interaction term in Eq.(5.18). Thus, at each time step, we first compute the elements $K_{ij}(\boldsymbol{r}_n)$ and the forces $-\mathcal{H}_{\boldsymbol{r}_n}$ exerted by the membrane on the proteins, and then we update the dynamics of the membrane and the proteins simultaneously.

Furthermore, since we include the fast dynamics of the membrane, we adopt an appropriate time step for the simulation. To do so, we need all the modes to converge, *i.e.*, the time step should be smaller than the characteristic relaxation time of the fastest mode with norm $q = \sqrt{2}\pi$ given by Eq. (5.15). In addition, the time step should not be too small in order to avoid unnecessary computational costs. Therefore, we end up with $\tau = 0.1\,\mathrm{ns}$.

5.3.2 Results

As previously, we are interested in the diffusion of the center of mass and growth of the radius of gyration, and how it compares to the case without membrane fluctuations. We consider an assembly of up to $N = 25$ proteins of radius $a_p = 5\,\mathrm{nm}$ such that the size of a protein is equal to the unit length $a = 10\,\mathrm{nm}$ to keep them pointlike. These proteins induce a spontaneous curvature $c_0 = 0.04\,\mathrm{nm}^{-1}$ with a moderate strength $\kappa_p = 4 \times 10^{-17}\,\mathrm{Jnm}^2$ on the membrane. It may be worth noting that the largest value of κ_p is dependent of the time step Δt since large values needs smaller time steps to prevent the numerical scheme from diverging.

Initially, the proteins are placed randomly in a circle of radius $R_0 = 38\,\mathrm{nm}$. With these parameters, we were able to simulate the evolution of the assembly until a time around $t = 0.4\,\mathrm{ms}$.

Since the proteins all have the same spontaneous curvature, they quickly create a region with a favorable curvature for the proteins. Thus, despite the repulsive interactions between the proteins, they remain grouped (see Fig. 5.5). How strong this effect is remains to be further investigated.

In Fig. 5.6, we see that the mean square displacements of the center of mass $\langle R^2_{\mathrm{CM}}\rangle$

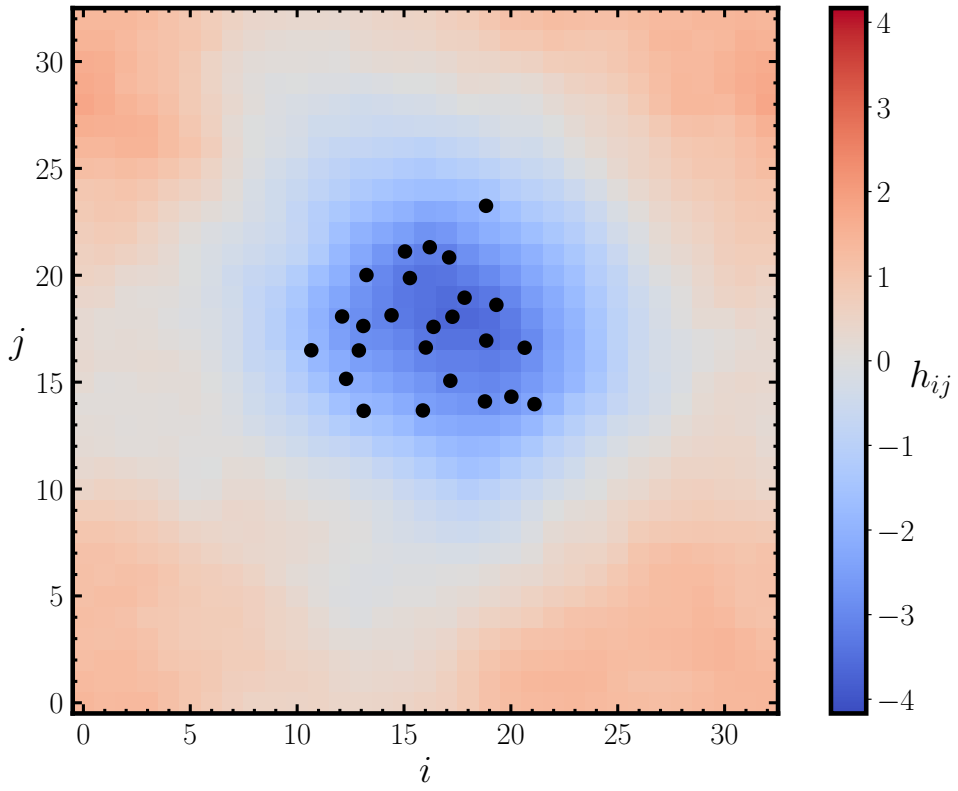

Figure 5.5 – Top view snapshot of the membrane containing $N = 25$ proteins at time $t = 0.15\,\mathrm{ms}$. i and j are used to indicate the membrane lattice sites. The spontaneous curvature, being positive, generates negative bumps (blue area). The parameters are $\kappa = 20 k_\mathrm{B} T$, $\sigma = 2 \times 10^{-5}\,\mathrm{Jm^{-}2}$, $\eta = 10^{-3}\,\mathrm{Jsm^{-3}}$, $\eta_2 = 10^{-9}\,\mathrm{Jsm^{-2}}$, $\kappa_p = 4 \times 10^{-17}\,\mathrm{Jnm^2}$, $c_0 = 0.04\,\mathrm{nm^{-1}}$ and $a_p = 5\,\mathrm{nm}$.

and of the gyration radius $\langle R_g^2 \rangle$ are of the same order at short times, *i.e.*, around $t = 0.1\,\mathrm{ms}$. We deduce that the collective behavior observed in [161] still exists in spite of the presence of curvature couplings and fluctuations. Therefore, despite the elastic repulsive interactions between proteins, the hydrodynamic couplings dominate and still generate a collective behavior between proteins.

In Fig. 5.7a, we compare the mean square displacement of the center of mass in the presence of curvature couplings with its counterpart where the curvature was neglected. Although both have the same behavior, we see a discrepancy: in the presence of curvature couplings, the mean square displacements increase slower. Keeping in mind the effects of fluctuations on the mobility of a single isolated protein [66], we deduce that this discrepancy comes from the correlations $\langle \boldsymbol{\xi}(t) \cdot \boldsymbol{f}(t') \rangle$ according to the mechanism presented above in the introduction. Further studies are needed on these correlations to better quantify their effect. We also compare the growth of the radius of gyration with and without the curvature couplings (see Fig. 5.7b). In the presence of curvature couplings, the growth of the radius of gyration is slightly reduced. Therefore, we expect a slower growth which still needs to be further investigated by simulating at larger times.

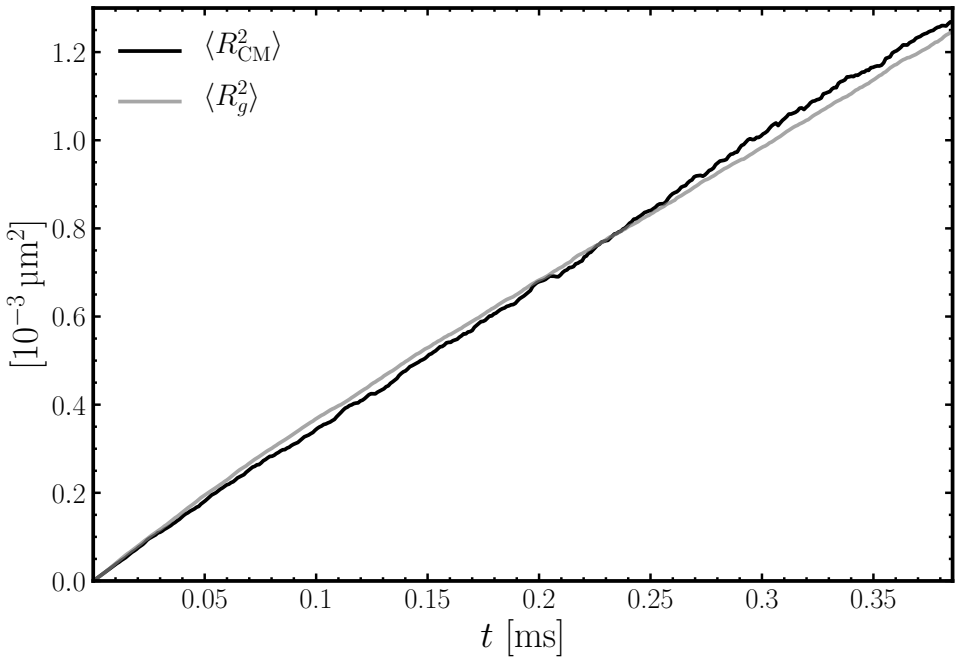

Figure 5.6 – Evolution of the mean square displacement of the center of mass and growth of the radius of gyration for an assembly of $N = 25$ curvature-inducing proteins. The black curve corresponds to $\langle R^2_{\mathrm{CM}} \rangle$ and the lightgray curve to $\langle R^2_g \rangle$. Since these quantities are comparable, we see the emergence of a collective motion due to the hydrodynamic couplings between proteins [161]. The parameters are given Fig. 5.5. The average was performed over 1000 realizations.

5.4 Overview

We have first extended the simulations of proteins in a flat membrane further in time which permitted us to probe the analytical predictions made in [161] based on ill-controlled approximations concerning the anomalous diffusion of an assembly of proteins subject to hydrodynamic correlations.

We have then taken into account the membrane-proteins curvature couplings and fluctuations. The presence of curvature couplings reduces the diffusion coefficient of the center of mass, as the mean square displacements are reduced with respect to the flat membrane case. Nevertheless $\langle R^2_g \rangle$ and $\langle R^2_{\mathrm{CM}} \rangle$ remain of the same order, and therefore the collective behavior of the assembly still exists.

It would be highly interesting to study analytically the diffusion in presence of curvature couplings. Since we take into account the membrane fluctuations, assumptions on the interprotein distribution have to be made as the correlations are not instantaneous in this case. However, given that the dynamics of the membrane is much faster than the one of the proteins, it can be possible to "preaverage" the membrane field [66] and therefore assume that the interprotein distribution is a Gaussian again whose variance remains to be determined. Moreover, further investigations are needed to determine the effects of curvature-inducing proteins. First, we did not take into account the effect of the membrane local geometry on the displacements of the proteins, *i.e.*, we assumed that the metric tensor is $\boldsymbol{g} = \mathbb{1}$ [66, 168]. In order to study non-equilibrium systems like the

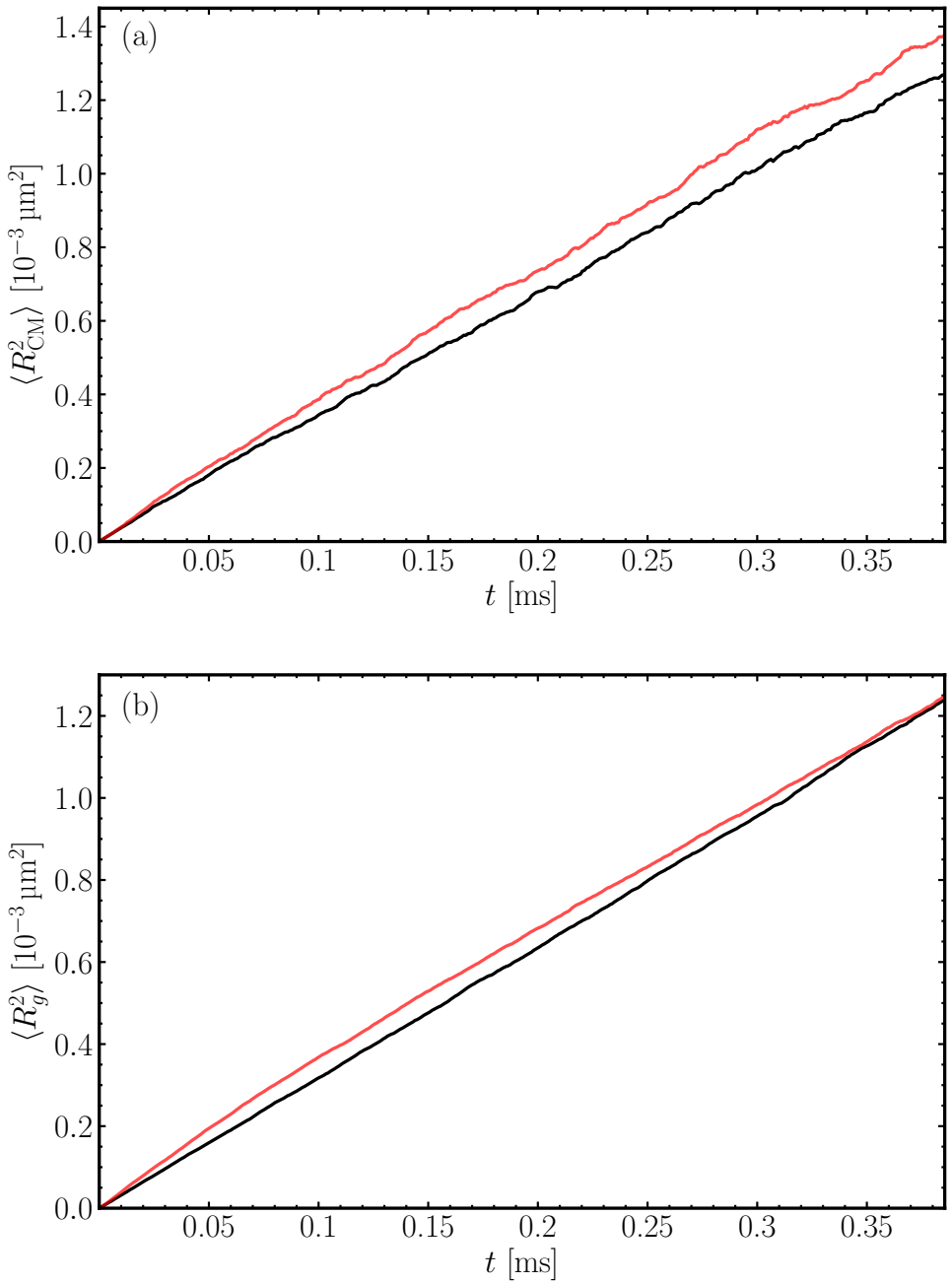

Figure 5.7 – Mean square displacements of the center of mass (a) and of the growth of the radius of gyration (b) as a function of time for an assembly of $N = 25$ proteins in presence of curvature couplings and fluctuations (black) and for a membrane held flat (red). The average was performed over 1000 runs and the parameters we use are given Fig. 5.6.

BmrA proteins, we should now allow for conformation changes, that can be encoded, in the spirit of [169], in a stochastic c_0 in the energy Eq. (2.21).

Conclusion

This thesis has allowed us to gain insights into the collective behavior of passive and conformationally active proteins embedded within biological membranes.

We have first determined the membrane phase diagram in presence of binding of curvature-inducing proteins in thermal equilibrium. We found three phases: an unbound uniform flat phase (U), a bound uniform phase (B), and a separated/corrugated phase (SC). By means of a nonlinear analysis, we were able to find the pattern selected by the membrane in the unstable SC phase: proteins form hexagonally-ordered bowl-shaped domains. We pushed the analysis further by introducing a Poisson rate to translate the unbinding mechanism into mathematical terms, thereby breaking the detailed balance condition and thus driving the system out of thermal equilibrium. The active unbinding process is found to alter the stability of the unstable phase, *i.e.*, it shifts the unstable region to higher chemical potentials and spontaneous curvatures.

We have then investigated the diffusion of a single protein in a non-fluctuating membrane where we were able to elegantly rederive the mobility formula (SD law) of such a system within the simplifying assumption that it can be considered a pointlike object. The only price to pay is the use of a small wavelength cutoff of the order the inverse of the protein's size. We have then exploited this approach by taking into account the bilayer property of the membrane where the SD law is found to generalize; for a protein moving within one monolayer, the diffusion is influenced by the intermonolayer friction: at high frictions, the SD law remains; at frictions lower than a threshold, which depends on the membrane viscosity and the protein size, the mobility increases since the monolayer without the protein is not fully dragged by the protein. In addition, we have considered the case of a protein that induces a local and isotropic spontaneous curvature. Our method has allowed us to derive the total friction of the latter, which is given by the sum of the usual SD friction and extra friction coming from the pull-back created by the membrane deformation.

Finally, we have studied the diffusion of an ensemble of curvature-inducing proteins. A numerical study considering a non-fluctuating membrane has allowed us to probe the subdiffusive nature of the collective diffusion predicted in the literature, as well as the evolution of the interprotein distribution. Finally, taking into account the fluctuations of the membrane, our numerical simulations have shown that proteins still behave collectively, despite a change in the collective diffusion coefficient with respect to the non-fluctuating membrane case.

Of course, our study calls for further investigations. First, even if we suspect the pull-back mechanism the membrane exerts on the proteins to be responsible for the difference observed in the collective diffusion between the non-fluctuating and fluctuating membrane cases, the proof is not clearly established as the contributions of the different correlations remain to be explored. Then, it would probably be possible to conduct an analytical study of the collective diffusion coefficient to fully quantify the effect of curvature on diffusion and to guide the analysis of numerical simulations.

Another interesting project would be to drive the system (proteins and membrane) out of equilibrium. This could be studied by incorporating an active switching rate that breaks the detailed balance condition.

Appendix A

Definite positive tensor for cylinders in a fluid sheet

In their article [80], Sokolov and Diamant derive the positive definite mobility tensor for cylindrical objects embedded in a two-dimensional fluid using the procedure Rotne and Prager used to determine the positive definite mobility tensor for polymers in a 3D suspension [84]. For the sake of completeness, we give the derivation performed and explained in [80], adding some specifications on intermediate steps.

First, it is convenient and usual to use the Oseen approximated mobility tensor derived by Kirkwood and Riseman (KR) [170] to describe the hydrodynamic interactions between the objects embedded in a fluid. Nevertheless, this tensor is not always positive definite, *e.g.* depending on the strength of the hydrodynamic interaction (for physical values indeed), the diffusion of a rigid rodlike polymer in a 3D fluid can be negative and thus is unphysical [81] (it leads to a negative dissipative power which breaks the Second law of the thermodynamics). As a definite positive mobility tensor for every physical value is needed both for thermodynamics laws and for numerical simulation using Cholesky-like decomposition, Rotne and Prager used an ansatz for the exact stress tensor to minimize the energy dissipation rate caused by the motion of the suspending fluid [84]. As stated by Sokolov and Diamant, the definite positive tensor found by the formers is the standard KR tensor plus a correction to the second order in a/r where a is the radius of the proteins and r is the separation between the pair proteins considered [80].

We first apply the Rotne-Prager method to cylindrical objects whose motion is constrained in a plane (two-dimensional dynamics) following [80]. Then, we derive the correct definite-positive tensor obtained in the case that overlapping between objects is authorized.

A.1 Rotne Prager method applied on cylinders in a fluid sheet

We consider a configuration $\mathbb{r}$ of disk inclusions of radius a driven by forces $\mathbb{F}$ whose movements are constrained into a sheet of viscosity η_2 and distances r between them are such that $r \ll \kappa^{-1} = \eta_2/(2\eta)$, where η is the viscosity of the 3D fluid surrounding the sheet and κ^{-1} the well-known Saffman-Delbrück length. The mobility tensor can be derived by minimizing the energy dissipation rate ϵ due to the viscous flow which is given by

$$\epsilon = \frac{1}{2\eta_2} \int \mathrm{d}^2 r \, \tau_{\alpha\beta}(\boldsymbol{r}) \, \tau_{\beta\alpha}(\boldsymbol{r}), \tag{A.1}$$

where we integrate over the whole area excluding the areas of the inclusions and $\boldsymbol{\tau}(\boldsymbol{r})$ is the viscous stress tensor at $\boldsymbol{r}$ given by

$$\tau_{\alpha\beta}(\boldsymbol{r}) = \eta_2 \left[\partial_\alpha u_\beta(\boldsymbol{r}) + \partial_\beta u_\alpha(\boldsymbol{r}) \right], \tag{A.2}$$

with $\boldsymbol{u}(\boldsymbol{r})$ the flow field. Moreover, the total stress tensor $\boldsymbol{\sigma}$ is given by

$$\sigma_{\alpha\beta}(\boldsymbol{r}) = -p(\boldsymbol{r})\delta_{\alpha\beta} + \tau_{\alpha\beta}(\boldsymbol{r}), \tag{A.3}$$

with p the pressure field. Both the total and viscous stress tensors satisfy the following properties:

$$\tau_{\alpha\beta} = \tau_{\beta\alpha}, \quad \sigma_{\alpha\beta} = \sigma_{\beta\alpha}, \tag{A.4}$$

$$\tau_{\alpha\alpha} = 0, \tag{A.5}$$

$$\partial_\beta \sigma_{\alpha\beta}(\boldsymbol{r}) = -\partial_\alpha p(\boldsymbol{r}) + \partial_\beta \tau_{\alpha\beta} = 0, \tag{A.6}$$

$$a \int_0^{2\pi} \mathrm{d}\theta \, \sigma_{\alpha\beta}(a\boldsymbol{n}^i(\theta)) n^i_\beta(\theta) = -F^i_\alpha, \tag{A.7}$$

where $\boldsymbol{F}^i$ is the force acting on the bead i and $\boldsymbol{n}^i$ is the unit normal to the surface of bead i. The first equation states that $\boldsymbol{\tau}$ and $\boldsymbol{\sigma}$ are symmetric. As $\boldsymbol{u}(\boldsymbol{r})$ is divergenceless, one gets that $\boldsymbol{\tau}$ is traceless so is Eq. (A.5). Eq. (A.6) corresponds to the divergenceless property of the total stress tensor assuming inertia is neglected (which leads to putting local forces acting on a fluid element to zero). Assuming the latter, the balance of forces gives that the total force exerted by the fluid flow on the surface of each bead compensates for the external force $\boldsymbol{F}^i$ applied to it, leading to Eq. (A.7).

Then one gets mobility tensor $\boldsymbol{B}^{ij}(\mathbb{r})$ for a configuration $\mathbb{r}$ of beads by equalizing the total energy dissipation rate ϵ due to the viscous flow with the power produced by beads under the action of the external forces:

$$\epsilon = F^i_\alpha v^i_\alpha = F^i_\alpha B^{ij}_{\alpha\beta}(\mathbb{r}) F^j_\beta. \tag{A.8}$$

Using the symmetric property of $\boldsymbol{\tau}$ and Eq. (A.1), it is clear that ϵ is positive and

vanished if and only if the viscous stress tensor is zero (which leads to zero external forces). Therefore the symmetric bilinear form of the rhs of Eq. (A.8) is a scalar product which leads to $\boldsymbol{B}^{ij}(\text{ɾ})$ being symmetric positive definite.

Nevertheless, the exact flow field $\boldsymbol{u}(\boldsymbol{r})$ that satisfies the boundary conditions of all inclusions is unknown and yet essential to determine the mobility tensor. We therefore, replace the exact stress tensor by a trial one $\bar{\boldsymbol{\sigma}}$ which must satisfy the conditions (A.4)–(A.7). Moreover, as ϵ is the minimum energy dissipation rate, any stress satisfying the properties (A.4)–(A.7) gives an energy dissipation rate $\bar{\epsilon}$ above the minimum ϵ, and thus a definite positive mobility tensor.

The ansatz Rotne and Prager made on the trial stress tensor is to take the superposition of the independent contributions of each inclusion:

$$\bar{\sigma}_{\alpha\beta}(\boldsymbol{r}) = -\bar{p}(\boldsymbol{r})\delta_{\alpha\beta} + \bar{\tau}_{\alpha\beta}(\boldsymbol{r}) = \sum_i \sigma^i_{\alpha\beta}(\boldsymbol{r} - \boldsymbol{r}^i), \tag{A.9}$$

with

$$\bar{p}(\boldsymbol{r}) = \sum_i p^i(\boldsymbol{r} - \boldsymbol{r}^i), \tag{A.10}$$

$$\bar{\tau}_{\alpha\beta}(\boldsymbol{r}) = \sum_i \tau^i_{\alpha\beta}(\boldsymbol{r} - \boldsymbol{r}^i), \tag{A.11}$$

where $\boldsymbol{\sigma}^i$, p^i, and τ^i are, respectively, the exact total stress, pressure, and viscous stress due to a single inclusion located at $\boldsymbol{r}^i$ with an external force $\boldsymbol{F}^i$ acting on it. It is straightforward to check that the stress tensor $\bar{\boldsymbol{\sigma}}$ satisfies the three first properties. For the last one, as $\boldsymbol{\sigma}^i$ is the exact total stress tensor it is clear that its integration over the surface of inclusion i gives $\boldsymbol{F}^i$. Now if we integrate it over the surface of another inclusion j, by using the divergence theorem we see that this integration vanishes. Therefore one has

$$a\int_0^{2\pi} \mathrm{d}\theta\, \sigma^i_{\alpha\beta}(a\boldsymbol{n}^i(\theta))n^i_\beta(\theta) = -F^i_\alpha, \tag{A.12}$$

$$a\int_0^{2\pi} \mathrm{d}\theta\, \sigma^i_{\alpha\beta}(\boldsymbol{r}^{ij} + a\boldsymbol{n}^j(\theta))n^j_\beta(\theta) = 0, \tag{A.13}$$

with $\boldsymbol{r}^{ij} = \boldsymbol{r}^j - \boldsymbol{r}^j$. Therefore integrating the total stress $\bar{\boldsymbol{\sigma}}$ over the surface of an inclusion gives the force acting on it and thus $\bar{\boldsymbol{\sigma}}$ satisfies the property (A.7). Note that the superposition $\bar{\boldsymbol{u}}$ of the flow field produced by a single inclusion does not satisfy the same boundary conditions as the exact flow field as each inclusion contribution is considered independently from the others.

As stated previously, the viscous stress tensor $\bar{\boldsymbol{\tau}}$ is associated to an approximate mobility tensor $\bar{\boldsymbol{B}}^{ij}(\text{ɾ})$ such that

$$\epsilon < \bar{\epsilon} = \frac{1}{2\eta_2}\int \mathrm{d}^2 r\, \bar{\tau}_{\alpha\beta}\, \bar{\tau}_{\beta\alpha} = F^i_\alpha \bar{B}^{ij}_{\alpha\beta}(\text{ɾ})F^j_\beta. \tag{A.14}$$

Note that the integral runs over the whole area excluding the areas of all inclusions, thus

this integration is really difficult to perform, therefore, as made by Rotne and Prager, we extend the definition of $\boldsymbol{\tau}^i$ into the inclusion domain such that $\boldsymbol{\tau}^j(|\boldsymbol{r}-\boldsymbol{r}^i|<a)=\mathbf{0}$ if $j=i$ and is nonzero if $i\neq j$. Furthermore, this extension of the area covered by the integration leads to adding more positive contributions to the dissipation and thus enforces the dissipation rate $\bar{\epsilon}$.

Using the definition of the total stress tensor $\bar{\boldsymbol{\sigma}}$ one can rewrite the above integral as

$$\frac{1}{2\eta_2}\int \mathrm{d}^2r\,\bar{\tau}_{\alpha\beta}\,\bar{\tau}_{\beta\alpha}=\frac{1}{2\eta_2}\int \mathrm{d}^2r\,\bar{\tau}_{\alpha\beta}\,(\bar{p}\,\delta_{\beta\alpha}+\bar{\sigma}_{\beta\alpha}). \tag{A.15}$$

As $\bar{\boldsymbol{\tau}}$ is traceless, the product between $\bar{\tau}_{\alpha\beta}$ and $\bar{p}$ appearing in the rhs vanishes. We then replace $\bar{\tau}_{\alpha\beta}$ by its definition given by Eq (A.2) and use the divergenceless and symmetric properties of $\bar{\boldsymbol{\sigma}}$ to change the rhs of the previous Eq into

$$\frac{1}{2\eta_2}\int \mathrm{d}^2r\,\bar{\tau}_{\alpha\beta}\,\bar{\sigma}_{\beta\alpha}=\int \mathrm{d}^2r\,\partial_\beta(\bar{u}_\alpha\bar{\sigma}_{\alpha\beta})=\sum_{i,j}\int \mathrm{d}^2r\partial_\beta(u^i_\alpha\sigma^j_{\alpha\beta}). \tag{A.16}$$

Then using the divergence theorem and the fact that $\boldsymbol{\sigma}^i$ is in the opposite direction of $\boldsymbol{n}^i$ we finally get

$$\begin{aligned}\frac{1}{2\eta_2}\int \mathrm{d}^2r\,\bar{\tau}_{\alpha\beta}\,\bar{\tau}_{\beta\alpha}=&-a\sum_i\int_0^{2\pi}u^i_\alpha(a\boldsymbol{n}^i)\sigma^i_{\alpha\beta}(a\boldsymbol{n}^i)n^i_\beta-a\sum_{i\neq j}\int_0^{2\pi}u^i_\alpha(\boldsymbol{r}^{ij}+a\boldsymbol{n}^j)\sigma^j_{\alpha\beta}(a\boldsymbol{n}^j)n^j_\beta\\&+a\sum_{i\neq j}\int_0^{2\pi}u^i_\alpha(a\boldsymbol{n}^i)\sigma^j_{\alpha\beta}(a\boldsymbol{n}^i-\boldsymbol{r}^{ij})n^i_\beta\end{aligned} \tag{A.17}$$

Using Eq. (A.14), by identification we see that the first integral of the rhs should give back the well-known Saffman-Delbrück self-mobility. For the last integral, we first remark that $\boldsymbol{u}(a\boldsymbol{n}^i)$ is independent of θ and then using Eq. (A.13) we see that this integral vanishes (see below). Therefore the second integral accounts for the off-diagonal terms of the mobility tensor for which $i\neq j$. The computation is given below.

To compute the integrals in the rhs of Eq. (A.17), we need to find $\boldsymbol{\sigma}^i$ and $\boldsymbol{u}^i(\boldsymbol{r})$. The latter corresponds to the flow velocity of the fluid at point $\boldsymbol{r}$ produced by a single disk inclusion located at the origin and driven by a force $\boldsymbol{F}^i$. This flow is given by [77]

$$u^i_\alpha(\boldsymbol{r})=U_{\alpha\beta}F^i_\beta, \tag{A.18}$$

$$U_{\alpha\beta}(\boldsymbol{r})=\frac{1}{4\pi\eta_2}\left[\left(\ln\frac{2}{\kappa r}-\gamma-\frac{1}{2}+\frac{a^2}{2r^2}\right)\delta_{\alpha\beta}+\left(1-\frac{a^2}{r^2}\right)\frac{r_\alpha\,r_\beta}{r^2}\right]. \tag{A.19}$$

The total stress tensor is obtained with the equations

$$\partial_\beta\sigma^i_{\alpha\beta}(\boldsymbol{r})=-\partial_\alpha p^i(\boldsymbol{r})+\partial_\beta\tau^i_{\alpha\beta}, \tag{A.20}$$

$$\tau^i_{\alpha\beta}=\eta_2(\partial_\alpha u^i_\beta+\partial_\beta u^i_\alpha), \tag{A.21}$$

$$\sigma^i_{\alpha\beta}=-p^i\delta_{\alpha\beta}+\tau^i_{\alpha\beta}. \tag{A.22}$$

The first two equations give the viscous stress and pressure field:

$$\tau^i_{\alpha\beta}(\boldsymbol{r}) = \eta_2 \left(\partial_\beta U_{\alpha\gamma} + \partial_\alpha U_{\beta\gamma}\right) F^i_\gamma, \tag{A.23}$$

$$p^i(\boldsymbol{r}) = \frac{r_\alpha}{2\pi r^2} F^i_\alpha. \tag{A.24}$$

Obtaining $\tau^i_{\alpha\beta}$ is straightforward. To get p^i, we first write its equation using Eqs. (A.6) and (A.21):

$$\partial_\alpha p^i(\boldsymbol{r}) = \eta_2 \left[\partial_\alpha \partial_\beta u^i_\beta + \partial^2_\beta u^i_\alpha\right], \tag{A.25}$$

where the first term in the rhs vanishes as the fluid is incompressible. We then solve this differential equation using polar coordinates and Eq.(A.18) to get the result above. Using (A.18) and (A.19) we get

$$u^i_\alpha(a\boldsymbol{n}^i) = \frac{1}{4\pi\eta_2}\left(\ln\frac{2}{\kappa a} - \gamma\right) F^i_\alpha, \tag{A.26}$$

which does not depend on θ. Therefore, using (A.12) and (A.13) on the first and third integrals in the rhs of Eq. (A.17) respectively, gives

$$\frac{a}{\eta_2}\sum_i \int_0^{2\pi} u^i_\alpha(a\boldsymbol{n}^i)\sigma^i_{\alpha\beta}(a\boldsymbol{n}^i)n^i_\beta = F^i_\alpha \left[\frac{1}{4\pi\eta_2}\left(\ln\frac{2}{\kappa a} - \gamma\right)\delta_{\alpha\beta}\right] F^i_\beta, \tag{A.27}$$

$$\frac{a}{\eta_2}\sum_{i\neq j} \int_0^{2\pi} u^i_\alpha(a\boldsymbol{n}^i)\sigma^j_{\alpha\beta}(a\boldsymbol{n}^i - \boldsymbol{r}^{ij})n^i_\beta = 0. \tag{A.28}$$

In order to compute the remaining integral in (A.17), we first expand the field $\boldsymbol{U}^i(\boldsymbol{r}^{ij} + a\boldsymbol{n}^j)$ to second order of a/r^{ij}:

$$\begin{aligned} U^i_{\alpha\beta}(\boldsymbol{r}^{ij} + a\boldsymbol{n}^j) = \frac{1}{4\pi\eta_2}\Bigg[&\left(\ln\frac{2}{\kappa r^{ij}} - \gamma - \frac{1}{2} - \frac{a}{r^{ij}}\cos(\theta-\phi) + \left(\frac{a}{r^{ij}}\right)^2\cos^2(\theta-\phi)\right)\delta_{\alpha\beta} \\ &\left(1 - \frac{2a}{r^{ij}}\cos(\theta-\phi) - \left(\frac{a}{r^{ij}}\right)^2\left(1 - 4\cos^2(\theta-\phi)\right)\right)\frac{r^{ij}_\alpha r^{ij}_\beta}{r^{ij^2}} \\ &\left(\frac{a}{r^{ij}} - 2\left(\frac{a}{r^{ij}}\right)^2\cos(\theta-\phi)\right)\frac{r^{ij}_\alpha n^j_\beta + r^{ij}_\beta n^j_\alpha}{r^{ij}} + \left(\frac{a}{r^{ij}}\right)^2 n^j_\alpha n^j_\beta + o\left(\frac{a}{r^{ij}}\right)^2\Bigg], \end{aligned} \tag{A.29}$$

where ϕ is the angle between the stress $\boldsymbol{\sigma}$ and the x-axis. Then using the expression of $\sigma^j_{\alpha\beta}$ as a function of $U^j_{\alpha\beta}$ (eqs. (A.22) – (A.24)) and expressing the unit vector $\boldsymbol{n}$ as a function of θ one finally gets

$$\bar{B}^{i\neq j}_{\alpha\beta} = \frac{1}{4\pi\eta_2}\left[\left(\ln\frac{2}{\kappa r^{ij}} - \gamma - \frac{1}{2} + \left(\frac{a}{r^{ij}}\right)^2\right)\delta_{\alpha\beta} + \left(1 - 2\left(\frac{a}{r^{ij}}\right)^2\right)\frac{r^{ij}_\alpha r^{ij}_\beta}{r^{ij^2}}\right] \tag{A.30}$$

A.2 Definite-positiveness of the mobility tensor for overlapping proteins

In their article, Diamant and Sokolov derived not only a definite-positive mobility tensor for interparticle distances such that $r > 2a_p$ but also one for $r \leq 2a_p$ (called inner tensor in the following).

To do so, they postulated the form it should take and determined its coefficients by satisfying the three following conditions:

- at $r = 0$, as the proteins overlap perfectly, the inner tensor should match the Saffman-Delbrück mobility tensor: $\mu_{SD}\boldsymbol{\delta}_{\alpha\beta}$.
- At $r = 2a_p$, the inner tensor should match the outer one.
- The inner tensor should be divergenceless.

They guessed a mobility tensor of the form

$$O_{\alpha\beta}^{\alpha\neq\beta}(r \leq 2a_p) = \frac{1}{4\pi\eta_2}\left[\left(C_1 + C_2\frac{r}{2a_p} + C_3\frac{r}{2a_p}\ln\frac{r}{2a_p}\right)\delta_{\alpha\beta} + \left(D_1 + D_2\frac{r}{2a_p} + D_3\frac{r}{2a_p}\ln\frac{r}{2a_p}\right)\frac{r_\alpha r_\beta}{r^2}\right]. \tag{A.31}$$

The first condition gives $C_1 = \mu_{\mathrm{SD}}$ and $D_1 = 0$, the second one, $C_2 = -(\ln 2 + 1/4)$ and $D_2 = 1/2$ and the last condition yields $C_3 = 2\ln 2 - 3/2$ and $D_3 = -\ln 2 + 3/4$.

This inner tensor should be definite-positive for every possible overlapping distance. However, we find a threshold under which this inner tensor is not definite-positive.

Therefore, we aim to derive this inner tensor by performing the calculations as it is performed by E. Wajnry [85] et al for the Rotne-Prager mobility tensor in the 3D case. Using the Faxen law, we can determine the mobility tensor from the velocities of the particles $\boldsymbol{u}_i$ which is given by

$$\boldsymbol{u}_i(\boldsymbol{r}_{ij}) = \frac{1}{2\pi a_p}\int_{\partial S_i}\boldsymbol{v}(\boldsymbol{r}')\,\mathrm{d}^2r', \tag{A.32}$$

where $\boldsymbol{r}_{ij} = \boldsymbol{r}_j - \boldsymbol{r}_i$ is the vector connecting the two centers and the $\boldsymbol{v}(\boldsymbol{r})$ is the velocity flow at point $\boldsymbol{r}$ in the fluid created by a cylinder pulled by a force $\boldsymbol{F}_i$. It is given by

$$v_\alpha(\boldsymbol{r}) = \begin{cases} \frac{1}{4\pi\eta_2}\left[\left(\ln\frac{2\ell_{SD}}{r} - \gamma - \frac{1}{2} + \frac{a_p^2}{2r^2}\right)\delta_{\alpha\beta} + \left(1 - \frac{a_p^2}{r^2}\right)\frac{r_\alpha r_\beta}{r^2}\right]F_\beta^i, & r > 2a_p \\ \frac{1}{4\pi\eta_2}\left[\ln\frac{2\ell_{\mathrm{SD}}}{a_p} - \gamma\right]F_\alpha^i & r \leq 2a_p \end{cases} \tag{A.33}$$

The configuration of the two overlapping proteins we consider is presented in Figure A.1. Knowing that the mobility tensor relates the velocity of a protein to the forces

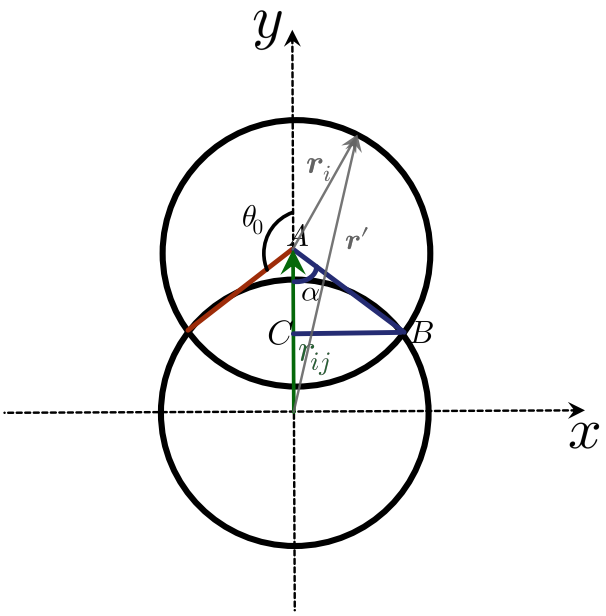

Figure A.1 – Sketch of two overlapping proteins. We choose the axes such that the overlapping is along $\boldsymbol{e_y}$. $\boldsymbol{r}_{ij}$ is the vector linking the two centers. $\boldsymbol{r}'$ is the sum of $\boldsymbol{r}_{ij}$ and $\boldsymbol{r}_i$. The triangle ABC is used to determine the relation between θ_0 and r_{ij}.

acting on all proteins, we identify

$$\boldsymbol{O} = \frac{1}{8\pi^2\eta_2}\left\{\int_{-\theta_0}^{\theta_0} \mathrm{d}\theta \left[\left(\ln\frac{2\ell_{\mathrm{SD}}}{r'} - \gamma - \frac{1}{2} + \frac{a_p^2}{2r'}\right)\mathbb{1} + \left(1 - \frac{a_p^2}{r'^2}\right)\frac{\boldsymbol{r}'\boldsymbol{r}'}{r'^2}\right] + \int_{-(\pi-\theta_0)}^{\pi-\theta_0}\left(\ln\frac{2\ell_{\mathrm{SD}}}{a_p} - \gamma\right)\mathbb{1}\right\}, \tag{A.34}$$

where $\boldsymbol{r}' = a_p \sin\theta\, \boldsymbol{e}_x + (r_{ij} + a_p\cos\theta)\boldsymbol{e}_y$ and θ_0 is the meridional angle at which the two proteins intersect such that $\cos\theta_0 = -r_{ij}/(2a_p)$. The first part comes from the outer flow for which $r' > 2a_p$ and the second part from the overlapping area.

Since the off-diagonal terms of the tensor $\boldsymbol{r}'\boldsymbol{r}'$ are odd functions their contribution vanish after integrating and we can rewrite the diagonal part as $a_p^2\sin^2\theta\,\mathbb{1}$ $+\left[(r_{ij} + a_p\cos\theta)^2 - a_p^2\sin^2\theta\right]\hat{\boldsymbol{r}}_{\boldsymbol{ij}}\hat{\boldsymbol{r}}_{\boldsymbol{ij}}$. Furthermore by using the expression of $r'^2 = a_p^2 + r_{ij}^2 + 2a_p r_{ij}\cos\theta$ we can express the logarithm coming from the outer flow as $\ln(2\ell_{\mathrm{SD}}/r') = \ln(2\ell_{\mathrm{SD}}/a_p) - \frac{1}{2}\ln\left[1 + (r_{ij}/a_p)^2 + 2(r_{ij}/a_p)\cos\theta\right]$. We therefore get

$$\begin{aligned}\boldsymbol{O} =& \frac{1}{4\pi\eta_2}\left(\ln\frac{2\ell_{\mathrm{SD}}}{a_p} - \gamma\right)\mathbb{1} \\ &+ \frac{\mathbb{1}}{4\pi^2\eta_2}\int_0^{\theta_0}\left[-\frac{1}{2}\ln\left(1 + \left(\frac{r_{ij}}{a_p}\right)^2 + 2\frac{r_{ij}}{a_p}\cos\theta\right) - \frac{1}{2}\left(1 - \frac{a_p^2}{r'^2}\right) + \left(\frac{a_p^2}{r'^2} - \frac{a_p^4}{r'^4}\right)\sin^2\theta\right]\mathrm{d}\theta \\ &+ \frac{\hat{\boldsymbol{r}}_{\boldsymbol{ij}}\hat{\boldsymbol{r}}_{\boldsymbol{ij}}}{4\pi^2\eta_2}\int_0^{\theta_0}\left(\frac{a_p^2}{r'^2} - \frac{a_p^4}{r'^4}\right)\left[\left(\frac{r_{ij}}{a_p} + \cos\theta\right)^2 - \sin^2\theta\right]\mathrm{d}\theta,\end{aligned} \tag{A.35}$$

where one recognizes that the first term is the well-known Saffman-Delbrück mobility. In the figure A.2 we can see that the form postulated by Sorkin and Diamant is not

equivalent to the true form of the inner tensor and even fails at very short distances.

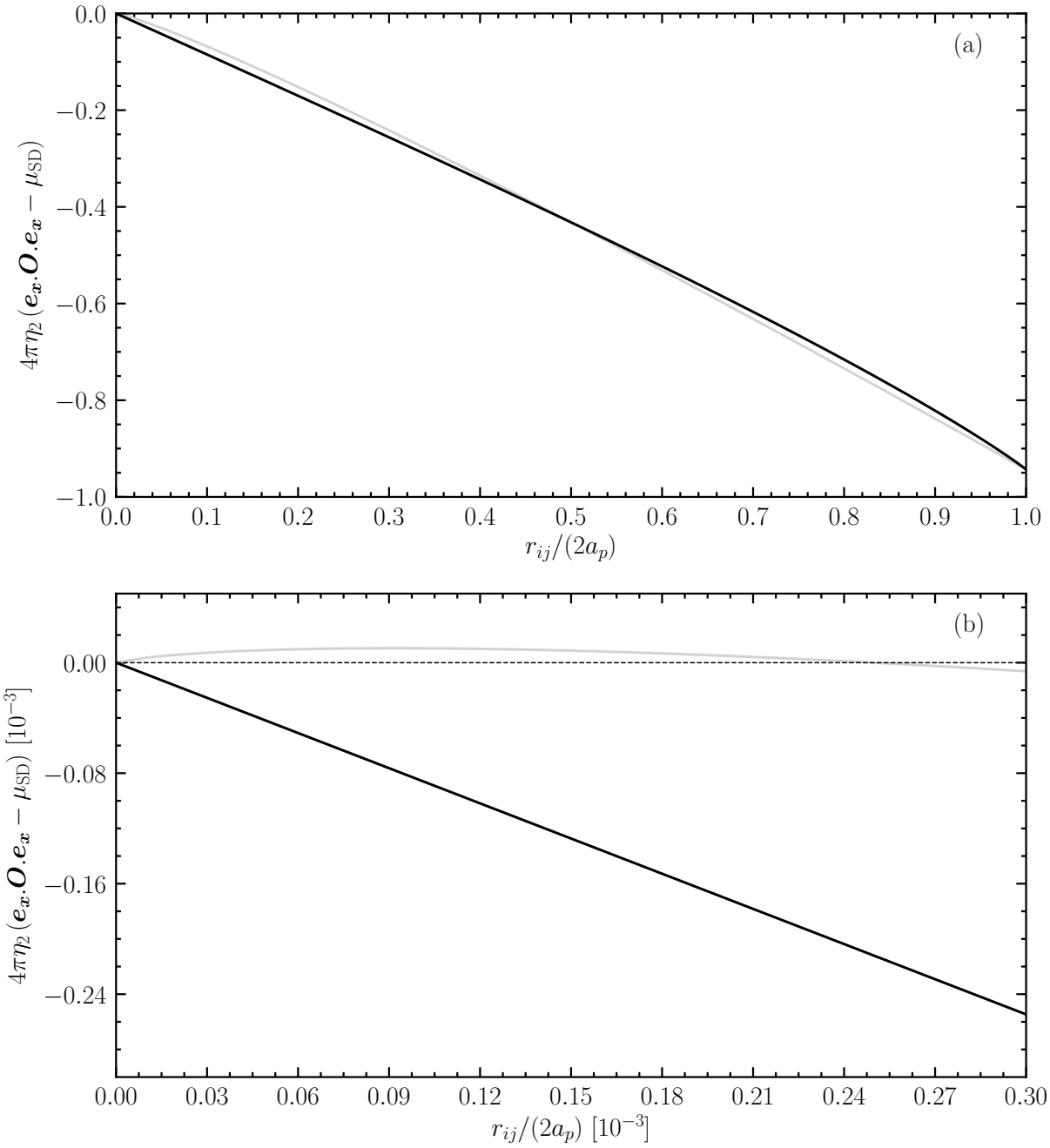

Figure A.2 – Mobility along $\boldsymbol{e}_x\boldsymbol{e}_x$ as function of $r_{ij}/(2a_p)$ subtracting the Saffman-Delbrück part for two overlapping proteins. (a) gives the comparison between the postulated form of Sorkin and Diamant (light gray) and the true value determined with (A.35) (black) for the full range of $r_{ij}/(2a_p)$. (b) is a zoom-in on a short distances range of $r_{ij}/(2a_p)$ where we can see that the postulated form fails to give a definite-positive mobility tensor when its sign changes. The parameters are $\eta_2 = 10^{-9}\,\mathrm{Jsm}^{-2}$, $a_p = 10\,\mathrm{nm}$.

Bibliography

[1] E. Fahy, D. Cotter, M. Sud, and S. Subramaniam, "Lipid classification, structures and tools", *Biochimica et Biophysica Acta (BBA) - Molecular and Cell Biology of Lipids*, 2011. DOI: https://doi.org/10.1016/j.bbalip.2011.06.009.

[2] Y. A. Hannun and R. M. Bell, "Functions of sphingolipids and sphingolipid breakdown products in cellular regulation", *Science*, vol. 243, no. 4890, pp. 500–507, 1989. DOI: 10.1126/science.2643164. eprint: https://www.science.org/doi/pdf/10.1126/science.2643164.

[3] G. van Meer, D. R. Voelker, and G. W. Feigenson, "Membrane lipids: Where they are and how they behave", en, *Nature Reviews Molecular Cell Biology*, vol. 9, no. 2, pp. 112–124, Feb. 2008. DOI: 10.1038/nrm2330.

[4] B. Alberts, D. Bray, K. Hopkin, A. D. Johnson, J. Lewis, M. Raff, K. Roberts, and P. Walter, *Essential cell biology*. Garland Science, 2015.

[5] J. N. Israelachvili, D. Mitchell, and B. W. Ninham, "Theory of self-assembly of lipid bilayers and vesicles", *Biochimica et Biophysica Acta (BBA) - Biomembranes*, vol. 470, no. 2, pp. 185–201, 1977. DOI: https://doi.org/10.1016/0005-2736(77)90099-2.

[6] K. Mitra, I. Ubarretxena-Belandia, T. Taguchi, G. Warren, and D. M. Engelman, "Modulation of the bilayer thickness of exocytic pathway membranes by membrane proteins rather than cholesterol", *Proceedings of the National Academy of Sciences*, vol. 101, no. 12, pp. 4083–4088, 2004. DOI: 10.1073/pnas.0307332101. eprint: https://www.pnas.org/doi/pdf/10.1073/pnas.0307332101.

[7] R. Hine *et al.*, *The facts on file dictionary of biology*. Infobase Publishing, 2009.

[8] H. Watson, "Biological membranes", *Essays In Biochemistry*, vol. 59, pp. 43–69, Nov. 2015. DOI: 10.1042/bse0590043.

[9] W. Curatolo, "Glycolipid function", *Biochimica et Biophysica Acta (BBA) - Reviews on Biomembranes*, vol. 906, no. 2, pp. 137–160, 1987. DOI: https://doi.org/10.1016/0304-4157(87)90009-8.

[10] T. Róg and I. Vattulainen, "Cholesterol, sphingolipids, and glycolipids: What do we know about their role in raft-like membranes?", *Chemistry and Physics of Lipids*, vol. 184, pp. 82–104, 2014. DOI: https://doi.org/10.1016/j.chemphyslip.2014.10.004.

[11] S. J. Singer and G. L. Nicolson, "The fluid mosaic model of the structure of cell membranes", *Science*, vol. 175, no. 4023, pp. 720–731, 1972. DOI: 10.1126/science.175.4023.720. eprint: https://www.science.org/doi/pdf/10.1126/science.175.4023.720.

[12] R. B. Gennis, *Biomembranes: molecular structure and function*. Springer Science & Business Media, 2013.

[13] B. A. Camley, C. Esposito, T. Baumgart, and F. L. Brown, "Lipid bilayer domain fluctuations as a probe of membrane viscosity", *Biophysical journal*, vol. 99, no. 6, pp. L44–L46, 2010.

[14] W. Rawicz, K. C. Olbrich, T. McIntosh, D. Needham, and E. Evans, "Effect of chain length and unsaturation on elasticity of lipid bilayers", *Biophysical journal*, vol. 79, no. 1, pp. 328–339, 2000.

[15] F. Jähnig, "What is the surface tension of a lipid bilayer membrane?", *Biophysical journal*, vol. 71, no. 3, p. 1348, 1996.

[16] E. Evans and W. Rawicz, "Entropy-driven tension and bending elasticity in condensed-fluid membranes", *Physical review letters*, vol. 64, no. 17, p. 2094, 1990.

[17] G. Blobel, "Intracellular protein topogenesis", *Proceedings of the National Academy of Sciences*, vol. 77, no. 3, pp. 1496–1500, 1980.

[18] P. V. Escribá, A. Ozaita, C. Ribas, A. Miralles, E. Fodor, T. Farkas, and J. A. Garcıa-Sevilla, "Role of lipid polymorphism in g protein-membrane interactions: Nonlamellar-prone phospholipids and peripheral protein binding to membranes", *Proceedings of the National Academy of Sciences*, vol. 94, no. 21, pp. 11 375–11 380, 1997.

[19] T. Weikl, M. Kozlov, and W. Helfrich, "Interaction of conical membrane inclusions: Effect of lateral tension", *Physical Review E*, vol. 57, no. 6, p. 6988, 1998.

[20] H. T. McMahon and J. L. Gallop, "Membrane curvature and mechanisms of dynamic cell membrane remodelling", *Nature*, vol. 438, no. 7068, pp. 590–596, 2005.

[21] T. Stanishneva-Konovalova, N. Derkacheva, S. Polevova, and O. Sokolova, "The role of bar domain proteins in the regulation of membrane dynamics", *Acta Naturæ*, vol. 8, no. 4 (31), 2016.

[22] M. M. Kessels and B. Qualmann, "Different functional modes of bar domain proteins in formation and plasticity of mammalian postsynapses", *Journal of cell science*, vol. 128, no. 17, pp. 3177–3185, 2015.

[23] J. McIlhinney, N. Hooper, J. L. Gallop, and H. T. McMahon, "Bar domains and membrane curvature: Bringing your curves to the bar.", *Biochemical Society Symposia*, Portland Press, vol. 72, 2005, pp. 223–231.

[24] B. Qualmann, D. Koch, and M. M. Kessels, "Let's go bananas: Revisiting the endocytic bar code", *The EMBO journal*, vol. 30, no. 17, pp. 3501–3515, 2011.

[25] O. Kahraman, R. Langen, and C. A. Haselwandter, "Directed supramolecular organization of n-bar proteins through regulation of h0 membrane immersion depth", *Scientific reports*, vol. 8, no. 1, pp. 1–13, 2018.

[26] C. Mim and V. M. Unger, "Membrane curvature and its generation by bar proteins", *Trends in biochemical sciences*, vol. 37, no. 12, pp. 526–533, 2012.

[27] B. J. Peter, H. M. Kent, I. G. Mills, Y. Vallis, P. J. G. Butler, P. R. Evans, and H. T. McMahon, "Bar domains as sensors of membrane curvature: The amphiphysin bar structure", *Science*, vol. 303, no. 5657, pp. 495–499, 2004.

[28] J. L. Gallop, C. C. Jao, H. M. Kent, P. J. G. Butler, P. R. Evans, R. Langen, and H. T. McMahon, "Mechanism of endophilin n-bar domain-mediated membrane curvature", *The EMBO journal*, vol. 25, no. 12, pp. 2898–2910, 2006.

[29] T. D. Pollard, W. C. Earnshaw, J. Lippincott-Schwartz, and G. Johnson, *Cell biology E-book*. Elsevier Health Sciences, 2016.

[30] J. C. Dawson, J. A. Legg, and L. M. Machesky, "Bar domain proteins: A role in tubulation, scission and actin assembly in clathrin-mediated endocytosis", *Trends in cell biology*, vol. 16, no. 10, pp. 493–498, 2006.

[31] M. Simunovic, G. A. Voth, A. Callan-Jones, and P. Bassereau, "When physics takes over: Bar proteins and membrane curvature", *Trends in cell biology*, vol. 25, no. 12, pp. 780–792, 2015.

[32] S. Liu, X. Xiong, X. Zhao, X. Yang, and H. Wang, "F-bar family proteins, emerging regulators for cell membrane dynamic changes-from structure to human diseases", *Journal of hematology & oncology*, vol. 8, no. 1, pp. 1–14, 2015.

[33] W. M. Henne *et al.*, "Structure and analysis of fcho2 f-bar domain: A dimerizing and membrane recruitment module that effects membrane curvature", *Structure*, vol. 15, no. 7, pp. 839–852, 2007.

[34] R. J. Heath and R. H. Insall, "F-bar domains: Multifunctional regulators of membrane curvature", *Journal of cell science*, vol. 121, no. 12, pp. 1951–1954, 2008.

[35] A. Frost, P. De Camilli, and V. M. Unger, "F-bar proteins join the bar family fold", *Structure*, vol. 15, no. 7, pp. 751–753, 2007.

[36] H. Zhao, A. Pykäläinen, and P. Lappalainen, "I-bar domain proteins: Linking actin and plasma membrane dynamics", *Current opinion in cell biology*, vol. 23, no. 1, pp. 14–21, 2011.

[37] R. Guidelli, "The common features of tetrameric ion channels and the role of electrostatic interactions", *Electrochemistry Communications*, vol. 121, p. 106 866, 2020.

[38] Z. Sands, A. Grottesi, and M. S. Sansom, "Voltage-gated ion channels", *Current Biology*, vol. 15, no. 2, R44–R47, 2005.

[39] G. Edwards and A. H. Weston, "The role of potassium channels in excitable cells", *Diabetes research and clinical practice*, vol. 28, S57–S66, 1995.

[40] X. Tao and R. MacKinnon, "Cryo-em structure of the kvap channel reveals a non-domain-swapped voltage sensor topology", *Elife*, vol. 8, e52164, 2019.

[41] J. L. Noebels, M. Avoli, M. A. Rogawski, R. W. Olsen, and A. V. Delgado-Escueta, "Jasper's basic mechanisms of the epilepsies [internet]", 2012.

[42] S. Aimon, A. Callan-Jones, A. Berthaud, M. Pinot, G. E. Toombes, and P. Bassereau, "Membrane shape modulates transmembrane protein distribution", *Developmental cell*, vol. 28, no. 2, pp. 212–218, 2014.

[43] F. Quemeneur, J. K. Sigurdsson, M. Renner, P. J. Atzberger, P. Bassereau, and D. Lacoste, "Shape matters in protein mobility within membranes", *Proceedings of the National Academy of Sciences*, vol. 111, no. 14, pp. 5083–5087, 2014.

[44] C. Kluge, M. Pöhnl, and R. A. Böckmann, "Spontaneous local membrane curvature induced by transmembrane proteins", *Biophysical Journal*, vol. 121, no. 5, pp. 671–683, 2022.

[45] O. Lewinson and N. Livnat-Levanon, "Mechanism of action of abc importers: Conservation, divergence, and physiological adaptations", *Journal of molecular biology*, vol. 429, no. 5, pp. 606–619, 2017.

[46] E. Steinfels, C. Orelle, J.-R. Fantino, O. Dalmas, J.-L. Rigaud, F. Denizot, A. Di Pietro, and J.-M. Jault, "Characterization of yvcc (bmra), a multidrug abc transporter constitutively expressed in bacillus subtilis", *Biochemistry*, vol. 43, no. 23, pp. 7491–7502, 2004.

[47] M. J. Li, M. Guttman, and W. M. Atkins, "Conformational dynamics of p-glycoprotein in lipid nanodiscs and detergent micelles reveal complex motions on a wide time scale", *Journal of Biological Chemistry*, vol. 293, no. 17, pp. 6297–6307, 2018.

[48] P. Borst and R. O. Elferink, "Mammalian abc transporters in health and disease", *Annual review of biochemistry*, vol. 71, no. 1, pp. 537–592, 2002.

[49] C. Orelle, F. Gubellini, A. Durand, S. Marco, D. Lévy, P. Gros, A. Di Pietro, and J.-M. Jault, "Conformational change induced by atp binding in the multidrug atp-binding cassette transporter bmra", *Biochemistry*, vol. 47, no. 8, pp. 2404–2412, 2008.

[50] P. F. Fribourg, M. Chami, C. O. S. Sorzano, F. Gubellini, R. Marabini, S. Marco, J.-M. Jault, and D. Lévy, "3d cryo-electron reconstruction of bmra, a bacterial multidrug abc transporter in an inward-facing conformation and in a lipidic environment", *Journal of molecular biology*, vol. 426, no. 10, pp. 2059–2069, 2014.

[51] H. B. Casimir, "On the attraction between two perfectly conducting plates", vol. 51, p. 793, 1948.

[52] M. Kardar and R. Golestanian, "The "friction" of vacuum, and other fluctuation-induced forces", *Reviews of Modern Physics*, vol. 71, no. 4, p. 1233, 1999.

[53] A. Gambassi, "The casimir effect: From quantum to critical fluctuations", vol. 161, no. 1, p. 012 037, 2009.

[54] A.-F. Bitbol, P. G. Dommersnes, and J.-B. Fournier, "Fluctuations of the casimir-like force between two membrane inclusions", *Physical Review E*, vol. 81, no. 5, p. 050 903, 2010.

[55] M. Goulian, R. Bruinsma, and P. Pincus, "Long-range forces in heterogeneous fluid membranes", *EPL (Europhysics Letters)*, vol. 22, no. 2, p. 145, 1993.

[56] A.-F. Bitbol, "Statistics and dynamics of complex membranes", Ph.D. dissertation, Université Paris-Diderot-Paris VII, 2012.

[57] W. Helfrich, "Elastic properties of lipid bilayers: Theory and possible experiments", *Zeitschrift für Naturforschung c*, vol. 28, no. 11-12, pp. 693–703, 1973.

[58] S. A. Safran, *Statistical thermodynamics of surfaces, interfaces, and membranes*. CRC Press, 2018.

[59] P. B. Canham, "The minimum energy of bending as a possible explanation of the biconcave shape of the human red blood cell", *Journal of theoretical biology*, vol. 26, no. 1, pp. 61–81, 1970.

[60] R. G. Morris and M. S. Turner, "Mobility measurements probe conformational changes in membrane proteins due to tension", *Phys. Rev. Lett.*, vol. 115, p. 198 101, 19 Nov. 2015. DOI: 10.1103/PhysRevLett.115.198101.

[61] C. Barbetta, "Forces and fluctuations in planar, spherical and tubular membranes", *arXiv preprint arXiv:1011.1640*, 2010.

[62] M. Deserno, "Fluid lipid membranes–a primer", *http://www.cmu.edu/biolphys/deserno/*, 2007.

[63] R. Phillips, T. Ursell, P. Wiggins, and P. Sens, "Emerging roles for lipids in shaping membrane-protein function", *Nature*, vol. 459, no. 7245, pp. 379–385, 2009.

[64] R. R. Netz, "Inclusions in fluctuating membranes: Exact results", *Journal de Physique I*, vol. 7, no. 7, pp. 833–852, 1997.

[65] E. Reister and U. Seifert, "Lateral diffusion of a protein on a fluctuating membrane", *EPL (Europhysics Letters)*, vol. 71, no. 5, p. 859, 2005.

[66] E. Reister-Gottfried, S. M. Leitenberger, and U. Seifert, "Diffusing proteins on a fluctuating membrane: Analytical theory and simulations", *Physical Review E*, vol. 81, no. 3, p. 031 903, 2010.

[67] S. M. Leitenberger, E. Reister-Gottfried, and U. Seifert, "Curvature coupling dependence of membrane protein diffusion coefficients", *Langmuir*, vol. 24, no. 4, pp. 1254–1261, 2008.

[68] A. Naji, P. J. Atzberger, and F. L. Brown, "Hybrid elastic and discrete-particle approach to biomembrane dynamics with application to the mobility of curved integral membrane proteins", *Physical review letters*, vol. 102, no. 13, p. 138 102, 2009.

[69] V. Démery and D. Lacoste, "Mechanical factors affecting the mobility of membrane proteins", *arXiv preprint arXiv:1810.09910*, 2018.

[70] P. Saffman and M. Delbrück, "Brownian motion in biological membranes", *Proceedings of the National Academy of Sciences*, vol. 72, no. 8, pp. 3111–3113, 1975.

[71] U. Seifert, "Fluid membranes in hydrodynamic flow fields: Formalism and an application to fluctuating quasispherical vesicles in shear flow", *The European Physical Journal B-Condensed Matter and Complex Systems*, vol. 8, no. 3, pp. 405–415, 1999.

[72] M. L. Henle and A. J. Levine, "Hydrodynamics in curved membranes: The effect of geometry on particulate mobility", *Physical Review E*, vol. 81, no. 1, p. 011 905, 2010.

[73] D. K. Lubensky and R. E. Goldstein, "Hydrodynamics of monolayer domains at the air–water interface", *Physics of fluids*, vol. 8, no. 4, pp. 843–854, 1996.

[74] N. Oppenheimer and H. Diamant, "Correlated dynamics of inclusions in a supported membrane", *Physical Review E*, vol. 82, no. 4, p. 041 912, 2010.

[75] D. J. Callaway, B. Farago, and Z. Bu, "Nanoscale protein dynamics: A new frontier for neutron spin echo spectroscopy", *The European Physical Journal E*, vol. 36, no. 7, pp. 1–8, 2013.

[76] H. Lamb, *Hydrodynamics*. New York: Cambridge University Press, 1997.

[77] P. Saffman, "Brownian motion in thin sheets of viscous fluid", *Journal of Fluid Mechanics*, vol. 73, no. 4, pp. 593–602, 1976.

[78] A. J. Levine and F. MacKintosh, "Dynamics of viscoelastic membranes", *Physical Review E*, vol. 66, no. 6, p. 061 606, 2002.

[79] N. Oppenheimer and H. Diamant, "Correlated diffusion of membrane proteins and their effect on membrane viscosity", *Biophysical Journal*, vol. 96, no. 8, pp. 3041–3049, 2009.

[80] Y. Sokolov and H. Diamant, "Many-particle mobility and diffusion tensors for objects in viscous sheets", *The Journal of Chemical Physics*, vol. 149, no. 3, p. 034 901, 2018.

[81] R. Zwanzig, J. Kiefer, and G. H. Weiss, "On the validity of the kirkwood-riseman theory", *proceedings of the National Academy of Sciences of the United States of America*, vol. 60, no. 2, p. 381, 1968.

[82] D. L. Ermak and J. A. McCammon, "Brownian dynamics with hydrodynamic interactions", en, *The Journal of Chemical Physics*, vol. 69, no. 4, pp. 1352–1360, 1978. DOI: 10.1063/1.436761.

[83] J. K. Sigurdsson, F. L. Brown, and P. J. Atzberger, "Hybrid continuum-particle method for fluctuating lipid bilayer membranes with diffusing protein inclusions", en, *Journal of Computational Physics*, vol. 252, pp. 65–85, Nov. 2013. DOI: 10.1016/j.jcp.2013.06.016.

[84] J. Rotne and S. Prager, "Variational Treatment of Hydrodynamic Interaction in Polymers", en, *The Journal of Chemical Physics*, vol. 50, no. 11, pp. 4831–4837, Jun. 1969. DOI: 10.1063/1.1670977.

[85] E. Wajnryb, K. A. Mizerski, P. J. Zuk, and P. Szymczak, "Generalization of the Rotne Prager Yamakawa mobility and shear disturbance tensors", en, *Journal of Fluid Mechanics*, vol. 731, R3, Sep. 2013. DOI: 10.1017/jfm.2013.402.

[86] Q. Goutaland, F. van Wijland, J.-B. Fournier, and H. Noguchi, "Binding of thermalized and active membrane curvature-inducing proteins", *Soft Matter*, vol. 17, no. 22, pp. 5560–5573, 2021.

[87] A. Frost, R. Perera, A. Roux, K. Spasov, O. Destaing, E. H. Egelman, P. De Camilli, and V. M. Unger, "Structural basis of membrane invagination by f-bar domains", *Cell*, vol. 132, no. 5, pp. 807–817, 2008.

[88] G. J. Doherty and H. T. McMahon, "Mechanisms of endocytosis", *Annual review of biochemistry*, vol. 78, pp. 857–902, 2009.

[89] S. L. Schmid and V. A. Frolov, "Dynamin: Functional design of a membrane fission catalyst", *Annu. Rev. Cell Dev. Biol.*, vol. 27, pp. 79–105, 2011.

[90] J. Prost and R. Bruinsma, "Shape fluctuations of active membranes", *Europhys. Lett.*, vol. 33, pp. 321–326, 1996.

[91] H. Turlier *et al.*, "Equilibrium physics breakdown reveals the active nature of red blood cell flickering", *Nature Phys.*, vol. 12, pp. 513–519, 2016.

[92] Y. Yang and M. Wu, "Rhythmicity and waves in the cortex of single cells", *Phil. Trans. R. Soc. B*, vol. 373, p. 20 170 116, 2018.

[93] H.-G. Döbereiner *et al.*, "Lateral membrane waves constitute a universal dynamic pattern of motile cells", *Phys. Rev. Lett.*, vol. 97, p. 038 102, 2006.

[94] D. Taniguchi, S. Ishihara, T. Oonuki, M. Honda-Kitahara, K. Kaneko, and S. Sawai, "Phase geometries of two-dimensional excitable waves govern self-organized morphodynamics of amoeboid cells", *Proc. Natl. Acad. Sci. USA*, vol. 110, pp. 5016–5021, 2013.

[95] O. Hoeller *et al.*, "Gβ regulates coupling between actin oscillators for cell polarity and directional migration", *PLoS Biol.*, vol. 14, e1002381, 2016.

[96] S. Kohyama, N. Yoshinaga, M. Yanagisawa, K. Fujiwara, and N. Doi, "Cell-sized confinement controls generation and stability of a protein wave for spatiotemporal regulation in cells", *eLife*, vol. 8, e44591, 2019.

[97] R. C. Chatelier and A. P. Minton, *Biophys. J.*, vol. 71, pp. 2367–2374, 5 1996.

[98] A. P. Minton, *Biophys. J.*, vol. 80, pp. 1641–1648, 4 1996.

[99] V. P. Zhdanov and B. Kasemo, *Eur. Biophys. J.*, vol. 39, pp. 1477–1482, 2010.

[100] P. Singh, P. Mahata, T. Baumgart, and S. L. Das, "Curvature sorting of proteins on a cylindrical lipid membrane tether connected to a reservoir", *Phys. Rev. E*, vol. 85, p. 051 906, 5 May 2012. DOI: 10.1103/PhysRevE.85.051906.

[101] V. Wasnik, N. S. Wingreen, and R. Mukhopadhyay, *PLoS One*, vol. 10, pp. 1–13, 2015.

[102] T. V. Sachin Krishnan, S. L. Das, and P. B. Sunil Kumar, "Transition from curvature sensing to generation in a vesicle driven by protein binding strength and membrane tension", *Soft Matter*, vol. 15, pp. 2071–2080, 9 2019. DOI: 10.1039/C8SM02623H.

[103] P. Dommersnes and J.-B. Fournier, "N-body study of anisotropic membrane inclusions: Membrane mediated interactions and ordered aggregation", *Eur. Phys. J. B*, vol. 12, no. 1, pp. 9–12, Nov. 1999. DOI: 10.1007/s100510050968.

[104] P. G. Dommersnes and J.-B. Fournier, "The many-body problem for anisotropic membrane inclusions and the self-assembly of "saddle" defects into an "egg carton"", *Biophys. J.*, vol. 83, pp. 2898–2905, 2002.

[105] H. Noguchi and J.-B. Fournier, "Membrane structure formation induced by two types of banana-shaped proteins", *Soft Matter*, vol. 13, pp. 4099–4111, 2017.

[106] T. Baumgart, B. R. Capraro, C. Zhu, and S. L. Das, "Thermodynamics and mechanics of membrane curvature generation and sensing by proteins and lipids", *Annu. Rev. Phys. Chem.*, vol. 62, pp. 483–506, 2011.

[107] D. S. Dean, "Langevin equation for the density of a system of interacting langevin processes", *Journal of Physics A: Mathematical and General*, vol. 29, no. 24, p. L613, 1996.

[108] K. Kawasaki, "Stochastic model of slow dynamics in supercooled liquids and dense colloidal suspensions", *Physica A: Statistical Mechanics and its Applications*, vol. 208, no. 1, pp. 35–64, 1994. DOI: https://doi.org/10.1016/0378-4371(94)90533-9.

[109] N. Weil and O. Farago, *Eur. Phys. J. E*, vol. 33, p. 81, 2010.

[110] J.-B. Fournier and P. Galatola, *Eur. Phys. J. E*, vol. 38, p. 86, 2015.

[111] P. D. Blood and G. A. Voth, "Direct observation of bin/amphiphysin/rvs (bar) domain-induced membrane curvature by means of molecular dynamics simulations", *Proc. Natl. Acad. Sci. USA*, vol. 103, pp. 15 068–15 072, 2006.

[112] H. Yu and K. Schulten, "Membrane sculpting by f-bar domains studied by molecular dynamics simulations", *PLoS Comput. Biol.*, vol. 9, e1002892, 2013.

[113] M. I. Mahmood, H. Noguchi, and K. Okazaki, "Curvature induction and sensing of the f-bar protein pacsin1 on lipid membranes via molecular dynamics simulations", *Sci. Rep.*, vol. 9, p. 14 557, 2019.

[114] J. Hu, T. Weikl, and R. Lipowsky, "Vesicles with multiple membrane domains", *Soft Matter*, vol. 7, pp. 6092–6102, 2011.

[115] K. K. Sreeja and P. B. Sunil Kumar, "Lipid-protein interaction induced domains: Kinetics and conformational changes in multicomponent vesicles", *J. Chem. Phys.*, vol. 148, p. 134 703, 2018.

[116] W. T. Góźdź, N. Bobrovska, and A. Ciach, "The interface width of separated two-component lipid membrane separation of components in lipid membranes induced by shape transformation", *J. Chem. Phys.*, vol. 137, p. 015 101, 2012.

[117] C. Tozzi, N. Walani, and M. Arroyo, "Out-of-equilibrium mechanochemistry and selforganization of fluid membranes interacting with curved proteins", *New J. Phys.*, vol. 21, p. 093 004, 2019.

[118] N. Ramakrishnan, R. P. Bradley, R. W. Tourdot, and R. Radhakrishnan, "Biophysics of membrane curvature remodeling at molecular and mesoscopic length-scales", *J. Phys.: Condens. Matter*, vol. 30, p. 273 001, 2018.

[119] H. Noguchi, "Shape deformation of lipid membranes by banana-shaped protein rods: Comparison with isotropic inclusions and membrane rupture", *Phys. Rev. E*, vol. 93, p. 052 404, 2016.

[120] H. Noguchi, "Shape transition from elliptical to cylindrical membrane tubes induced by chiral crescent-shaped protein rods", *Sci. Rep.*, vol. 9, p. 11 721, 2019.

[121] H. Noguchi and G. Gompper, "Meshless membrane model based on the moving least-squares method", *Phys. Rev. E*, vol. 73, p. 021 903, 2006.

[122] H. Shiba and H. Noguchi, "Estimation of the bending rigidity and spontaneous curvature of fluid membranes in simulations", *Phys. Rev. E*, vol. 84, p. 031 926, 2011.

[123] H. Noguchi, "Two- or three-step assembly of banana-shaped proteins coupled with shape transformation of lipid membranes", *EPL*, vol. 108, p. 48 001, 2014.

[124] S. E. Feller, Y. Zhang, R. W. Pastor, and B. R. Brooks, "Constant pressure molecular dynamics simulation: The langevin piston method", *J. Chem. Phys.*, vol. 103, pp. 4613–4621, 1995.

[125] H. Noguchi, "Line tension of branching junctions of bilayer membranes", *Soft Matter*, vol. 8, pp. 3146–3153, 2012.

[126] M. P. Allen and D. J. Tildesley, *Computer Simulation of Liquids*. Oxford: Clarendon Press, 1987.

[127] H. Noguchi, "Solvent-free coarse-grained lipid model for large-scale simulations", *J. Chem. Phys.*, vol. 134, p. 055 101, 2011.

[128] H. Noguchi, "Cup-to-vesicle transition of a fluid membrane with spontaneous curvature", *J. Chem. Phys.*, vol. 151, p. 094 903, 2019.

[129] E. Evans and F. Ludwig, "Dynamic strengths of molecular anchoring and material cohesion in fluid biomembranes", *Journal of physics: condensed matter*, vol. 12, no. 8A, A315, 2000.

[130] E. Evans, V. Heinrich, F. Ludwig, and W. Rawicz, "Dynamic tension spectroscopy and strength of biomembranes", *Biophysical journal*, vol. 85, no. 4, pp. 2342–2350, 2003.

[131] H. V. Ly and M. L. Longo, "The influence of short-chain alcohols on interfacial tension, mechanical properties, area/molecule, and permeability of fluid lipid bilayers", *Biophysical Journal*, vol. 87, no. 2, pp. 1013–1033, 2004.

[132] T. Baumgart, S. T. Hess, and W. W. Webb, "Imaging coexisting fluid domains in biomembrane models coupling curvature and line tension", *Nature*, vol. 425, pp. 821–824, 2003.

[133] S. Veatch and S. L. Keller, "Separation of liquid phases in giant vesicles of ternary mixtures of phospholipids and cholesterol", *Biophys. J.*, vol. 85, pp. 3074–3083, 2003.

[134] M. Yanagisawa, M. Imai, and T. Taniguchi, "Shape deformation of ternary vesicles coupled with phase separation", *Phys. Rev. Lett.*, vol. 100, p. 148 102, 2008.

[135] D. A. Christian *et al.*, "Spotted vesicles, striped micelles and janus assemblies induced by ligand binding", *Nat. Mater.*, vol. 8, pp. 843–849, 2009.

[136] Q. Goutaland and J.-B. Fournier, "Saffman-delbrück and beyond: A pointlike approach", *The European Physical Journal E*, vol. 42, no. 12, pp. 1–8, 2019.

[137] B. Hughes, B. Pailthorpe, and L. White, "The translational and rotational drag on a cylinder moving in a membrane", *Journal of Fluid Mechanics*, vol. 110, pp. 349–372, 1981.

[138] H. A. Stone and A. Ajdari, "Hydrodynamics of particles embedded in a flat surfactant layer overlying a subphase of finite depth", *Journal of Fluid Mechanics*, vol. 369, pp. 151–173, 1998.

[139] H. A. Stone and H. Masoud, "Mobility of membrane-trapped particles", *Journal of Fluid Mechanics*, vol. 781, pp. 494–505, 2015.

[140] J.-M. Park and T. Lubensky, "Disclination asymmetry in deformable hexatic membranes and the kosterlitz-thouless transitions", *Journal de Physique I*, vol. 6, no. 4, pp. 493–502, 1996.

[141] R. Cortez, "The method of regularized stokeslets", *SIAM Journal on Scientific Computing*, vol. 23, no. 4, pp. 1204–1225, 2001.

[142] A. J. Levine and T. Lubensky, "Response function of a sphere in a viscoelastic two-fluid medium", *Physical Review E*, vol. 63, no. 4, p. 041 510, 2001.

[143] C. S. Peskin, "The immersed boundary method", *Acta numerica*, vol. 11, pp. 479–517, 2002.

[144] P. J. Atzberger, P. R. Kramer, and C. S. Peskin, "A stochastic immersed boundary method for fluid-structure dynamics at microscopic length scales", *Journal of Computational Physics*, vol. 224, no. 2, pp. 1255–1292, 2007.

[145] B. A. Camley and F. L. Brown, "Beyond the creeping viscous flow limit for lipid bilayer membranes: Theory of single-particle microrheology, domain flicker spectroscopy, and long-time tails", *Physical Review E*, vol. 84, no. 2, p. 021 904, 2011.

[146] B. A. Camley and F. L. Brown, "Diffusion of complex objects embedded in free and supported lipid bilayer membranes: Role of shape anisotropy and leaflet structure", *Soft Matter*, vol. 9, no. 19, pp. 4767–4779, 2013.

[147] K. Seki, S. Mogre, and S. Komura, "Diffusion coefficients in leaflets of bilayer membranes", *Physical Review E*, vol. 89, no. 2, p. 022 713, 2014.

[148] U. Seifert and S. A. Langer, "Viscous modes of fluid bilayer membranes", *EPL (Europhysics letters)*, vol. 23, no. 1, p. 71, 1993.

[149] R. Merkel, E. Sackmann, and e. Evans, "Molecular friction and epitactic coupling between monolayers in supported bilayers", *Journal de Physique*, vol. 50, no. 12, pp. 1535–1555, 1989.

[150] E. Evans and A. Yeung, "Hidden dynamics in rapid changes of bilayer shape", *Chemistry and physics of lipids*, vol. 73, no. 1-2, pp. 39–56, 1994.

[151] W. K. den Otter and S. Shkulipa, "Intermonolayer friction and surface shear viscosity of lipid bilayer membranes", *Biophysical journal*, vol. 93, no. 2, pp. 423–433, 2007.

[152] J.-B. Fournier, N. Khalifat, N. Puff, and M. Angelova, "Chemically triggered ejection of membrane tubules controlled by intermonolayer friction", *Physical review letters*, vol. 102, no. 1, p. 018 102, 2009.

[153] R. J. Hill and C.-Y. Wang, "Diffusion in phospholipid bilayer membranes: Dual-leaflet dynamics and the roles of tracer–leaflet and inter-leaflet coupling", *Proceedings of the Royal Society A: Mathematical, Physical and Engineering Sciences*, vol. 470, no. 2167, p. 20 130 843, 2014.

[154] H. Gruler, "Chemoelastic effect of membranes", *Zeitschrift für Naturforschung C*, vol. 30, no. 9-10, pp. 608–614, 1975.

[155] S. Leibler, "Curvature instability in membranes", *Journal de Physique*, vol. 47, no. 3, pp. 507–516, 1986.

[156] C. Prévost, H. Zhao, J. Manzi, E. Lemichez, P. Lappalainen, A. Callan-Jones, and P. Bassereau, "Irsp53 senses negative membrane curvature and phase separates along membrane tubules", *Nature communications*, vol. 6, no. 1, pp. 1–11, 2015.

[157] C. Van Der Wel, A. Vahid, A. Šarić, T. Idema, D. Heinrich, and D. J. Kraft, "Lipid membrane-mediated attraction between curvature inducing objects", *Scientific reports*, vol. 6, no. 1, pp. 1–10, 2016.

[158] F. Brochard and J. Lennon, "Frequency spectrum of the flicker phenomenon in erythrocytes", *Journal de Physique*, vol. 36, no. 11, pp. 1035–1047, 1975.

[159] V. Démery and D. S. Dean, "Drag forces in classical fields", *Physical review letters*, vol. 104, no. 8, p. 080 601, 2010.

[160] D. R. Daniels, "Curvature correction to the mobility of fluid membrane inclusions", en, *The European Physical Journal E*, vol. 39, no. 10, p. 96, Oct. 2016. DOI: 10.1140/epje/i2016-16096-3.

[161] B. Sorkin and H. Diamant, "Persistent collective motion of a dispersing membrane domain", *Biophysical journal*, vol. 120, no. 10, pp. 2030–2039, 2021.

[162] M. Chein, E. Perlson, and Y. Roichman, "Flow arrest in the plasma membrane", *Biophysical journal*, vol. 117, no. 5, pp. 810–816, 2019.

[163] G. Nägele, "Brownian dynamics simulations", *LECTURE MANUSCRIPTS OF THE SPRING SCHOOL OF THE INSTITUTE OF SOLID STATE RESEARCH*, vol. 37, B4, 2005.

[164] D. W. Scott, "Box–muller transformation", *Wiley Interdisciplinary Reviews: Computational Statistics*, vol. 3, no. 2, pp. 177–179, 2011.

[165] W. H. Press, S. A. Teukolsky, W. T. Vetterling, B. P. Flannery, *et al.*, *Numerical recipes in c*, 1992.

[166] C. Beenakker, "Ewald sum of the rotne–prager tensor", *The Journal of chemical physics*, vol. 85, no. 3, pp. 1581–1582, 1986.

[167] J. Bleibel, "Ewald sum for hydrodynamic interactions with periodicity in two dimensions", *Journal of Physics A: Mathematical and Theoretical*, vol. 45, no. 22, p. 225 002, 2012.

[168] A. Naji, A. J. Levine, and P. A. Pincus, "Corrections to the saffman-delbrück mobility for membrane bound proteins", *Biophysical journal*, vol. 93, no. 11, pp. L49–L51, 2007.

[169] R. Zakine, J.-B. Fournier, and F. van Wijland, "Field-embedded particles driven by active flips", *Phys. Rev. Lett.*, vol. 121, p. 028 001, 2018.

[170] J. G. Kirkwood and J. Riseman, "The intrinsic viscosities and diffusion constants of flexible macromolecules in solution", *The Journal of Chemical Physics*, vol. 16, no. 6, pp. 565–573, 1948.